Summer 8-16-2024

Scaling, Modeling, and Resilience of the Arctic Boreal Ecosystem

Wouter Hantson
University of Maine, wouter.hantson@gmail.com

SCALING, MODELING, AND RESILIENCE OF THE ARCTIC BOREAL ECOSYSTEM

By

Wouter Hantson

B.A. Erasmus Hogeschool Brussel 2005

M.A. Wageningen University, 2010

A DISSERTATION

Submitted in Partial Fulfillment of the

Requirements for the Degree of

Doctor of Philosophy

(in Forest Resources)

The Graduate School

The University of Maine

August 2024

Advisory Committee:

Daniel J. Hayes, Associate Professor of Geospatial Analysis &

Remote Sensing, Advisor

Aaron Weiskittel, Professor of Forest Biometrics and Modeling

Ivan Fernandez, Professor Emeritus of Soil Science

David Hiebeler, Professor of Mathematics

Joshua Fisher, Associate Professor of Environmental Science and Policy

SCALING MODELING, AND RESILIENCE OF THE ARCTIC-BOREAL ECOSYSTEM

By Wouter Hantson

Dissertation advisor: Dr. Daniel J. Hayes

An Abstract of the Dissertation Presented
in Partial Fulfillment of the Requirements for the
Degree of Doctor of Philosophy
(in Forest Resources)
August 2024

Arctic tundra landscapes are characterized by underlying permafrost sustained by extremely low average temperatures. These permafrost soils have been sequestering carbon for millennia, effectively locking it into the frozen ground. Currently, anthropogenic climate change, exacerbated by Arctic amplification, is driving rapid and unprecedented warming in the Arctic region putting the permafrost at risk of thaw. Thawing permafrost could release vast amounts of previously stored carbon as greenhouse gasses, driving the permafrost carbon feedback to accelerate warming. Unfortunately, the high spatial variability and complex feedback mechanisms limit our understanding of the connections and dynamics between above- and below-ground processes, and current models often fail to adequately capture permafrost C dynamics, a much-needed representation in climate predictions.

First, we conducted a scaling exercise to evaluate the potential of novel remote sensing technologies to capture key tundra processes and reduce observational mismatches. Unoccupied aerial systems, airborne imaging spectroscopy, and satellite imagery were used to model the active layer and characterize key permafrost features. Medium spatial resolution image bands proved to be good predictors of average thaw depth, whereas high resolution imagery showed more contrast

beneficial in complex landscapes like polygon tundra. And while average thaw depth predictions have proved valuable, when studying the resilience of the Arctic Boreal Region (ABR) it is important to observe local features at the matching scale. Second, airborne imaging spectroscopy allows for a region-wide mapping of spectral vegetation traits reflecting the variability in hydrology or nutrient availability. Key traits indicative of tundra functioning were selected and clustered to create a high-resolution spatial dataset reflecting above-ground tundra characteristics reflecting the below-ground permafrost conditions.

Further analysis of the spectral traits revealed the local adaptation strategies to environmental conditions and disturbances. Lastly, based on the Landsat archive, yearly disturbances were mapped and disturbance trends by thermokarst zone were created. This study highlights the importance of landscape characteristics in analyzing and modeling disturbance trends.

By leveraging each remote sensing data product, we enhanced the characterization of tundra landscapes. The scaling approach identified the benefits and pitfalls of each product for modeling, which is crucial for region-wide application. Remote sensing proved extremely valuable and provided insights into the historical and current state of the permafrost and allows for an improved prediction of future shifts in vegetation and ecosystem trajectories by improving the modeling of key vegetation parameters and understanding permafrost-vegetation interactions.

ACKNOWLEDGEMENTS

This work was supported by a grant from NASA's Arctic Boreal Vulnerability Experiment (NNX15AU53A) and funding from DOE's Next Generation Ecosystem Experiment (UT-Battelle / ORNL subcontract 4000172408). The Next-Generation Ecosystem Experiments (NGEE Arctic) project is supported by the Office of Biological and Environmental Research in the DOE Office of Science. Research sponsored by the Laboratory Directed Research and Development Program of Oak Ridge National Laboratory, managed by UT-Battelle, LLC, for the U. S. Department of Energy.

TABLE OF CONTENTS

LIST OF TABLES

LIST OF FIGURES

CHAPTER 1

SCALING ARCTIC LANDSCAPE AND PERMAFROST FEATURES IMPROVES ACTIVE LAYER DEPTH MODELING

Tundra ecosystems in the Arctic store up to 40% of global below-ground organic carbon but are exposed to the fastest climate warming on Earth. However, accurately monitoring landscape changes in the Arctic is challenging due to the complex interactions among permafrost, micro-topography, climate, vegetation, and disturbance. This complexity results in high spatiotemporal variability in permafrost distribution and active layer depth (ALD). Moreover, these key tundra processes interact at different scales, and an observational mismatch can limit our understanding of intrinsic connections and dynamics between above and below-ground processes. Consequently, this could limit our ability to model and anticipate how ALD will respond to climate change and disturbances across tundra ecosystems.

In this chapter, we studied the fine-scale heterogeneity of ALD and its connections with land surface characteristics across spatial and spectral scales using a combination of ground, unoccupied aerial system, airborne, and satellite observations. We showed that airborne sensors such as AVIRIS-NG and medium-resolution satellite Earth observation systems like Sentinel-2 can capture the average ALD at the landscape scale. We found that the best observational scale for ALD modeling is heavily influenced by the vegetation and landform patterns occurring on the landscape. Landscapes characterized by small-scale permafrost features such as polygon tussock tundra require high-resolution observations to capture the intrinsic connections between permafrost and small-scale land surface and disturbance patterns. Conversely, in landscapes dominated by water tracks and shrubs, permafrost features manifest at a larger scale and our model results indicate the best performance at medium resolution (5 m), outperforming both higher (0.4 m) and lower resolution (10 m) models. This transcends our study

to show that permafrost response to climate change may vary across dominant ecosystem types, driven by different above- and below-ground connections and the scales at which these connections are happening. We thus recommend tailoring observational scales based on landforms and characteristics for modeling permafrost distribution, thereby mitigating the influences of spatial-scale mismatches and improving the understanding of vegetation and permafrost changes for the Arctic region.

1.1. Introduction

Tundra landscapes are an extensive feature of the northern arctic biome where cold average annual temperatures result in perennially frozen ground or permafrost if frozen for at least two consecutive years (French 2007; Van Everdingen, Association, and Others 1998). Extremely low soil temperatures and poor drainage facilitate the long-term accumulation of dead organic matter, and as a result, permafrost soils have been sequestering carbon for thousands of years (McGuire et al. 2012; Treat et al. 2024). Estimates suggest a large stock of around 1,500 petagrams of soil organic carbon (SOC) across the circumpolar Arctic, a magnitude that is almost twice the size of the atmospheric C pool (Schuur et al. 2015; Hugelius et al. 2014). At the same time, the Arctic region has experienced warming two to four times faster than any other biome on Earth. The resulting ground thaw could unlock a substantial amount of the C previously stored in the permafrost and make it available for decomposition and release to the atmosphere as greenhouse gasses (Schuur et al. 2015; Hayes et al. 2014). This permafrost carbon feedback is one of the largest terrestrial-climate feedbacks, with strong positive effects on global warming (Schuur et al. 2008; Schuur et al. 2015; Schaefer et al. 2014).

On top of the permafrost, profound differences between winter and summer temperatures and incident solar radiation create seasonal freeze-thaw cycles of the topsoil – known as the active layer (Gomersall and Hinkel 2010; Shur, Hinkel, and Nelson 2005; Hall 2007). The complex interactions among active layer dynamics, soil properties, and vegetation composition and structure create striking landscape features

with distinct, and heterogeneous, micro-topography characteristics across scales: from small (<0.5 m) and larger (<10 m) hummocks to ice-wedge polygons (10-30 m), each showing unique spatial patterns (Sturm and Holmgren 1994; van Huissteden 2020) - figure 1). The spatial differences in soil ice content and associated vegetation cover have been shown to be the main drivers of micro-scale topographic patterns (van Huissteden 2020), along with surface hydrology and interactions with soil ice and vegetation. For example, freeze-thaw cycles cause ground ice accumulation in soil cracks, initiating a self-organizing network of ice wedges. This process creates the typical polygon pattern of tundra landscapes (figure 1c), with a dry elevated area along the edges and wet depressions above the ice wedges and in the center of the polygon (French 2007).

The spatial heterogeneity of micro-topography and the associated soil moisture and vegetation patterns importantly regulate below-ground processes, for example, soil hydrothermal dynamics that determine the spatial distribution of ground ice content, Active Layer Depth (ALD), and permafrost stability. In particular, while the soil thermal state is mainly driven by surface energy balance and ground heat fluxes, the spatial variation in surface albedo driven by changes in vegetation type, cover, and height can have strong impacts on seasonal permafrost freeze-thaw processes, an important determinant of ALD. Besides influencing the albedo, vegetation layers are also an important buffer between the atmosphere and soil by influencing both sensible and latent heat fluxes. Shifts in arctic vegetation are thus expected to alter ground heat fluxes and cause almost immediate thawing when removed (Blok et al. 2011; Nauta et al. 2014). In addition to vegetation, variation in micro-topography also plays an important role in ground heat fluxes and subsequently affects permafrost dynamics. This is because fine-scale terrain characteristics like slope and orientation can forge local drainage and soil moisture, affect snow cover and redistribution (Bennett et al. 2022), and drive fine-scale vegetation distribution and structure (French 2007; Cohen et al. 2014; Jorgenson et al. 2010; Romanovsky and Osterkamp 1995; J. P. Fisher et al. 2016). These complex interactions among climate, micro-topography, vegetation, and soil hydrology are

responsible for the high spatiotemporal variability found in permafrost dynamics, challenging our ability to quantify and model the spatial variation in ALD.

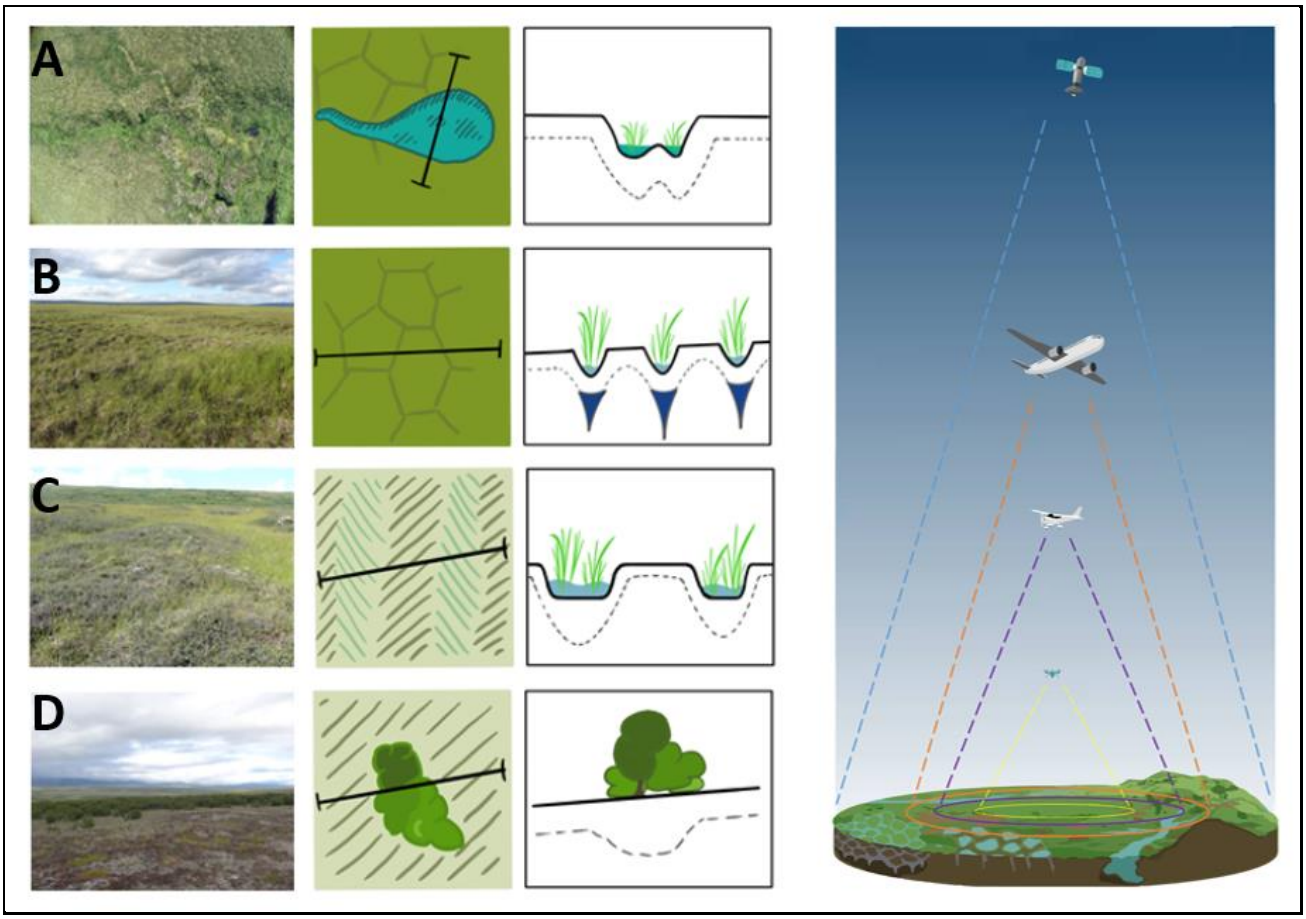

Figure 1.1: Conceptual overview of the thaw gradients covered in this thesis. a. Drained thaw lakes, leave small to large depressions in the tundra landscape. Typical vegetation: dry tussock- and dwarf-shrub tundra shifting to tussock-sedge, moss tundra in the depressions; b. Ice wedge polygon tundra with intermediate- and complete degraded ice wedges creating depressions above the ice wedge polygon structure, sometimes draining toward a water track leading to deeper channels. Polygon complex of wet graminoids and wet tussock sedges, while the polygon centers are dominated by dry tussock-sedge, dwarf-shrub lichen tundra; c. Water tracks in a moderate tundra landscape create a linear complex of wet sedges and dwarf shrub lichen tundra; d. Shrub encroachment in the tundra landscape. A complex of low-shrub tundra and tall shrub thickets. The average transect presented is approximately 50 m. The scaling diagram on the right shows a conceptual overview of the RS products, UAS, Airborne, and satellite, with their differences in altitude and spatial coverage (not to scale).

ALD is also highly vulnerable to disturbances. Press disturbances driven by anthropogenic climate warming are slowly changing the landscape and can cause an increase in ALD, melting the top of ice wedges and shifting low-centered to high-centered polygons with deeper waterlogged channels (Liljedahl et al. 2016; French 2007), or by pulse disturbances causing abrupt permafrost thaw and creating thermokarst features across the landscape (Grosse et al. 2011). Both types of disturbances change the hydrology of the landscape, the vegetation patterns, and the availability of soil C for decomposition thereby driving changes in surface and soil energy fluxes that affect ALD.

Despite the important interactions between above and below-ground processes, limited research has been done to quantify these connections and evaluate their potential to infer below-ground spatial variability in ALD, due to the remote location and logistic challenges to measure above- and below-ground properties simultaneously in tundra landscapes. Of all influencing factors, vegetation is relatively easy to observe using remote sensing (RS) and can act as a window to the underlying ALD and permafrost (Mikola et al. 2018; Döpper et al. 2021; Loranty et al. 2018), especially if combined with micro-topography data, to create a link between the above- and below-ground processes necessary to observe the fate of the permafrost. High-resolution data are necessary to capture the tundra heterogeneity (Muster et al. 2012), but permafrost landscape dynamics and associated disturbance effects are mostly observed at coarser spatial and temporal scales (Liljedahl et al. 2016). This scale mismatch among the key tundra processes makes it challenging to unravel the intrinsic connections between above and below-ground processes, limiting our ability to model and anticipate how ALD will respond to climate change and disturbances across different ecosystem types.

The recent development and use of new sensors and platforms like unoccupied aerial systems (UASs), allow us to observe vegetation, typography, and hydrology at high resolutions, providing new opportunities to understand the fine-scale connections between above and ground processes and facilitating upscaling to larger airborne and satellites. Recently, high-resolution airborne hyperspectral

imagery and high-resolution satellite imagery were used to model permafrost extent (Thaler et al. 2023) and active layer thickness (Zhang, Douglas, and Anderson 2021; Anderson et al. 2019; Gangodagamage et al. 2014) but the effect of the different sensors and scale of the RS product on the modeled permafrost features is not clear. Advances in UAS technology bridge the gap between ground-level and coarse-resolution remote sensing observations (Yang et al. 2020, 2022). Combining hyperspectral and UAS image processing allows for quick and detailed characterization of tundra vegetation and landscape patterns (Yang et al. 2023). Vegetation height and structure can be derived from UAS photogrammetry, together with a high-resolution elevation model, to detect soil subsidence and patterns in microtopography (Armstrong et al. 2018; Huang et al. 2018; Correll et al. 2019). UASs have been used to assess polygon tundra dynamics (Kartoziia 2019; Fraser et al. 2016) and the fractional cover of tundra vegetation used for upscaling to satellite data resolution (Yang et al. 2023; Zhang et al. 2020; Riihimäki, Luoto, and Heiskanen 2019).

In this chapter, we investigated to what extent RS captures the fine-scale variability in ALD through its connection with above-ground features like vegetation, topography, and hydrology. We analyzed how these connections vary across different representative ecosystem types and across a range of observational scales. We collected detailed field-based measurements of thaw depth across representative transects in combination with high-resolution UAS imagery covering our study sites on the Seward Peninsula, Alaska. The UAS imagery with a base resolution of 0.4 m was stepwise upscaled to 10 m and for each step, ALD was modeled with Random Forest. The explained variance was analyzed against the spatial resolution to identify the optimum modeling scale for the two study sites. To extend our approach to the broader landscape, we used hyperspectral datasets from NASA's Arctic-Boreal Vulnerability Experiment (ABOVE) AVIRIS-NG flight campaign (Miller et al. 2018) and Sentinel 2 to model the ALD at the watershed level. Model outputs were used to investigate the scaling effect across datasets and the dominant patterns in ALD were analyzed using wavelet and variogram analysis. The

upscaling process allowed for studying the impact of the spectral differences among the datasets at an identical resolution. Our modeling results show the predictive power of region-wide, medium-resolution ALD trends over the landscape, but the key permafrost features that are sensitive to change and a possible indicator of the resilience of the tundra landscape are only captured by the high-resolution UAS and AVIRIS-NG datasets. Determining the optimal synergy between the spatial patterns of tundra landscape features and the optimal scale of observation and analysis will help mitigate the influences of spatial-scale mismatches in modeling and improve the understanding of vegetation and permafrost changes in the Arctic.

1.2. Materials

1.2.1. Study Site

Our two study sites (Teller and Mile 80; figure 2) are located near Nome on the Seward Peninsula, western Alaska. The Seward Peninsula is located below the Arctic Circle on the Bering Sea coast and is a remnant of the historical Bering land bridge but is currently separated from Siberia by the Bering Strait. The Seward Peninsula is covered by tundra vegetation underlain with discontinuous permafrost (Peel, Finlayson, and McMahon 2007). The mean annual air temperature at Nome is -2.3C and shows a positive warming trend from 1976 to 2020, with pronounced changes during spring and fall while the winters are becoming slightly colder (https://akclimate.org/climate-change-in-alaska/). The Teller Road mile 27 site, hereafter called Teller, is characterized by coastal tundra with a topographic transition from wet meadow tundra on uplands to willow shrubland on lower slopes and along the streams (Raynolds et al. 2019). The Kougarok Road Mile 80 site, hereafter Mile 80, is categorized as interior tundra This site is characterized by a permafrost thaw pond, surrounded by non-active high-centered ice-wedge polygons. The pond was drained around 2005, causing increased drainage of the polygon landscape around the pond with decreasing soil moisture and increasing depths of the troughs surrounding the polygons. These changes subsequently triggered a landscape shift from wet graminoids to mesic plant

communities such as tussock sedges (Perreault et al. 2016). Through collaborations with the Next-Generation Ecosystem Experiments Arctic (NGEE-Arctic) (https://ngee-arctic.ornl.gov/) and NASA ABoVE (https://above.nasa.gov/), various field and airborne datasets, including AVIRIS-NG, have been collected at both Teller and Mile 80 sites (Miller et al. 2018).

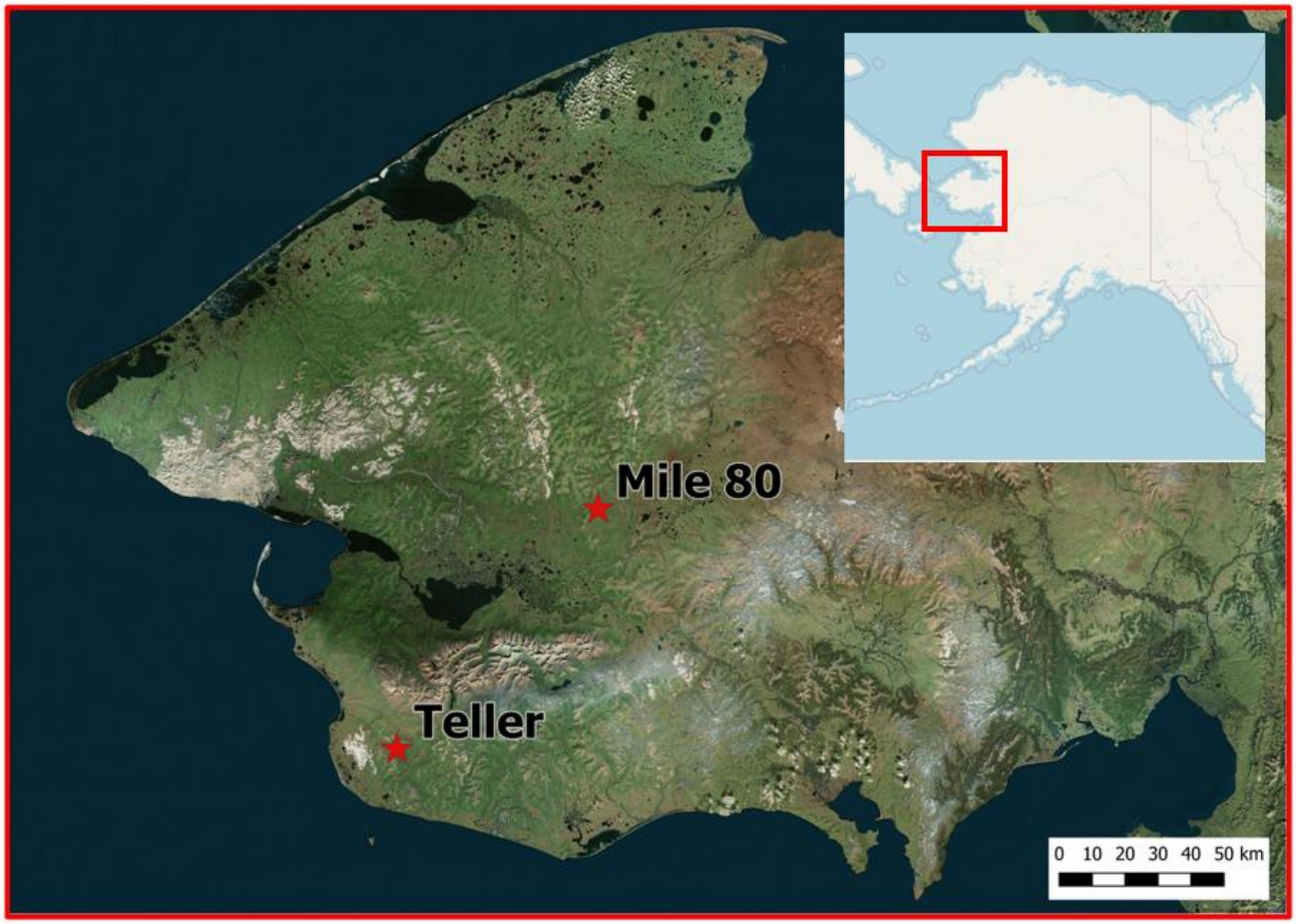

Figure 1.2: Location of study sites Mile 80 and Teller on the Seward Peninsula, Alaska, USA

1.2.2. Datasets

1.2.2.1. In Situ Active Layer Depth Measurements. In July 2019, we conducted a field campaign to collect field-based active layer depth (ALD) measurements across the Teller and Mile 80 sites. It is noted that this study focused on exploring the patterns of peak-season ALD, instead of maximum annual ALD, commonly referred to as active layer thickness (ALT) observed at the end of the growing

season. ALD generally increases proportionally to the square root of time since snowmelt (Nelson and Hinkel 2003), allowing to observe the spatial patterns in ALD variability before reaching the maximum thaw depth. We used a high resolution spatial sampling strategy to thoroughly capture the spatial variability of tundra vegetation, permafrost features, and disturbances (figure 1) by planning linear transects perpendicular to the elevation gradient (Teller) or crossing permafrost and thaw features (Mile 80) and avoiding alignment with vegetation and environmental gradients. At each sampling location, a thaw probe (130 cm long, 1 cm diameter, marked with 5-centimeter increments) was pushed into the ground until resistance of the permafrost layer was encountered. At locations with rocks or a high variability, multiple thaw depths were sampled within an area of about 2X2 m square, and the maximum thaw depth is reported. To link with remote sensing imagery, the coordinates of each location were measured using Garmin GPSmap and a portable Trimble Geo7X differential GPS. The Geo7X was connected to a Zephyr Model 2 Dual Frequency GNSS antenna (Trimble Incorporated, Sunnyvale, California) and coordinates were logged for at least 1 minute. The nearest base station data from the Trimble Reference Network (https://www.trimble.com/trs/findtrs.asp) were used to post-process the locations to achieve dGPS accuracy.

1.2.2.2. Remote Sensing Data. UAS imagery of the study sites was obtained with a Phantom 4 RTK drone in combination with the D-RTK 2 Mobile Station (DJI, Shenzhen DJI Science and Technology Ltd.), providing centimeter-scale geolocation accuracy for the UAS. The Phantom 4 is equipped with a built-in 1-inch, 20MP CMOS sensor with a mechanical shutter. Two and three UAS flights were collected at Teller and Mile80, respectively, under clear-sky conditions and a flight height of 100m. For this study, one flight for each site that covered our ALD sampling locations was used. Vegetation characteristics, canopy height, and digital elevation models were derived from photogrammetry point clouds processed with the Metashape (Agisoft LCC) software. We

processed UAS flight separately to create a 5 cm resolution RGB ortho mosaic and digital surface model (DSM), and based on non-vegetated pixels and local minima the digital elevation model (DEM) was generated from the DSM (Yang et al. 2020). Afterwards, the Canopy Height Model (CHM) was calculated as the difference between DSM and DEM. This UAS dataset is publicly available at https://doi.org/10.5440/1906348. The UAS imagery is characterized by an extremely high spatial resolution in the visible spectrum. The obtained resolution of 4 cm was initially reprocessed to a base resolution of 0.4 m. During the timeframe of UAS data collection, AVIRIS-NG flight lines were collected and made available by the NASA ABoVE airborne campaign (Miller et al. 2018). AVIRIS NG is an imaging spectrometer with 425 spectral bands and a wavelength range from 380 (visible) to 2510 nm (infrared); with 5 nm spectral resolution and a spatial resolution of 5 meters. The imaging spectroscopy data were collected on July 7 2019 and the orthorectified and atmospherically corrected reflectance product (L2) was downloaded from the AVIRIS-NG data portal (https://avirisng.jpl.nasa.gov/dataportal/). Compared to the airborne AVIRIS-NG, a Sentinel 2 satellite has 4 bands (RGB and NIR) matching the 10 m spatial resolution. The Sentinel 2 satellites (a twin configuration) have covered the whole world since June 2015 with a revisit time of only 5 days at the equator. A cloud-free, atmospherically corrected surface reflectance product (L2A) of Sentinel-2 imagery was downloaded from the Copernicus open-access hub (https://scihub.copernicus.eu/). The Sentinel 2 data were collected on July 6 2019 for Teller and July 8 2019 for Mile 80. The Arctic-DEM from the Polar Geospatial Center (Porter et al. 2022) was used for the AVIRIS-NG and Sentinel 2, encompassing the complete watershed area for both sites. Subsequently, the image dataset and DEM were clipped to the watershed level of the respective study sites. The Arctic-DEM strip that matched the AVIRIS and Sentinel-2 collection dates and

overlapped the study site were downloaded at resolutions of 2m (rescaled to match AVIRIS-NG) and 10m (https://www.pgc.umn.edu/data/arcticdem/) (Porter et al. 2023). This allows for each RS dataset to have a matching DEM.

1.3. Methods

1.3.1. Deriving Fine-scale Topographic and Spectral Features

Fine-scale topographic features such as ice-wedge polygon tundra, patterned ground, and solifluction lobes are important drivers of snow depth, hydrological processes, drainage patterns, and soil moisture that affect ALD (Hermes et al. 2020; Matsuoka, Ikeda, and Date 2005; Wainwright et al. 2015, 2017; Engstrom et al. 2005). However, these impacts remain poorly studied as these features happen at scales from a foot to several meters, hard to capture with traditional airborne or satellite DEM datasets (e.g. ArcticDEM). In this study, we addressed this problem by deriving topographic features that, considering the scale effects, can capture features at different scales and that we can apply to DEM datasets with different resolutions. Specifically, topographic variables representing fine-scale topographic position and water/energy distribution across the landscapes were derived, including slope, aspect, heat load index (HLI), topographic positioning index (TPI), terrain ruggedness index (TRI), convergence index (CI), and Topographic Wetness Index (TWI). The HLI is calculated based on the DEM using the R package "SpatialEco" (Evans and Ram 2021), and is a measure of incoming solar radiation that accounts for the differences in slope and aspect, for example, the temperature differences between south-facing and north-facing slopes. The TPI identifies terrain features, where a 0 value represents flat surfaces or smooth slopes, < 0 TPI indicates valley bottom or gully, and > 0 TPI represents ridges. TRI provides a measure of the ruggedness of the landscape, ranging from level to extremely rugged, based on the elevation differences within the defined neighborhood (here at 5, 25, and 50 m). The Convergence Index (CI) represents the structure of the terrain by peaks and ridges/pits and channels for the defined neighborhood. As the scale is important the CI highly depends on the size of the neighborhood (here at

5, 10, 15, 25, 50, 75). TWI can be seen as the likelihood of water accumulating in the landscape and is used to represent soil moisture (Winzeler et al. 2022). TWI is calculated based on the specific catchment area, the contributing upslope area divided by the flow width, and the grid slope (R - RSAGA & SAGA GIS (Conrad et al. 2015)). To standardize the imagery was transformed to the first three bands of the Principal Components Analysis (PCA). To take advantage of the information stored in the AVIRIS hyperspectral bands, spectral traits and indices related to vegetation and soil were calculated and included as covariates. Table 1 (Supplemental material) provides an overview of all covariates. The topographic and spectral covariates are calculated for each RS dataset and used in the modeling approach.

1.3.2. Modeling ALD with Random Forest

Using ALD measurement across transects (section 2.2.1) in combination with spectral and topographic derivatives from our RS products, we developed a spatially explicit Random Forest (RF) model to predict and map ALD across our study landscapes. The spectral and topographic derivatives are used in the RF model, as described in 3.1. The RF machine learning algorithm (Breiman 2001) was selected since it is relatively easy to use without much parameter tuning and still outperforms other ML algorithms, particularly on relatively small datasets (Genuer, Poggi, and Tuleau-Malot 2010).

1.3.3. Scaling Analysis

To facilitate the scaling of ALD from individual sites (studied with in situ measurements and UAS imagery) to the larger landscape (observed with airborne and satellite imagery), and across tundra vegetation, permafrost-, and disturbance features, we conducted comprehensive, multi-scale, and multi-resolution analyses. First, we examined the impacts of spatial resolution on modeling ALD by training the RF using UAS derivatives datasets resampled to a range of resolutions (i.e 0.40 m to 10 m at 0.8 m interval). In this process, we identified the optimum modeling scale for the two study sites (see section 2.4.1). This analysis provided a ‘clean’ investigation of spatial scaling effects on modeling ALD.

After that, we re-trained the RF using datasets from AVIRIS-NG and Sentinel 2, along with the matching Arctic-DEM at the watershed level of both study sites. This allowed us to model ALD and extend our approach to encompass a broader landscape. We compared the model outputs from UAS, AVIRIS-NG, and Sentinel-2 to investigate the scaling effect across UAS datasets with upscaled resolutions (see section 2.4.1), different sensors, and landscape features (see section 2.4.2). Lastly, the upscaling process allowed the synchronization of resolutions among the upscaled UAS, AVIRIS-NG, and Sentinel 2 and enabled us to examine the impact of the spectral differences among the datasets at an identical resolution.

1.3.4. Identifying Optimum Feature Scale for Modeling ALD

The mismatch between the scale at which ecological processes happen and the scale of observation strongly impacts modeling ecological patterns with remote sensing data. Either over- or under-sized observation could lead to reduced model uncertainty due to the occurrence of salt-and-pepper noises at fine scale and aggregation of information at large scales. Identifying the optimal scale that best captures above-below ground relationships for different landscapes can guide us toward the most predictive scale for ALD modeling. In this study, the high-resolution UAS base layers including RGB and DEM, are stepwise upscaled with increments of 0.8 m, aggregating from the base resolution of 0.4 m to a maximum resolution of 10 m. This resulted in a series of resolutions for which the remote sensing derivates were extracted. For each step, the scaled orthoimage and DEM were used to calculate the modeling covariates, the RF model was trained and subsequently, ALD was modeled across all grain sizes. To identify the optimum modeling scale, the explained variance of the RF model was plotted against the grid size, where the maximum explained variance will represent the optimum modeling scale.

1.3.5. Comparing UAS, AVIRIS-NG, And Sentinel 2 for Modeling ALD

We compare the ability of three datasets, UAS, AVIRIS-NG, and Sentinel-2, with a spatial resolution of 0.4, 5.1, and 10 m respectively, for modeling ALD. These datasets were used to calculate covariates for ALD modeling. Integrating these different resolutions and spatial sales allowed us to model ALD and extend our approach to encompass a broader landscape context. We used a spatial covariance approach to analyze the modeled ALD patterns versus spatial heterogeneity of the different ALD models with different spatial resolutions. We calculated a series of variograms to describe the spatial dependence of the ALD model results for the different sensors and different landscape patterns, with the variogram attributes descriptive of the scale and intensity of dominant patterns detected in the modeled ALD (Murwira and Skidmore 2005; Rietkerk et al. 2000). On the other hand, a Wavelet transform was calculated to analyze the scale variability of dominant patterns. The wavelet transform has its roots in signal processing and is based on the Fourier analysis, which decomposes a signal into sinusoidal frequency components but loses its spatial reference (Broughton and Bryan 2011). Wavelets enable analysis across scales in the spatial domain by providing a location-scale analysis. The wavelet spectrum is calculated for a scalable moving window shifted over the transect, and a stepwise increase in window size creates a multi-resolution analysis in space. The increased data aggregation allows an analysis of the scale variability of the dominant patterns in space. The ability to detect features within transects at varying spatial scales makes a wavelet analysis a versatile analytical tool for detecting feature variability across scales and allows us to uncover complex patterns and structures in our landscapes (Dale and Mah 1998; Csillag and Kabos 2002; Murwira and Skidmore 2005). We visualized the wavelet analysis using the wavelet power spectrum where the X-axis represents the location along the transect while the Y-axis represents the feature scale, where Y=1 corresponds with the original pixel size. When moving up the Y-axis the wavelet scale is aggregated by factor 1-2-4-8-16... The associated edge effects with increased aggregation create a window of applicability of the wavelet power spectrum. We used the R

package WaveletCom to calculate the power spectrum, identify significant patterns, and visualize the window of applicability (Rösch and Schmidbauer 2018).

To quantify the dominant scale, we selected landscape features with distinct spatial and vegetation patterns observed across various spatial scales at each study site. For Mile 80 (see figure 1.8 for matching figures), the three landscape features with distinct micro-topography characteristics and spatial pattern(s) were: A) Tussock tundra, B) Ice-wedge polygons, and C) the thaw pond. For the Teller site, the landscape features selected were: A) Gully with shrub encroachment along the banks, B) Water tracks with distinct linear patterns of drier upland dwarf shrubs and wetter sedge-dominate depressions, and C) Shrub patches. The spatial autocorrelation, or patchiness, of the modeled ALD was calculated using a variogram analysis. Furthermore, wavelet analysis was applied to detect spatial patterns across scales for the three landscape patterns, allowing the detection of the different features present in the tundra landscapes. The results derived from these analyses allow for a detailed understanding of the tundra and landscape patterns observed and ALD modeled by the UAS, AVIRIS-NG, and Sentinel 2 datasets. The spatial patterns detected by the different platforms were compared with the OFS derived from the scaled UAS ALD model. We then compared and analyzed the model outputs from UAS, AVIRIS-NG, and Sentinel to investigate the scaling effect across different datasets, resolutions, and landscape features.

1.3.6. Comparative Analysis of spectral Properties of UAS, AVIRIS-NG, and Sentinel 2 for Thaw Depth Modeling

The upscaling process facilitated the alignments of ALD model outputs based on resolution among the upscaled UAS (2.4.1) and AVIRIS-NG and Sentinel (2.4.2), enabling an analysis of the impact of spectral resolution among datasets. In our analysis, we compared the matching datasets derived from UAS with AVIRIS-NG, and Sentinel 2 for their ability to model ALD, considering the different spectral resolutions of each dataset.

The UAS imagery is characterized by 3 spectral bands in the visible spectrum (Red, Green, Blue - RGB) with a base resolution of 0.4 m and upscaled resolutions of 5.1 and 10 meters to match AVIRIS-NG and Sentinel-2, respectively. The upscaled ALD model results are used as a base model. Conversely, the Sentinel 2 satellite has 4 spectral bands matching the 10-meter spatial resolution covering RGB and a Near Infrared (NIR) band.

1.4. Results

1.4.1. Field-based Active Layer Depth

The active layer depth was measured along 6 transects at Teller (collected on 17/07/2019) and 4 transects at Mile 80 (collected on 12/07/2019) during the 2019 field season. The ALD ranged from 15 cm to 120 cm and 18 cm to 100 cm, respectively, for Teller and Mile 80, with much larger spatial variation at Teller than Mile80 (mean ALD: Teller 72.7±25.9 and Mile 80 38.7±12.5). The larger spatial variation in ALD at Teller is associated with vegetation patterns (Yang et al., 2019). The deepest mean ALD was associated with wet graminoids (89.8±21.6 cm) and forbs (e.g. horsetail/coltsfoot - 79.4±20.9 cm), followed by tall willow shrubs (77.6±23.5 cm) and dry graminoids (75.2±26.5 cm). The lowest mean ALD was observed for deciduous low shrubs (e.g. dwarf birch and bog blueberry - 58.9±21.9 cm). The difference between the means of deciduous low shrubs and tall willow, dry graminoid, and wet graminoid is significant ($p < 0.05$). We used one-sided ANOVA to test the difference between groups ($p < 0.01$) followed by the Tukey HSD ($p < 0.05$) to identify the specific groups with significant differences. However, at Mile 80, no significant differences were observed in mean ALD between the two main vegetation types tussock tundra (39.3±14.9 cm) and deciduous low shrub (38.4±11.5 cm).

1.4.2. Characterization of Key Covariates

The covariates were selected to capture and represent the diverse land surface variation present at the study sites. At Mile 80, the DEM shows overall minor elevational variation over the tussock tundra,

creating a gently rolling landscape with a slight curvature. Interestingly, the micro-topography was able to capture the existence of polygons (figure 1.1b), where the slightly elevated polygon centers are covered with deciduous low shrubs, and the depressions above the ice wedges are covered with sedges (left panel in Figure 1.3). The site features a central thaw pond and a drainage channel from that pond towards a stream. The thaw pond, measuring 100 by 150 meters and almost 1.5 m deep, is a dominant disturbance feature increasing drainage from the surrounding polygon tundra. At Teller, the elevational gradient is south-southeast oriented, with relatively steep slopes along the central stream. Microtopographic variation includes linear patterns along the slope with distinct graminoid (depressions) and deciduous low shrub cover, and deeper water tracks with wet graminoid vegetation. Along the stream, willow patches are mixed with wet graminoids, forbs (horsetails), and deciduous low shrubs. The calculated Convergence Index (Thommeret, Bailly, and Puech 2010) with varying kernel sizes reveals different landscape patterns, as presented for Mile 80 in Figure 1.3. A smaller kernel size accentuates features associated with polygon tundra, an intermediate kernel size highlights the main drainage channels, and a large kernel size highlights disturbances like the distinct thaw pond.

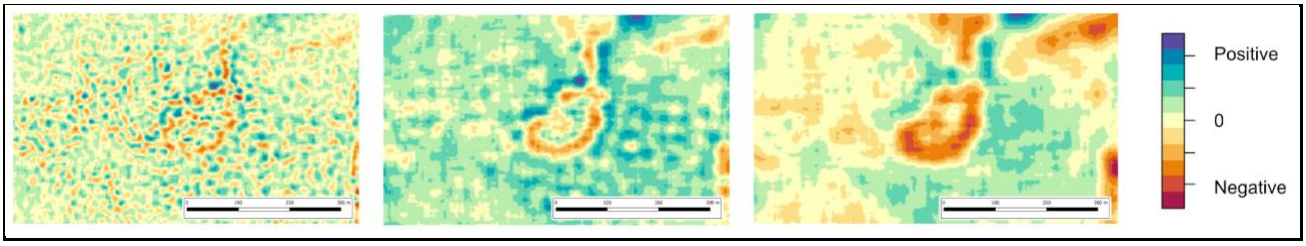

Figure 1.3: Micro-topographic spatial patterns defined by the Convergence Index (CI), with different neighborhood sizes (25-49-75 pixels) — an example from the Mile 80 study site based on UAS-derived DEM with a resolution of 0.4m. Convergent or channels are represented in red (negative CI), yellow represents a more planar surface (CI=0), and blue highlights divergent or ridges (positive CI).

1.4.3. Modeled Active Layer Depth

1.4.3.1. UAS-based ALD modeling and Scaling Across Grid Size. The modeled ALD of the gradually upscaled high-resolution UAS base layers with a resolution of 0.4 m up to a maximum resolution of 10m. ALD was modeled across all grain sizes, and the RF model's explained variance was plotted against the grid size. Figure 1.4 visualizes the changes in the explained variance of the RF model with increasing grid size for both study sites and reveals a distinctly different trajectory for both sites. For the Teller site, the model accuracy increased initially and peaked around a spatial resolution of 5 m before showing a slight decrease towards the lower resolutions. In contrast, the explained variance for Mile 80 peaked at the highest resolution before quickly dropping with increased spatial grid size.

When visually examining the spatial patterns, the Teller site (figure 1.4b) shows pronounced landscape patterns for the mid- to low-range resolutions (2.8 to 10.0 m), including the peak 5 m resolution. The high-resolution model output comparatively lacked spatial patterns, while speckled model output is observed at large pixel sizes. Instead at Mile 80 (figure 1.4a), high-resolution model outputs well observed the spatial structures associated with tundra polygons. These spatial structures were diminished with decreasing model resolution, especially when the modeling resolution is over 2.8 m.

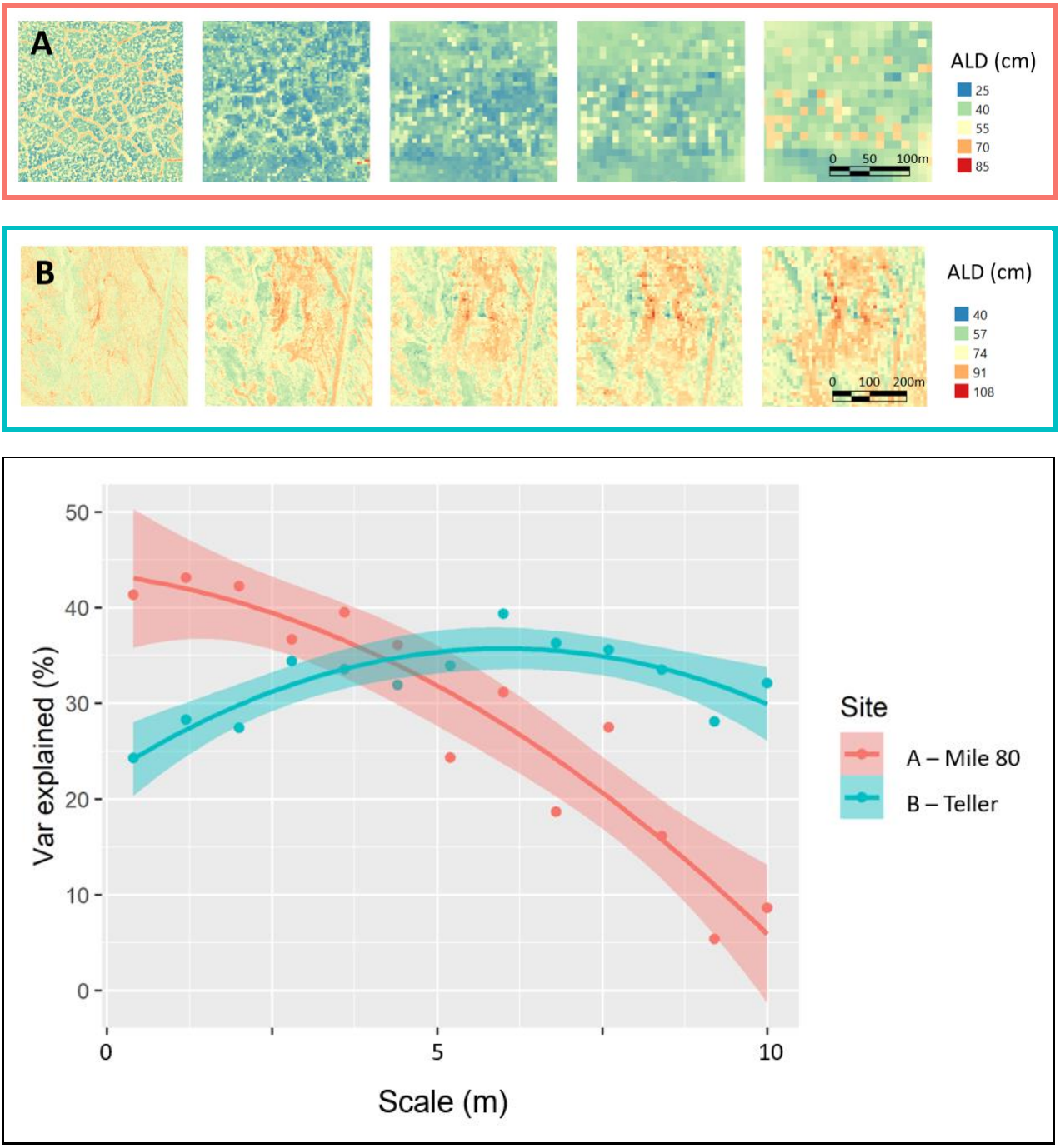

Figure 1.4. Active layer modeling results with changing resolutions. A &B: UAS model results for ALD with increasing grid size ranging from 0.4m to 10 m, with intermediate steps of 2.8, 5.2, and 7.6 m presented (A = Mile 80, B = Teller). Note the difference in scale and the associated size of the landscape features in both landscapes. Figure 4 bottom: Scale of the RS dataset used to model ALD plotted against the explained variance by the model. The plot shows the difference in behavior between Mile 80 and Teller, where Mile 80 peaks at the smallest scale, quickly dropping with increased resolution the models for the Teller site reach their optimum around 5m resolution, with a slight drop with the lower and higher resolutions.

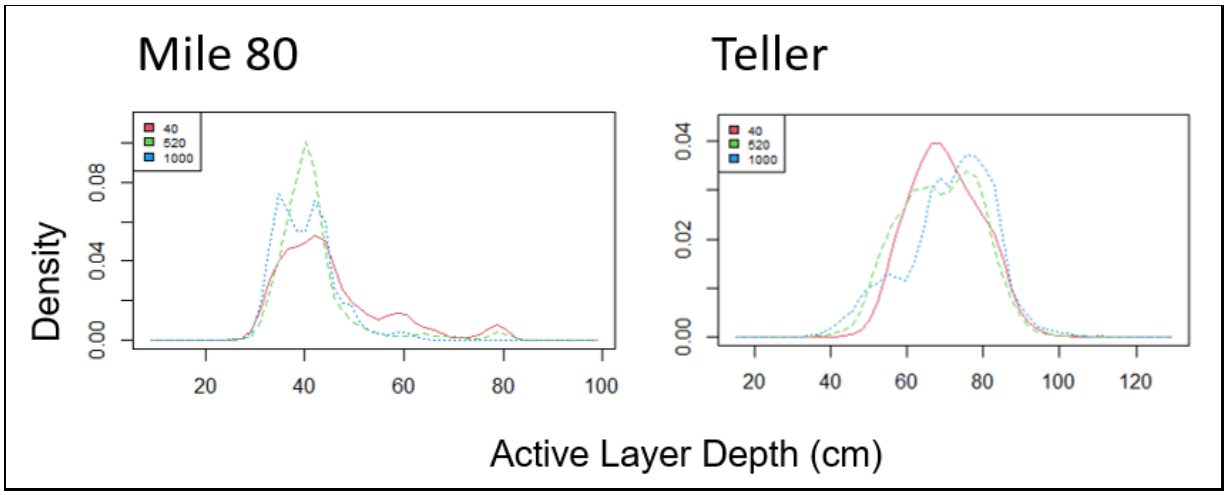

Figure 1.5: Density plot of UAS model results for ALD with grid sizes 0.4m, 5m, and 10 m for Mile 80 and Teller study site.

Figure 1.5 shows the distribution of the modeled ALD values for both the Mile 80 and Teller study sites, for resolutions 0.4 m, 5, and 10 m. Different ALD prediction patterns are observed for the two study sites. For Mile 80 (figure 1.5 - left), the ALD predictions are largely centered around a mean of 40 cm, which is close to the observed ALD mean of 38.7 cm derived from the transect-based, in situ ALD measurements. Only the high-resolution model represented the spatial ALD variability, allowing the model to predict and capture variation in the deeper ALD values beyond the average. For Teller (figure 1.5 - right), the model outputs for the different resolutions show similar mean ALD values that align with the mean transect ALD of 72.7cm measured in the field. At 10 m resolution, the model slightly overestimates ALD while at 0.4 m there is a slight underestimate of ALD. Overall, the models at Teller effectively capture the average ALD compared to the mean of the transect ALD measurements.

1.4.3.2. Multi-platform Based ALD Modeling Across Grid Size and Landforms. For the multi-platform comparison, ALD was modeled using the high-resolution UAS base layer, the AVIRIS-NG, and the Sentinel 2 imagery with respectively 0.4 m, 5.1 m, and 10 m spatial resolution (figure 1.6). We analyzed the model outputs for spatial patterns by variogram and wavelet analysis. These tools

allowed us to study how the different landscapes are represented across scales and sensors. Splitting the landscapes into their distinct landforms, variograms, and wavelets allowed us to study the distinctive differences captured by our model across both scale and landforms. Details of the model outputs from UAS, AVIRIS-NG, and Sentinel 2 for the Teller (Top) and Mile 80 (bottom) study sites are presented in Figure 1.6.

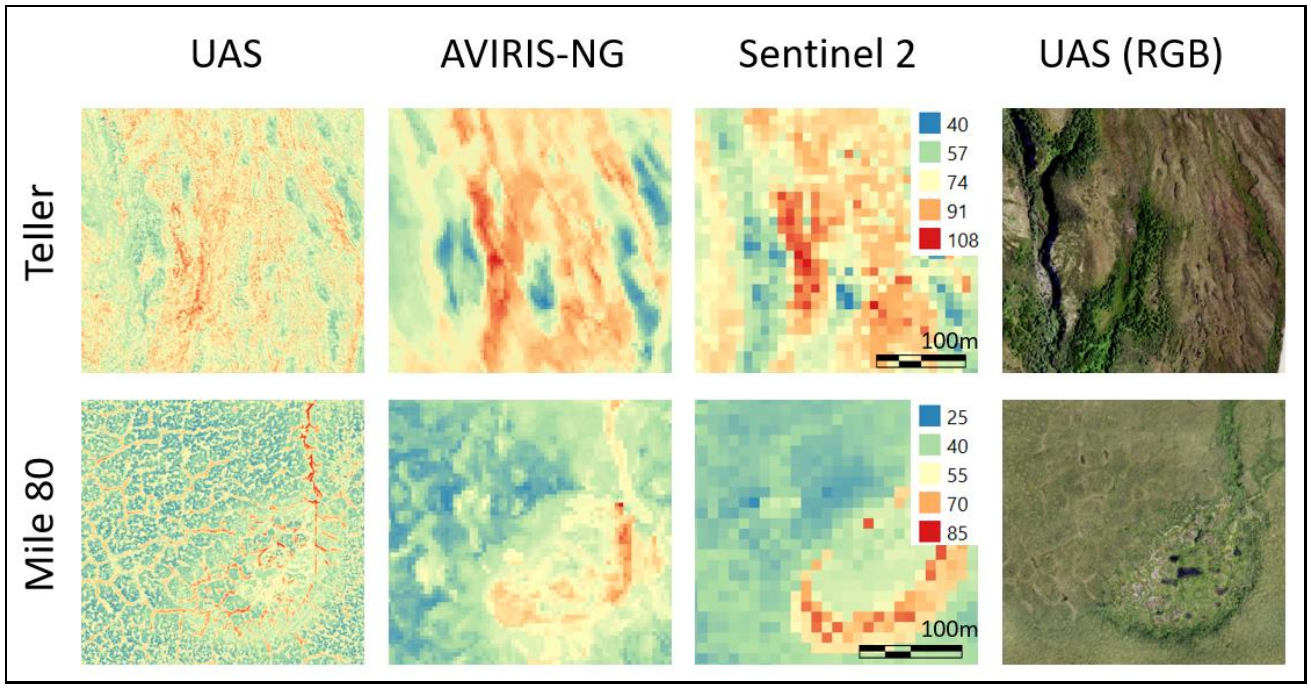

Figure 1.6: Multi-platform model results from the Teller site (top) and Mile 80 (bottom). A detail of the ALD model results are presented from left to right: UAS (0.4 m), AVIRIS-NG (5.1 m), Sentinel 2 (10 m), and the UAS RGB image (0.4 m) for reference.

For Mile 80, the key landforms present include tussock tundra, polygon tundra, and a drained thaw lake. To get insights into the distribution of the modeled thaw depth across landforms and pixel size/dataset, we extracted details from the study sites that explicitly cover the landforms of interest (figure 1.7). The density plot shows that all the datasets cover the variability of ALD for the thaw pond (C). However, the tussock tundra and polygon tundra show contrasting results. Only the high-resolution model could capture the variability in ALD associated with the tussock tundra

(A) and polygon tussock tundra (B) features. Deeper ALD values were not present in the AVIRIS-NG and Sentinel models. For Teller, key landforms present include (A) gullies with shrubs, (B) water tracks, and (C) areas of shrub encroachment. Concerning the distribution of modeled thaw depth across the landforms (figure 1.7), the density plot shows that all datasets cover the mean ALD, while the medium to low-resolution model has a wider spread compared to the high-resolution model.

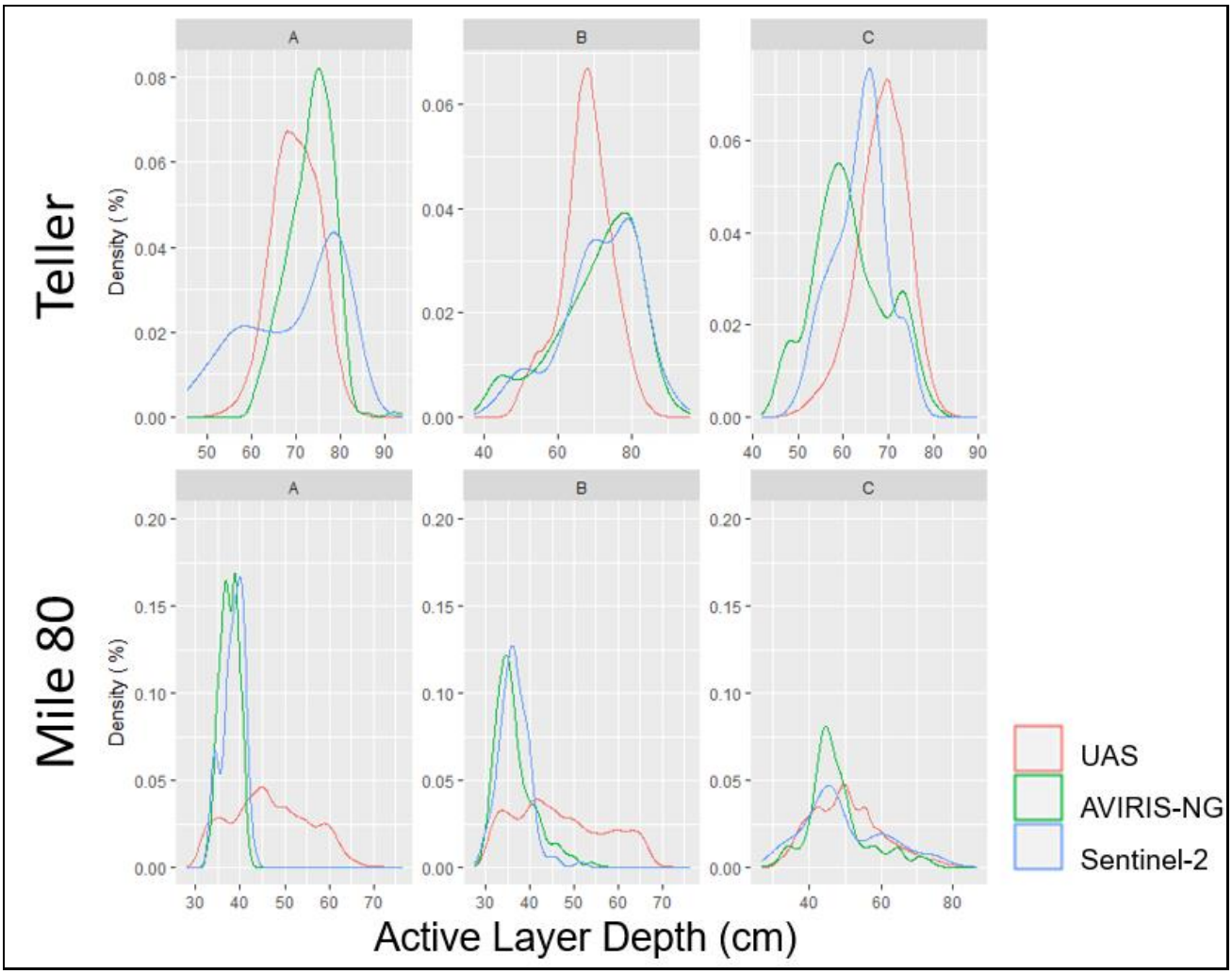

Figure 1.7. Density plots showing the distribution of modeled ALD across key landforms and platforms. Landforms covered by Mile 80: (a) tussock tundra, (b) polygon tundra, and (c) drained thaw lake; and Teller: (a) gullies with shrubs, (b) water tracks, and (c) shrub encroachment.

The spatial variation in the modeled ALD was analyzed using a variogram analysis (figure 8). Overall, observed spatial patterns in modeled ALD decreased with coarsening resolution. Compared to AVIRIS-NG and Sentinel, the semivariance of the UAS modeled ALD peaked for the three examined landscape types, with a larger range value for thaw lake and polygon tussock tundra (range: 4.7 m for both), compared to tussock tundra (range 2.9 m). The observed pattern in range corresponds with the spatial size of the features in the landscape patterns for tussock tundra (A) < polygon tussock tundra (B) and thaw lake (C). In contrast, the AVIRIS-NG model shows no autocorrelation for tussock tundra, capturing only the polygon tundra and thaw pond. The increased range for polygon tundra variogram, along with a large nugget to partial sill ratio, indicate a weak spatial structure. The thaw lake variogram tends to flatten, but still displays a linear increase, indicating a trend in ALD over the landscape. Finally, the Sentinel-2 model only captures the thaw pond, yet again showing an increased range, a linear trend, and a large nugget-to-partial sill ratio, suggesting a weak spatial structure. The variogram for (A) and (B) exhibit a pure nugget effect (a straight horizontal line) without spatial structure. For Teller (figure 1.8), variogram output from the UAS model shows a strong, short-ranged spatial autocorrelation pattern that is observed for both landforms related to shrubs, while the water tracks variogram tends to reach a sill twice, indicating a potential anisotropic pattern. The AVIRIS-NG model reveals a long-range spatial dependency for water tracks while showing weak to no spatial dependency for both other landforms. Sentinel-2 model output captured a weak spatial autocorrelation characterized by a large nugget-to-partial sill ratio for the water tracks, a pure nugget effect for shrub encroachment, and a linear trend for the gully suggesting a trend over the modeled landscape.

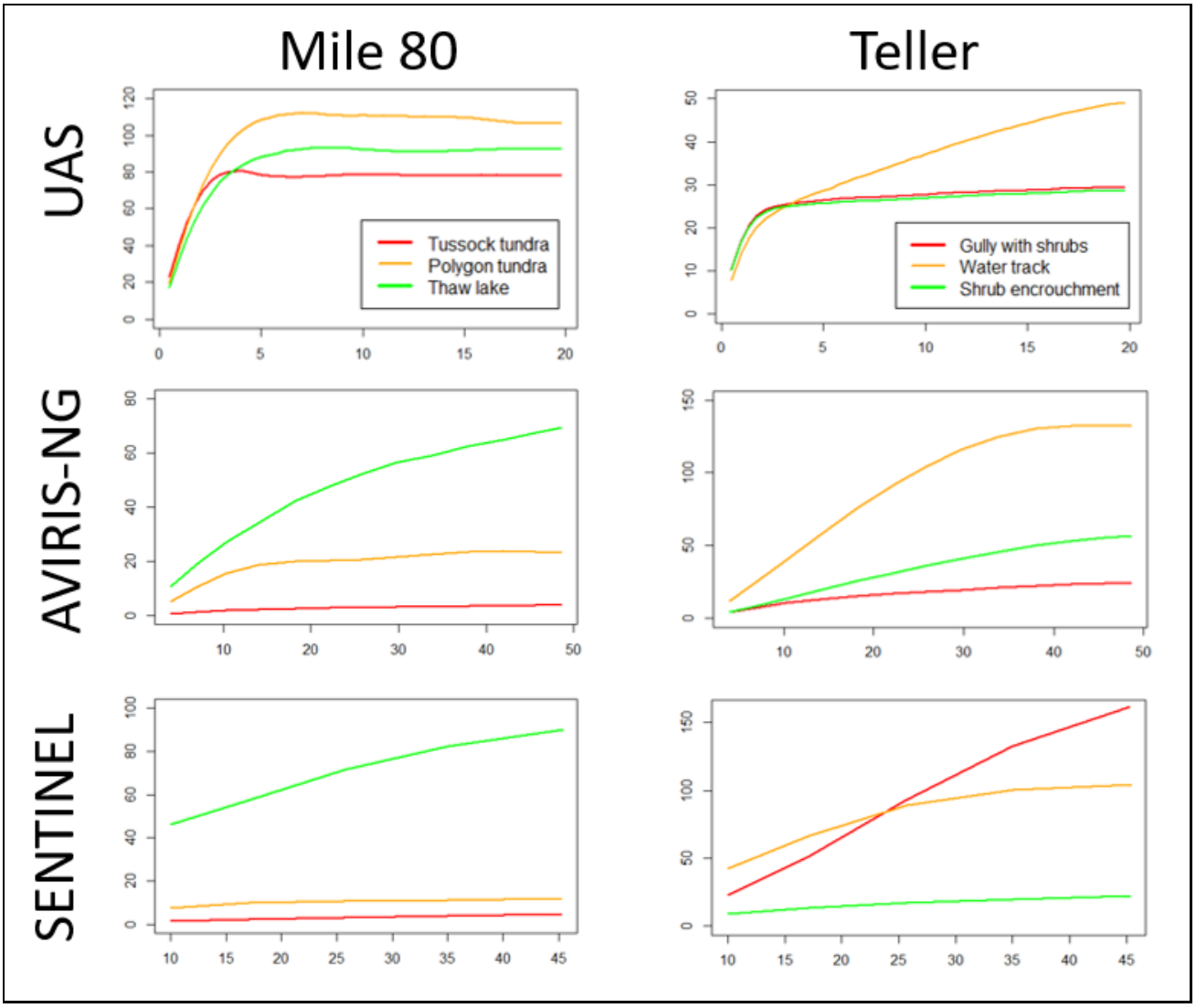

Figure 1.8: Multi-platform variogram analysis of the ALD model output from the Mile 80 (left) and Teller site (right). Comparison between RS platforms from top to bottom: UAS (0.4 m), AVIRIS-NG (5.1 m), Sentinel 2 (10 m) and different landforms. The landforms for Mile 80 are tussock tundra, polygon tundra, and thaw lake; and for Teller a gully with shrubs, water tracks, and shrub encroachment. The variogram graphically depicts the spatial structure within the model output. A typical variogram has an increasing spherical shape, reflecting the increased variation or dissimilarity in the data until it reaches the range. Beyond the range, no correlation is observed. Variogram models showing a linear increase indicate a trend over the modeled landscape and variogram models represented by a straight line signify no spatial structure and are referred to as exhibiting a pure nugget effect.

We performed a wavelet analysis to study Mile 80 in more detail. The dominant frequencies identified along the UAS transect covering Mile 80 (figure 1.9) manifest with peak powers in the frequency bands centered around 8, 24, and 64, corresponding to real-world periods of approximately 3.2 m, 9.6 m, and 25.6 m, respectively. Analyzing the spatial variation within the transect reveals a distinct pattern: a strong signal with a period of 8 is most prominent in the initial quarter of the plot, while the signal with period 24 dominates the second quarter. The largest period dominates around the center of the transect. Translated to the context of tundra landforms, the shorter periods align with the Tussock tundra vegetation patterns (figure 1.9a), the intermediate period correlates with the characteristic polygon tundra (figure 1.9b), and the largest period of around 25.6 m aligns with the presence of the thaw pond situated in the middle of the transect (figure 1.9c). Comparing the observed patterns within the AVIRIS-NG and Sentinel-based transect indicates a consistent pattern. Although the fine-scale patterns associated with tussock tundra and polygon tundra are absent, large-scale patterns were observed at the center of the transect, aligning with the thaw pond.

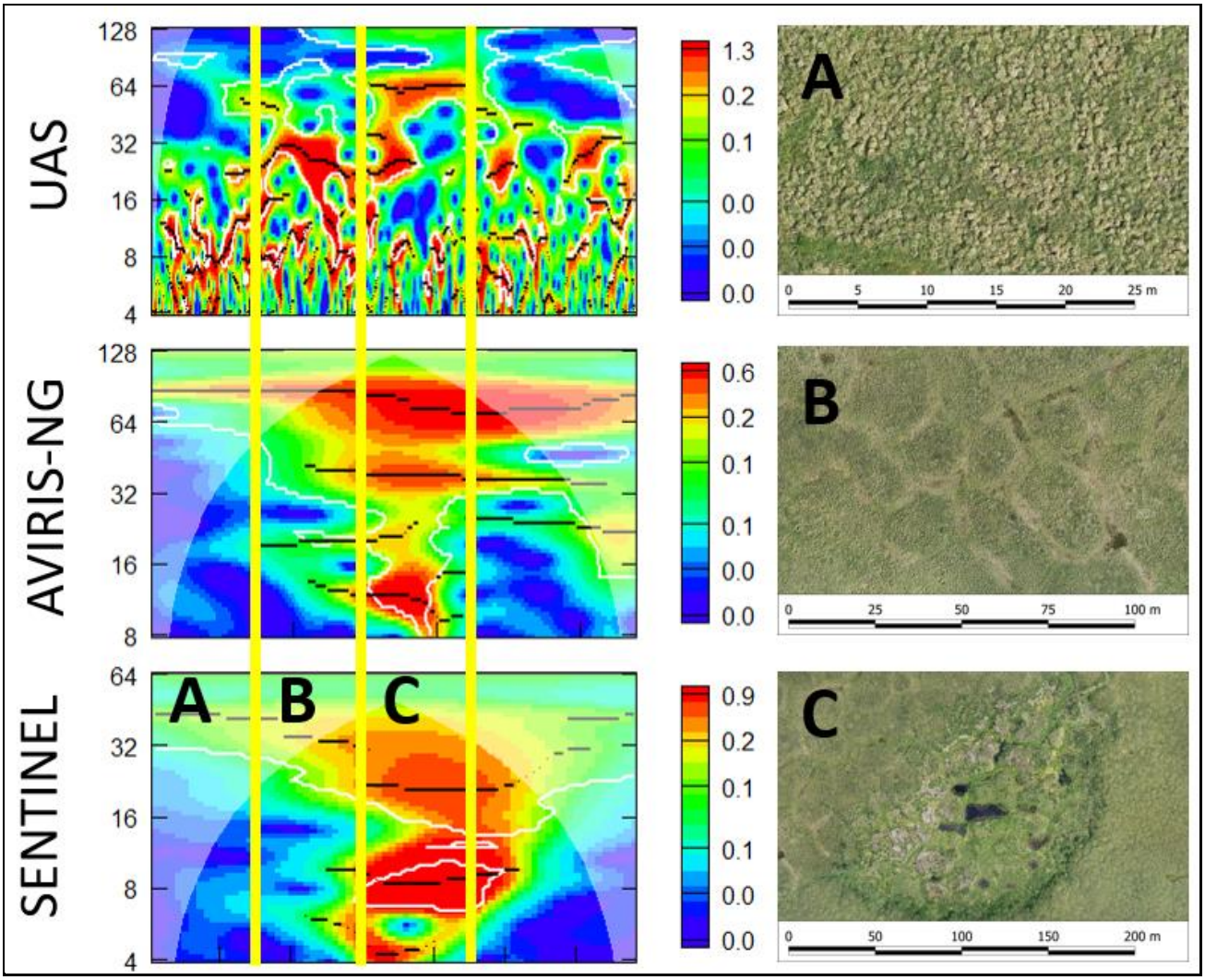

Figure 1.9: Wavelet analysis of the different platforms and landforms of Mile 80. To quantify the dominant scale for different landscape features with distinct micro-topographic characteristics and spatial pattern(s) we selected a subset of the Mile 80 study site covered with: A) Tussock tundra, B) Ice-wedge polygons, and C) Thaw pond. The transect used for the wavelet analyses covers first (A) tussock tundra, and second (B) polygon tundra with (C) a drained thaw lake followed by a mixture of tussock tundra with degraded polygon tundra for the rest of the transect. The wavelet spectrum (left), with the distance along the transect on the X-axis and the scale on the Y-axis, visualizes the significant patterns by scale along the transect. Power ranges from purple (low) to red (high), and the 5% significance level is delineated by white lines.

1.4.3.3. Multi-platform Based ALD Modeling Across Grid Sizes and Spectral Resolutions. To investigate the influence of spectral resolution on the ALD modeling, we compared outputs from the upscaled UAS-based model with those derived from the AVIRIS-NG and Sentinel-2 datasets,

respectively (figure 10). Visually, the spatial structure of Teller seems preserved in all model outputs and looking at the correlation the AVIRIS-NG and Sentinel-2 based (R2 0.76 and 0.77) models both outperformed the upscaled UAS imagery at an identical resolution (R2 0.64 and 0.70) indicating the added value of the spectral information in AVIRIS-NG (an increase of 0.12) and the NIR band of sentinel (an increase of 0.06). A similar but stronger pattern is visible for mile 80. Increase of R2 by 0.18% for the AVIRIS-NG-based model compared to the upscaled UAS and 0.21% for the Sentinel-based model.

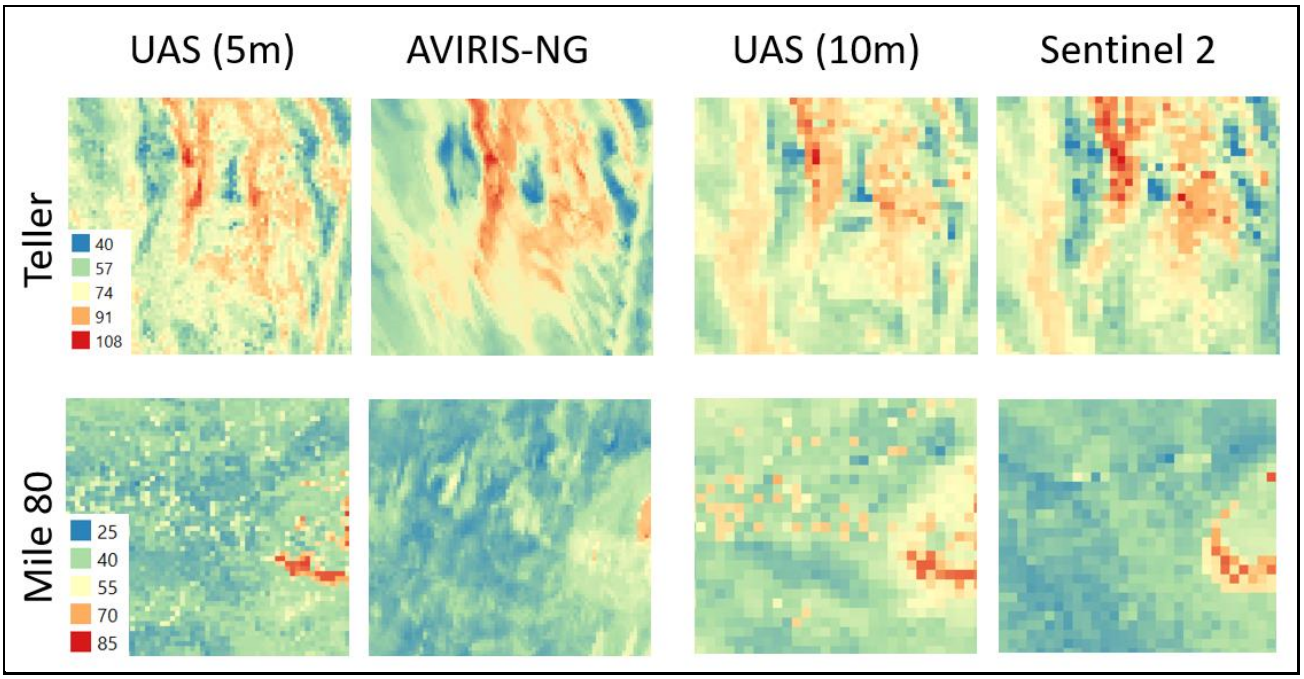

Figure 1.10: Effect of spectral resolution on the multi-platform model results from the Teller site (left) and Mile 80 (right). A detail of the ALD model results are presented from left to right: 0.4 m, RGB and ALD), AVIRIS-NG (5.1 m), and Sentinel-2 (10 m).

Table 1.1: Correlation coefficient between ALD field measurements and modeling output.

Correlation	UAS (5m)	AVIRIS-NG	UAS (10m)	Sentinel 2
Teller	0.64	0.76	0.70	0.77
Mile 80	0.44	0.62	0.34	0.55

1.5. Discussion and Conclusion

We evaluated the ALD model outcomes for a large range of spatial scales across different tundra landscapes on the Seward Peninsula, AK. We compared 3 commonly used sensor platforms, each with their specific spectral and spatial resolutions: UAS, AVIRIS-NG, and Sentinel-2. As base layers, we upscaled the high-resolution 0.4 m UAS imagery to match the 5.1 m AVIRIS-NG and 10 m Sentinel-2 Imagery.

Tundra landscapes are characterized by a high environmental complexity that results from vegetation permafrost interactions and landscape dynamics, all influenced by external drivers such as weather patterns and the changing climate. Environmental heterogeneity is also recognized as the key driver of species richness, but such relationships are strongly affected by the spatial scale of analysis (Stein, Gerstner, and Kreft 2014). The link between vegetation community attributes and permafrost condition (Standen and Baltzer 2021) makes effectively capturing this heterogeneity crucial for the accurate modeling of ALD. Detecting the extremes in ALD, particularly in ice-rich tundra where a sudden increase in thaw depth can trigger catastrophic thaw, can dramatically alter the landscape.

Our study, based on upscaled UAS imagery, revealed that an optimal characterization of the tundra landscape largely depends on the spatial heterogeneity and size of the landscape features. A key factor in modeling the ALD of the tundra landscape involved considering the scale of common tundra vegetation, permafrost, and disturbance features. The identification of the Optimum Feature Scale **(**OFS) via a multi-scale modeling approach allowed us to detect the scale at which the RF model excels in capturing the ALD variability across the landscape. The spatial scales aligned with the observed landscape heterogeneity outperformed the other scales. To achieve high-precision modeling results, the observations must match the permafrost and/or ecological feature scale, and pixel size used by the RS products. On the other hand, although high-resolution model results demonstrated excellence in some cases (e.g. at the Mile 80 site), medium-resolution models covering larger landscape features

outperformed them for the Teller site. This underscores how a stratified approach might be required to optimize the modeling of the tundra landscape. The medium-resolution model, using AVIRIS-NG, also benefits from the added value of the high spectral resolution to improve the medium-resolution model outcomes.

Our findings indicate that low-resolution predictions show less contrast compared to high-resolution predictions (Thompson, Bell, and Butler 2001), but medium-resolution models are good predictors of average thaw depth even at a site with high heterogeneity. And while average thaw depth predictions have proved valuable, when studying the resilience and future trajectories of the ABR it is important to observe local (disturbance) features at the matching scale. For example, the small-scale (micro-)topography and vegetation patterns observed in polygon tundra, present in the landscape at mile 80, have similar underlying ALD patterns driven by the presence of ground ice wedges. Disturbances associated with ice wedges characterize the different polygon tundra disturbance stages. Observations from mile 80 for the polygon tundra landscape demonstrate ALD patterns with above- and below-surface spatial variability as described by (Siewert et al. 2021). Increased disturbances caused by the drained thaw lake changed the local and regional hydrology, where water tracks may have contributed to the thaw lake drainage (Trochim et al. 2016). The increased water drainage deepened the troughs, leading to dryer and wider troughs by removing the insulation moss cover above the ice wedges.

By analyzing this landscape at high resolution, we conclude that the increased drainage could drive tundra landscapes to shift back to aerobic respiration resulting in a greater proportion of CO2 compared to the higher CH4 emissions expected under wetter conditions (Lawrence et al. 2015), reducing the global warming potential of the emissions from 25 for CH4 versus 1 for CO2 over a 100-year time period. Additional research is needed to confirm these dynamics at our study sites. It is also important to highlight that these polygon tundra dynamics are observed using high-resolution UAS imagery, but could not be observed using medium- to large-scale observations from AVIRIS-NG and Sentinel-2. This scale

dependency of ecosystem properties emphasizes the necessity of incorporating spatial structure and fine-scale heterogeneity into modeling efforts (Graham et al. 2019; Atkins et al. 2023). However, observing the landscape across different scales not only makes it possible to observe the different drivers but also enables a comprehensive understanding of the dynamics and the impact of climate change and disturbance on these ecological drivers.

Our findings contribute significantly to a better understanding of the landscape dynamics controlling tundra ecosystem processes, with insights into the permafrost carbon feedback. The multiscale analysis here has implications for improved monitoring and could advance our ability to address the complexities of the tundra ecosystem more effectively. The identification of dominant tundra landscape features, coupled with the exploration of the spatial variation of these features, can drive different models for the representation of ALD, key outstanding needs in terrestrial biosphere models (Fisher et al. 2018; Huntzinger et al. 2020).

In summary, pixel size or spatial resolution is a critical factor in determining the level of discretization associated with different spatial observation scales. Although increased spectral resolution can improve model results, the observed spatial variation in the landscape must match the environmental covariates, with matching spatial patterns for above- and below-ground properties. Achieving this congruence between observation and process modeled is essential for accurate model predictions. This extends to the distribution of extreme thaw across the landscape. Emphasizing the strengths of an RS modeling approach while understanding the limitations of the different RS platforms is essential for enhancing current and future monitoring strategies. This knowledge will contribute to our understanding of the impact of climate change on the tundra ecosystem and assessing ecosystem health and resilience will be possible by linking thaw depth frequencies, indicative of disruptions in ecosystem health or decreasing resilience in the face of global warming. Continuous monitoring of these indicators over time could help assess tundra ecosystem stability and resilience in the changing world.

CHAPTER 2

THAWTRENDR: A SPACEBORNE DISTURBANCE HISTORY PRODUCT

Disturbance events and associated ecosystem changes in the Arctic-Boreal Region (ABR) of North America have the potential to unlock a substantial amount of the large soil organic carbon (SOC) stock by thawing and making it available for decomposition. This permafrost carbon feedback (PCF) could significantly influence global-scale climate dynamics and urgently needs an improved representation in state-of-the-art climate models. The current and rapid warming of the ABR is causing increased and intensified disturbance impacts, but quantifying the rate of change across the landscape is challenging, primarily due to a lack of observations. There is a need to develop and test methods for quantifying the detailed landscape aspects of changes in disturbance regimes and thus make it possible to study the post-disturbance thaw and recovery of ABR ecosystems.

In this study, we have generated an annual 30 m spatial resolution disturbance map product through a comprehensive time-series analysis of the historical Landsat satellite record using the LandTrendr algorithm. Our focus was to analyze the disturbance trends for North Alaska, with particular emphasis on the different susceptible thermokarst landscapes. We differentiated between wetland, lake, and hillslope thermokarst landforms to capture the spatial variation in disturbance intensity and trends across these landscapes. To enhance disturbance detection of the LandTrendr algorithm to detect disturbances, we combined model outputs from different spectral indices to create an ensemble of disturbance layers. An RF model used the difference between disturbance datasets as covariates to classify detected disturbances into disturbance classes.

We observed large differences in model outcomes between indices. This underscores the importance of selecting appropriate indices and using a model ensemble to detect disturbances effectively. Interestingly, we found that the highest thermokarst risk classes for lake, hillslope, and wetland are less

affected by wildfires. This suggests that high-risk thermokarst areas are low-risk fire areas, (currently) not prone to fire disturbance that could trigger permafrost thaw and thermokarst disturbances.

Our disturbance dataset enables further investigation into the impact of disturbance history on current vegetation and the effect of disturbance intensity on the landscape, categorized by disturbance type. Quantifying disturbance trends and assessing the associated permafrost vulnerability is crucial for understanding and projecting global carbon cycle dynamics. The potential shift of the ABR from a carbon sink to a carbon source under a future warming climate underscores the urgency and significance of our research, which contributes to understanding the interactions among disturbances, permafrost, and the broader climate system.

2.1. Introduction

The Arctic Boreal Region (ABR) of northwestern North America is characterized by its cold climate and poorly drained soils, which facilitate the extensive accumulation of organic matter in perennially frozen ground or permafrost. Over the past millennia, the ABR has accumulated substantial carbon stocks in its ecosystems. For example, the northern circumpolar permafrost zone stores up to 1,600 Pg C - approximately one-third to one-half of the global terrestrial C storage (Bradshaw and Warkentin 2015; McGuire et al. 2009; Pan et al. 2011). Currently, the ABR is undergoing rapid, widespread, and unprecedented transformation marked by physical and biological changes initiated in recent decades (French 2011, Frost et al. 2018, Jorgenson et al. 2006, Lara et al. 2016, Myers-Smith et al. 2015, Myneni et al 1997). While global climate change is evident, the high northern latitudes have experienced a temperature rise twice that of the global average (AMAP 2017, Chapman and Walsh 2007, Hinzman et al 2005, IPCC 2014, McGuire et al 2006, Serreze and Barry 2011). This accelerated climate warming increases the frequency and intensity of disturbances and associated ecosystem changes in the ABR, potentially unlocking and releasing to the atmosphere a substantial amount of carbon currently stored in the permafrost soils (Tarnocai et al. 2009; Hugelius et al. 2014 & 2020; Hayes et al. 2014). The increased

vulnerability to thaw and decomposition may lead to an increased release of C into the atmosphere (Schädel et al. 2014; Schuur and Abbott 2011; O'Donnell et al. 2012), driving the so-called 'permafrost carbon feedback' (Schuur et al. 2015), thereby further accelerating global warming. In contrast, the potential increase in C uptake by tundra and boreal forest vegetation under similar climate conditions is projected to be smaller than the permafrost C emissions (McGuire et al. 2018; Abbott et al. 2015). For example, considering the current warming trajectory for the ABR, it is estimated that 5% to 15% of the soil organic carbon (SOC) pool could become vulnerable to decomposition and potentially released into the atmosphere by the year 2100. Notably, this projection only considers the gradual thawing of permafrost (Schuur et al. 2015; Hugelius et al. 2014 & 2020), and adding the land area vulnerable to abrupt thaw processes (Olefeldt et al. 2016) is likely to accelerate the release of SOC across the permafrost region (Turetsky et al. 2019 & 2020; Nitzbon et al. 2020).

Press disturbances, like climate warming, cause a gradual yet widespread top-down degradation of permafrost by increasing the active layer thickness (ALT) The resulting increased rooting depth and decomposition rate will release nutrients thereby slowly altering the environmental conditions and the associated vegetation communities (Salmon et al. 2016; Blume-Werry et al. 2019; Wang et al. 2017). In contrast, thermokarst is categorized as a pulse disturbance, where the thawing of ice-rich permafrost leads to rapid and significant subsidence of a part of the landscape, resulting in pronounced shifts in hydrological patterns (Turetsky et al. 2019; in 't Zandt, Liebner, and Welte 2020; Schuur et al. 2015; Osterkamp et al. 2009). Pulse disturbances have the potential to push an ecosystem beyond its resilience thresholds, making recovery to the previous state unlikely, and triggering ecosystem changes (Grosse et al. 2011; Scheffer et al. 2001 & 2009). These ecosystem changes could be catastrophic and result in a substantial release of large amounts of C (Turetsky et al. 2019 & 2020). Other disturbances linked to global warming are causing more extreme weather events (e.g., heat waves, rain storms, drought, pests) and increased fire frequency and intensity of wildfires.

Arctic tundra and boreal forests are particularly sensitive to climate variability, and the exhibition of an amplified response to external disturbances can indicate the ecosystem's proximity to a critical threshold or transition (Seddon et al. 2016; Scheffer et al. 2009). Warming is pushing landscapes over their tipping point and accelerating disturbance regimes, for example, the larger area covered by higher-intensity fires as shown by Rocha et al. (2012). The interplay of these events could eventually shift the trajectory of ABR ecosystems by triggering permafrost thaw and vegetation changes (Walker et al. 2019; Genet et al. 2013; Li et al. 2021).

A profound understanding of these disturbance dynamics is key to accurately predicting the magnitude - and even direction - of the carbon-climate feedback in the future. To determine the future trajectory of the ABR, we need to address the extent of the permafrost in the region that is currently resilient to transition or vulnerable to near-term thaw induced by climate change. Our approach involves a comprehensive analysis of the Landsat satellite record for trends in disturbances over the recent decades. By characterizing landscape resilience from these observed patterns, we aim to map the vulnerability of permafrost in the upcoming decades. Observing permafrost disturbance in the ABR is challenging due to the spatiotemporal variability and complex interactions between vegetation cover and permafrost (McGuire et al. 2002), compounded by the variable ground ice content, creating a large heterogeneity across landscapes and regions. We build on the decades-long Landsat archive available on Google Earth Engine (GEE) (Gorelick et al. 2017; Kennedy et al. 2018) and by integrating disturbance-targeted observations, we aim to unravel the resilience of permafrost landscapes. Thaw features can be observed by satellites (INitze et al. 2018; Beamish et al. 2020), but by mining the entire Landsat archive to find and characterize disturbance events we can quantify the different aspects of disturbances across the ABR. The outcomes of our study make it possible to study post-disturbance thaw and recovery by creating a spaceborne disturbance product for the permafrost region of the Seward Peninsula, Alaska.

2.2. Methods

2.2.1. Spaceborne Disturbance Detection

As a case study for the circumpolar Arctic region our analysis covers the North of the state of Alaska, including the Seward Peninsula, which hosts the Next-Generation Ecosystem Experiments Arctic (NGEE-Arctic) project (https://ngee-arctic.ornl.gov/) collecting high-resolution datasets (Yang et al. 2021, 2023) and the ABOVE (https://above.nasa.gov/) AVIRIS-NG fight campaign (Miller et al. 2018) allowing for future data integration.

The effects of climate change are pushing landscapes over their tipping point and accelerating disturbance regimes with a significant effect on the ABR. To map and monitor these changes, remote sensing techniques have emerged as a crucial tool with a proven track record. Pulse disturbances have been mapped and described using remote sensing (Jones et al. 2011), and long-term RS records have facilitated the study of trends in vegetation properties associated with press disturbances (Beck and Goetz 2011). Recent studies have successfully demonstrated the approach for detecting and classifying various ABR landscape changes (Olthof and Fraser 2014; I. Nitze et al. 2018; Ingmar Nitze et al. 2017, 2021). Advances in access to satellite imagery, e.g. free access to the Landsat archive since 2008, combined with a massive increase in the availability of cloud-based storage and processing, have created novel opportunities for image processing and change detection. For example, the combined integration of the Landsat archive and time-series segmentation algorithms like LandTrendr (Landsat-based detection of Trends in Disturbance and Recovery) (Kennedy, Yang, and Cohen 2010) and CCDC (Continuous Change Detection and Classification) (Zhu and Woodcock 2014) are now available and implemented on Google Earth Engine (GEE) (Kennedy et al. 2018; Gorelick et al. 2017; Arévalo et al. 2020).

The disturbances detected depend on the algorithm, spectral index, and the point density of the time series observations (Pasquarella et al. 2022). Each segmentation algorithm has specific input

requirements, for example, CCDC captures and models the phenological variation and deviation over time and is effective in regions with long growing seasons and/or strong phenological variation. The unique challenges of the ABR such as the short growing season, influence of residual snow, and frequent cloud cover limit the ability of these phenological-driven approaches. The LandTrendr change detection and segmentation method is based on a yearly composite (Kennedy, Yang, and Cohen 2010), and the integration of LandTrendr with GEE has been demonstrated for specific ABR disturbances by detecting retrogressive thaw slumps (Runge, Nitze, and Grosse 2022). Next to arctic-specific factors, like the short growing season, using the Landsat archive over Alaska adds complexity to creating pixel-based time series. First, there is limited data coverage over Alaska within the Landsat archive from 1984 to 2005 (Ju and Masek 2016) due to data relay issues in combination with limited tasking and Landsat-7 was affected by the scan line corrector failure since 2003 (Goward et al. 2006).

To address these challenges, our approach leverages the extensive processing and storage capabilities of GEE to implement the LandTrendr algorithm across a range of spectral indices calculated from the Landsat archive (Table 1). The time series data were extracted from maximum pixel values collected during the peak summer season, spanning from July 5 to August 25, corresponding with peak vegetation. This process creates an ensemble of yearly observations from 1986. Disturbances in the ABR occur at different scales and are driven by various processes, triggering different disturbance trajectories. We leverage this variability by using different band indices, relating to different processes, as input for LandTrendr, creating an ensemble of disturbance patterns in the results. Using an ensemble of different metrics has improved disturbance detection performance (Cohen et al. 2018; Hislop et al. 2019; Healey et al. 2018). This allows for the creation of an ensemble of disturbance maps from 1986 to 2020, including the disturbance's year, intensity, recovery, and duration. The ensemble will facilitate the study of trends of disturbances over a large region.

Table 2.1: Landsat-based indices used for disturbance detection. The Tasseled Cap indices are Brightness (TCB), Greenness (TCG), Wetness (TCW), and Angle (TCA).

Indices	Calculation (Landsat)
NDVI	(NIR − Red) / (NIR + Red)
NDWI	(Green - NIR) / (Green + NIR)
NBR	(NIR − SWIR2) / (NIR + SWIR2)
TCB	0.2043 ∗ Blue + 0.4158 ∗ Green + 0.5524 ∗ Red + 0.5741 ∗ NIR + 0.3124 ∗ SWIR1 + 0.2303 ∗ SWIR2
TCG	− 0.1603 ∗ Blue + − 0.2819 ∗ Green + − 0.4934 ∗ Red + 0.7940 ∗ NIR + − 0.0002 ∗ SWIR1 + − 0.1446 ∗ SWIR2
TCW	0.0315 ∗ Blue + 0.2021 ∗ Green + 0.3102 ∗ Red + 0.1594 ∗ NIR + − 0.6806 ∗ SWIR1 + − 0.6109 ∗ SWIR2
TCA	Arctan (TCG/TCB)

2.2.2. Spatial and Temporal Disturbance Patterns

The spatiotemporal disturbance patterns are analyzed based on landscape characteristics and synthesized within the thermokarst vulnerability zones as delineated by Olefeldt et al. (2016). Initially established to asses thermokarst risk in lake, wetland, and hillslope environments, these zones serve here as a framework for characterizing the landscape based on: (a) Permafrost distribution and ground ice content: The ice content of the permafrost drives vegetation changes, for example, abrupt thaw drives a change from woody vegetation to graminoid cover in ice-rich lowlands, whereas in ice-poor uplands the woody vegetation increases, see Heijmans et al. (2022) for a detailed review; (b)Topography; (c) Sedimentary overburden; and (d) Histel coverage. We expect these zonation to be valuable for analyzing not only thermokarst trends, but also the patterns of wildfire, and other disturbances. The original classification by Olefeldt et al. (2016) includes three classes based on lake, wetland, and hillslope thermokarst types, each subdivided into low, moderate, high, and very high categories of vulnerability. This allows the creation of an ensemble of disturbance trends over time by thermokarst class. To compare the rate of change by disturbance class, simple linear models with a fixed intercept (we start with the

hypothetical detected disturbance = 0) were fitted on the cumulative yearly observed disturbance. Disturbance vulnerability class was added as an interaction term to compare intercept differences. For this we used least-square means, to obtain the slopes for each risk intensity class. All analyses were performed in RStudio (R version 4.3.2, using the packages nlme and ARest).

2.2.3. Disturbance Classification

The disturbance history allows tracking changes over time and showing the temporal evolution of the disturbance probability. Here, we also aim to characterize the disturbance type. To classify the disturbance dataset, we developed a classification based on the key indices identified for disturbance detection. The LandTrendr output for each selected indices, excluding the year of disturbance, is used as a covariate in a disturbance-type classification model. The year of disturbance is attached to the classified disturbance dataset, creating a yearly, classified spatial disturbance layer from 1986 to 2020, allowing for a spatiotemporal trend analysis by disturbance type. To address the limited field observations due to the demanding conditions to collect additional field data in the ABR, we synthesize existing datasets e.g. (Swanson 2021; I. Nitze et al. 2018; Pekel et al. 2016; Hansen et al. 2013). Disturbance classes are averaged into broader categories and training data is extracted using equal sampling across classes in GEE. We use a 70/30 split for training and validation datasets. Among the two GEE classifiers, ee.Classifier.smileCart() and ee.Classifier.smileRandomForest(), RandomForest allows better tuning of the classes by using the class probability output and was used for the final classification.

2.3. Results

2.3.1. Disturbance Detection

The detection of pulse disturbances using various indices with the LandTrendr algorithm resulted in different trajectories and detection probabilities (Figure 2.1). These variations and differences among indices facilitated the creation of an ensemble dataset that integrates the diverse disturbance trends detected by each index.

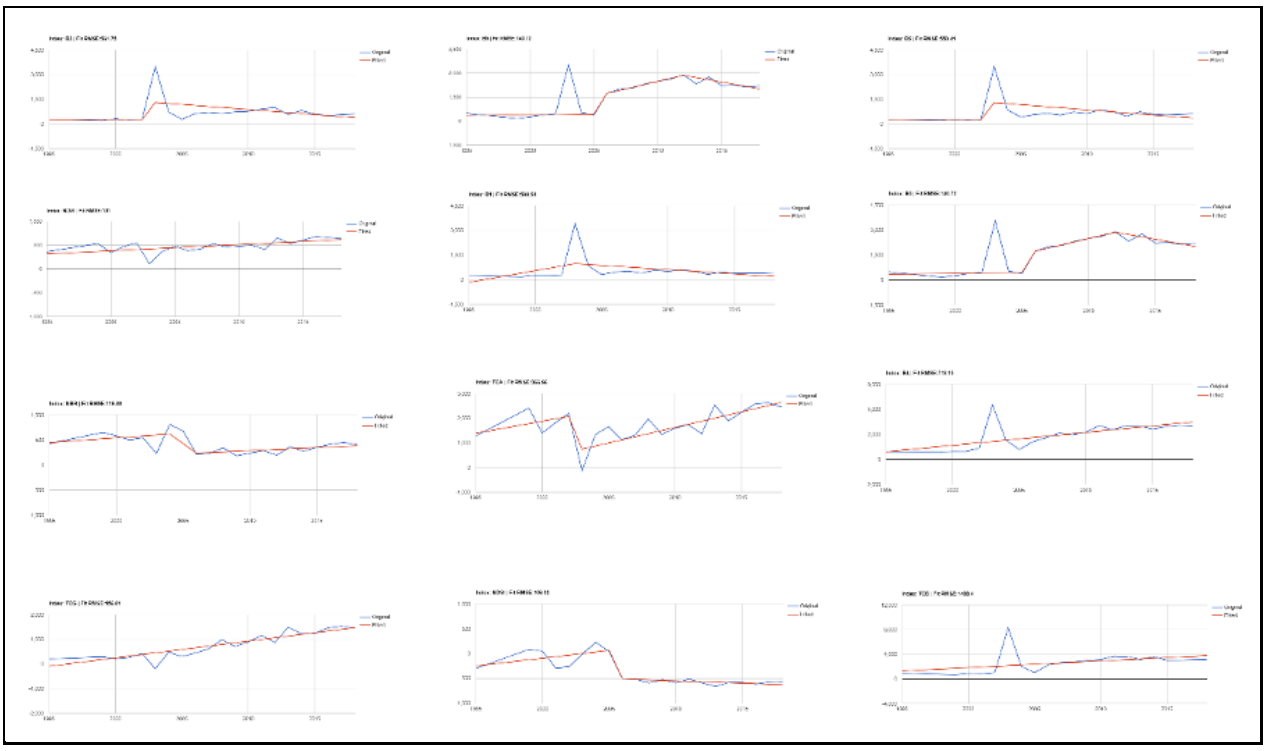

Figure 2.1. Differences in disturbance detection by LandTrender based on the used Landsat derived indices.

There is a large variation in the detected disturbed area depending on the index applied by LandTrendr. Figure 2.2 summarizes the disturbance layers from the different indices over northern Alaska from 1986 to 2020, revealing that on average 1.15% (sd 1.26) of northern Alaska was disturbed. The disturbance percentages observed by the different indices range from 0.00% up to 3.82%, with a median of 0.85% slightly lower than the mean. Comparing the influence of the indices used in the LandTrendr model, the most disturbed areas were detected by TCA lag (3.5%), NBR lag (2.6%), TCG lag (2.3%), TCW lag (1.1%), TCA gain (1.2%), and TCG gain (1.1%).

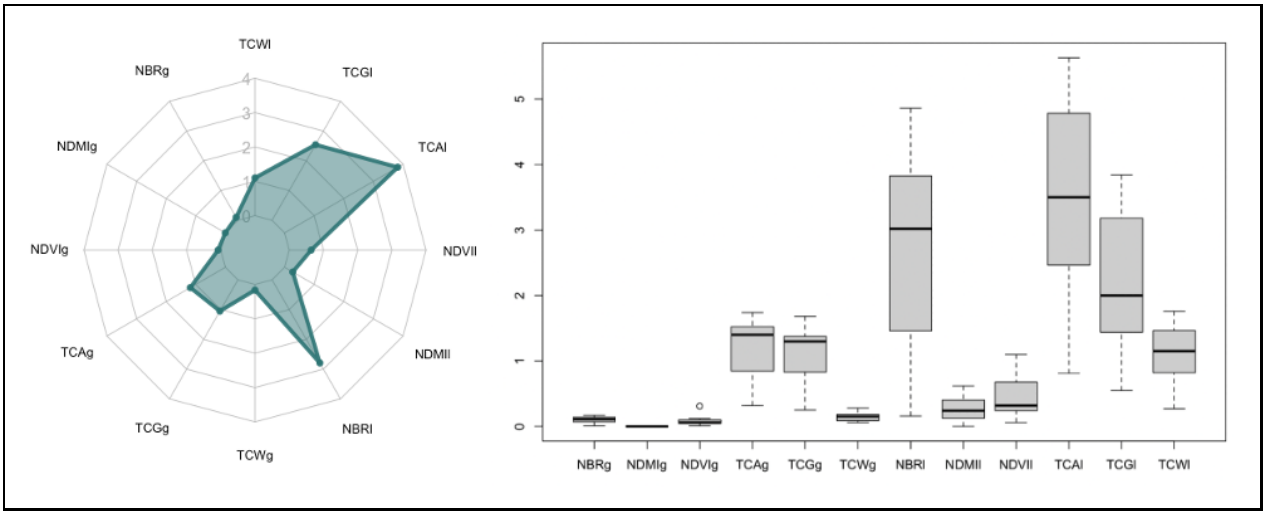

Figure 2.2. Spider chart represents the percentage of north Alaska affected by disturbances detected by LandTrendr for the different indices, from 1986 till 2020. The boxplot on the right shows the variation around the median.

2.3.2. Spatial Disturbance Patterns

Furthermore, the observed differences between indices can be specific to certain disturbance classes. Figure 3 summarizes the disturbance layers over northern Alaska from 1986 to 2020, categorized by thermokarst risk type and risk gradation. The detection patterns observed are similar to those of the averaged disturbance ensemble, with higher disturbance percentages registered for NBR and the three TC indices.

Within the thermokarst category, the average disturbance values are similar:

- Hillslope thermokarst zones: 1.2%,
- Wetland thermokarst zones: 1.1%,
- Lake thermokarst zones: 0.9%.

Statistically, no significant differences were observed using a one-way ANOVA test ($p = 0.61 > 0.05$) to test for differences between the group averages. However, larger differences were observed when averaged by risk category:

- Low-risk categories: 1.6%,

- Moderate risk: 1.1%,
- High risk: 0.9%,
- Very high risk: 0.6%.

A one-way ANOVA test ($p = 0.036 < 0.05$) followed by Tukey's Honest Significant Difference (HSD) method was used to detect differences between group means. A significant difference was observed between the very high-risk and low risk thermokarst groups (p adj $0.03 < 0.05$).

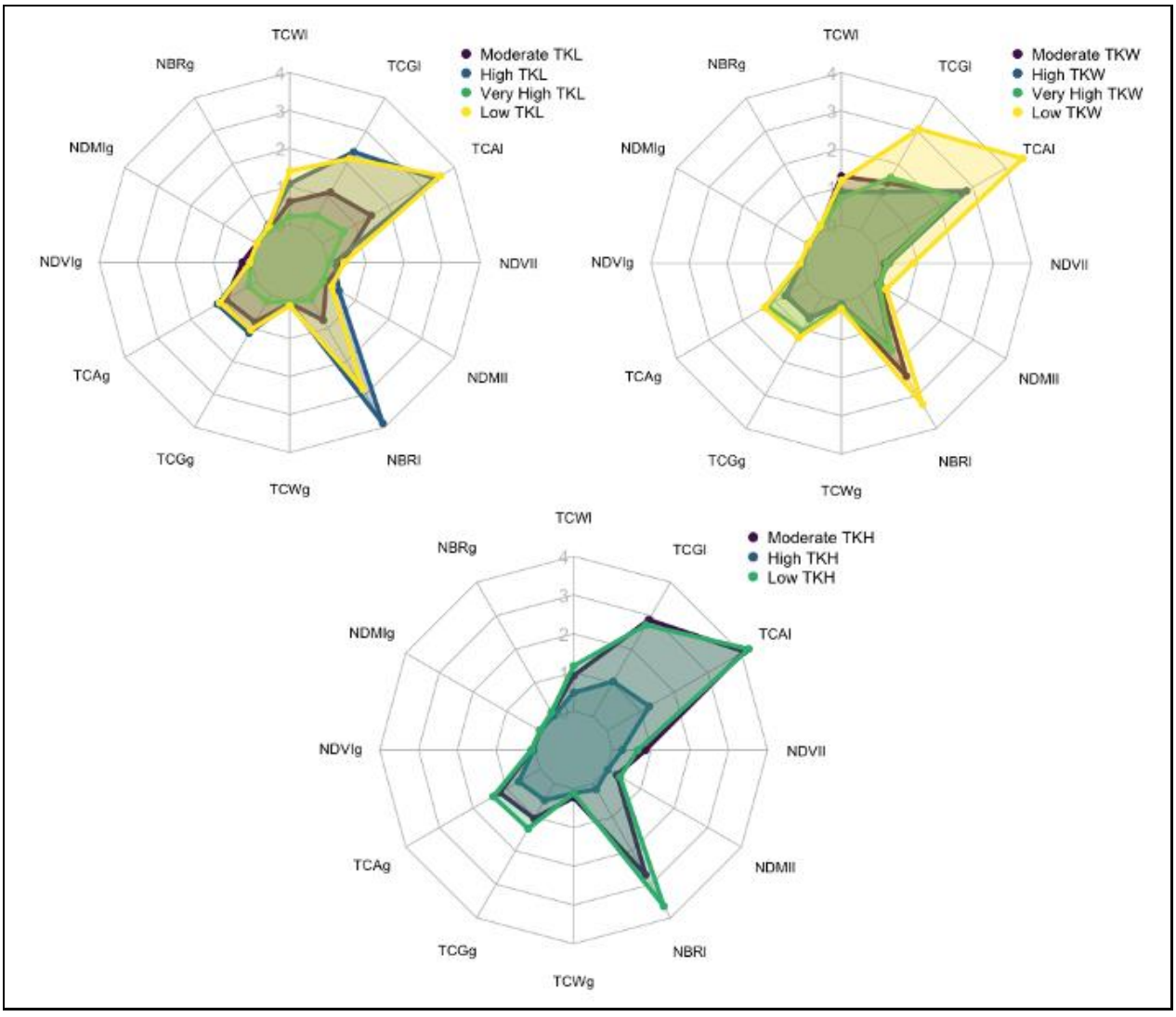

Figure 2.3. Spider charts showing the disturbance rate by thermokarst risk and indices used, from 1990 till 2023, and summarized by thermokarst risk area: A. Thermokarst lake, B. Thermokarst wetland, and C. Thermokarst hillslope.

Comparing the thaw risk for each thermokarst type, significant differences between the mean thaw risks were observed only for the lake thermokarst risk zone ($p = 0.039 < 0.05$) using one-sided ANOVA. However, these differences were not significantly confirmed by Tukey's HSD test.

Examining the different risk zones, it was found that the very high and moderate high lake, high hillslope, and very high, high, and moderate wetland thermokarst risk zones correlate with relatively low disturbance percentages. Conversely, the low-risk zones exhibit the highest disturbance percentage for lake, wetland, and hillslope thermokarst.

Specifically, low-risk thermokarst zones show high observed disturbance percentages as detected by NBR and TCA indices. In contrast, high-risk thermokarst zones display low disturbance percentages on the NBR and TCA disturbance indices and relatively high on the other tasseled cap disturbance indices. This pattern indicates a relationship between the importance of the index and the expected disturbance for Lake, Wetland, and hillslope disturbance types.

2.3.3. Spatio-Temporal Patterns of Disturbance

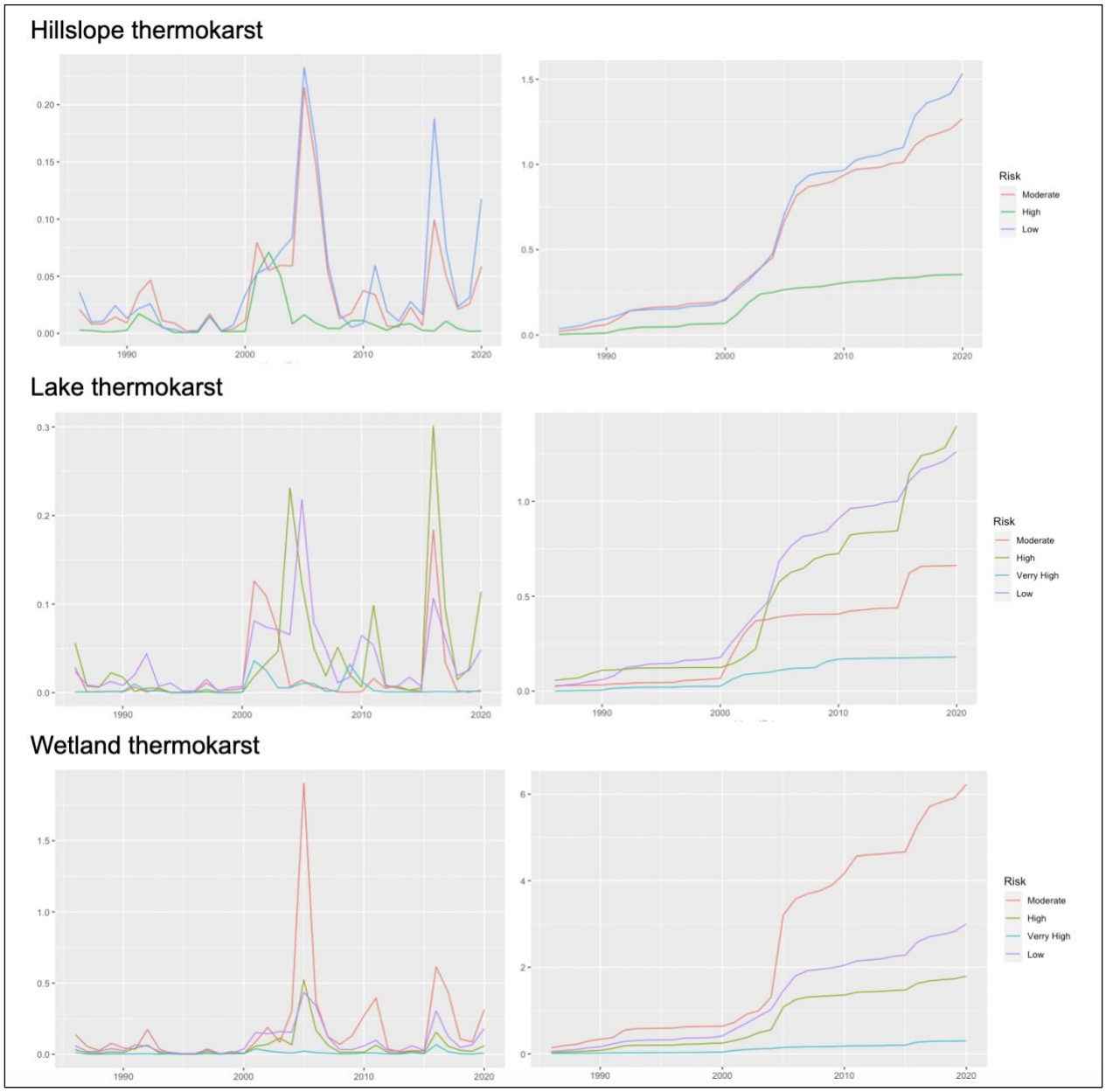

Figure 2.4. Spatio-temporal disturbance patterns were analyzed for the hillslope, lake, and thermokarst risk polygons. The analysis includes the yearly disturbed area and the cumulative increase in disturbed area over time from 1986 to 2020. The disturbance patterns were examined for moderate-, high-, and low-risk thermokarst hillslope zones, as well as for moderate-, high-, very high-, and low-risk zones for lake and wetland thermokarst.

Figure 2.4 illustrates the occurrence of peak disturbances, notably clustered around the years 2005 and 2016. There is no observed shift in disturbance between thermokarst categories; however, there is an

intensity peak specifically for wetland thermokarst disturbance. The accumulated disturbances over time, observed in Figure 2.4, exhibit a distinct pattern across different thermokarst and risk classes. Disturbance accumulation remained stable until a steep increase was observed during the years 2000 - 2005. These peak disturbances account for the initial steep rise, yet an upward trend in disturbances continued even after this period. Large peak disturbances correlate with a steeper increase in the overall disturbance trend, indicating significant impact evens followed by sustained disturbance activity.

Table 2.2: Testing slope coefficients of accumulated disturbance trends.

	Lake	Wetland	Hillslope
Low - Moderate	$p < 0.01$	$p < 0.01$	
Low - High		$p < 0.01$	$p < 0.01$
Low - Very high	$p < 0.01$	$p < 0.01$	/
Moderate - High	$p < 0.01$	$p < 0.01$	$p < 0.01$
Moderate - Very high	$p < 0.01$	$p < 0.01$	/

2.3.4. Disturbance Trends By Class

Based on the observed differences between indices (Figure 2.1) disturbance datasets were used as covariates in an RF model to classify detected disturbances into specific disturbance classes. First, we identified the key indices (Figure 2.3) for further disturbance detection: TCW l&g, TCG l&g, TCA l&g, and NDVIl & NBRl. Training data was split 70/30 for training and validation. The overall validation (Table 2.3) accuracy was 86% for the fire class, 63% for drained lakes, and 67% for wetlands. Figure 2.5 provides a detailed depiction of detected drained lakes on the Seward peninsula. Additionally, we included two Non-Disturbance (ND) classes in the classification to account for false positive disturbance detections related to water bodies.

Table 2.3: Confusion matrix based on independent validation data.

%	Fire	Drained	ND1	Wetland	ND2	
Fire	**87.7**	5.3	3.5	0.0	3.5	**87.7**
Drained	1.6	**63.9**	16.4	4.9	13.1	**63.9**
ND1	3.3	15.0	**36.7**	30.0	15.0	**36.7**
Wetland	1.6	6.6	13.1	**75.4**	3.3	**75.4**
ND2	6.0	10.4	16.4	3.0	**64.2**	**64.2**
	86.2	**62.9**	**41.5**	**66.7**	**67.2**	**65.4**

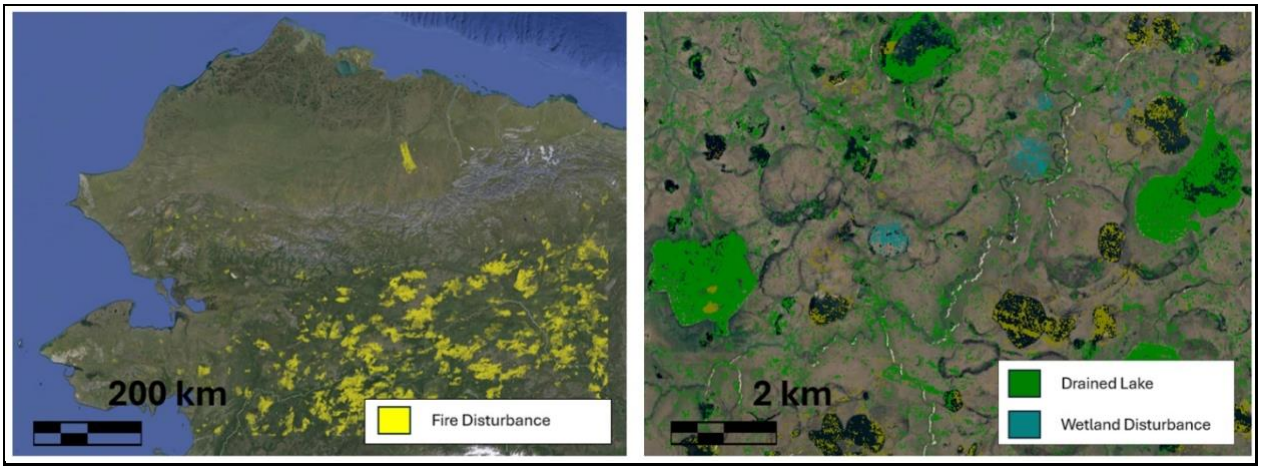

Figure 2.5. Detailed representation of the disturbance dataset, focusing on fire disturbances (yellow) and drained lakes (green).

In the final step, we assign the classified disturbance layer with the year of disturbance from the original LandTrendr output. Figure 2.6 illustrates the total accumulated disturbed area categorized by fire, drained lakes, and wetlands disturbance for thermokarst hillslope, wetland, and lake thermokarst risk polygons. Fire disturbance accounts for the largest proportion of the disturbed area. In contrast, lake and wetland disturbances are significantly smaller in scale (Figure 2.6 - right column), and exhibit distinct disturbance patterns, compared to fire disturbances, with peak occurrences around 1992 and after

2000. This pattern was not previously detected, as fire disturbances dominate the overall observed disturbance pattern over time (Figure 2.4).

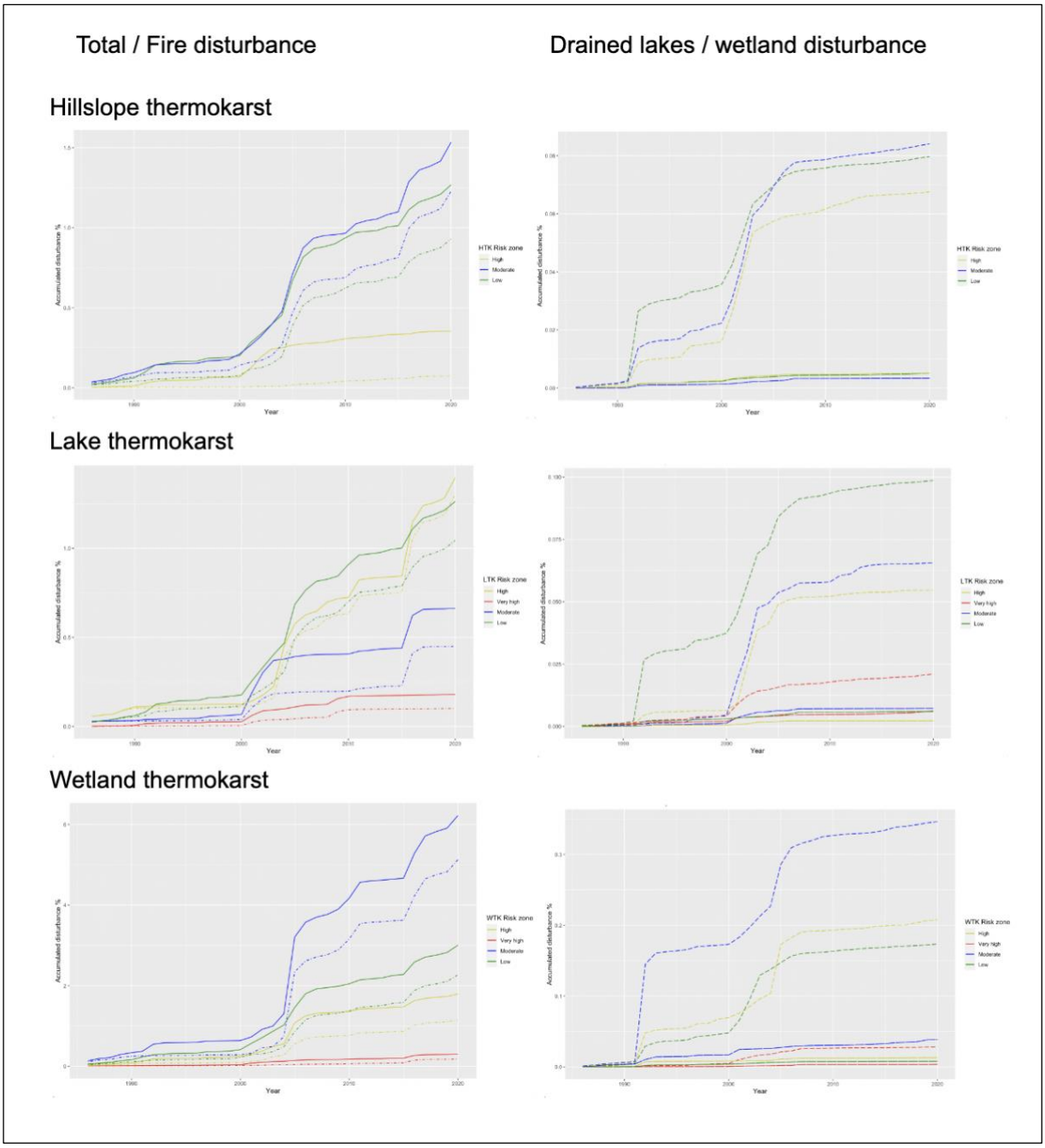

Figure 2.6: Spatio-temporal disturbance patterns categorized by disturbance type for the hillslope, lake, and thermokarst risk polygons. The analysis includes the cumulative increase in disturbed area over time, spanning from 1986 to 2020, for fire, drained lakes, and wetland disturbance. The disturbance patterns were examined across risk zones: very high-, high-, moderate- and low-risk thermokarst classes wetland, lake, and hillslope thermokarst.

2.4. Discussion and Conclusion

We tailored the LandTrendr algorithm to address the specific disturbances observed in the ABR, which are diverse and highly variable, each triggering different spectral responses. Traditionally, the LandTrendr algorithm runs on a single vegetation or spectral index. By comparing the outcomes of LandTrendr across different spectral or vegetation indices, we observed large differences in disturbance detention. This variability has also been noted in forested areas (Cohen et al. 2018), highlighting the importance of an ensemble approach.

To enhance disturbance detection, we combined model outputs from different spectral indices to create an ensemble of disturbance layers. This enabled us to map yearly disturbances from 1986 to 2020. Combining ensemble layers offers several benefits, including increased robustness and accuracy by leveraging the strengths of multiple models. Various post-processing techniques have been proposed, primarily for forest disturbance detection. For instance, (Healey et al. 2018) used a stacked generalization approach based on multiple detection algorithms using RF, incorporating pre-and post-disturbance data. Adding various pre-and post-disturbance indices as covariates to our RF model could be beneficial and potentially lead to improved detection accuracy.

To identify differences in disturbance pressure between landscapes with varying characteristics, we differentiated between risk classes associated with wetland, lake, and hillslope thermokarst landforms as defined by (Olefeldt et al. 2016). Our analysis revealed spatial variation in disturbance intensity and trends across these landscapes, indicating specific disturbance patterns for different thermokarst landscapes. High-risk thermokarst zones across all classes (lake, hillslope, and wetland) exhibited the lowest observed disturbance pressure. This raised the question: Are disturbances in these areas either not detected or the 'expected' disturbances have not yet been activated? Time segmentation disturbance algorithms, like LandTrendr, are developed for detecting pulse disturbances, while thermokarst disturbances can be initiated as a press disturbance before triggering a pulse disturbance

that can be observed by the algorithms. Fire disturbance, on the other hand, proportionally affects the largest areas among the observed disturbances, with its increasing prevalence being particularly significant. Fires impact the tundra landscape by combusting biomass and organic matter from tundra and forest vegetation and soils, contributing to a globally significant source of greenhouse gas emissions (Mack et al. 2013; Van Der Werf et al., 2017), also there is an increasing risk to trigger permafrost thaw and thermokarst post-fire. Increases in thaw lakes, peatland, and wetland areas are major contributors to methane (CH4) emissions due to their extensive organic-rich soils commonly found in arctic tundra and boreal forest ecosystems (McGuire et al. 2009; Roulet et al. 1992; Peng et al. 2022). The observed rise in disturbance-driven carbon emissions could potentially weaken the ABR land sink. However, the highest thermokarst risk classes for lake, hillslope, and wetland are less affected by wildfires. This suggests that high-risk thermokarst areas are low-risk fire areas, (currently) not prone to fire disturbance that could trigger permafrost thaw and thermokarst disturbances.

To calculate the disturbance probability and track changes over time, we analyzed the temporal evolution of disturbance probability. Additionally, it is crucial to predict future disturbance trends based on the time since the last disturbance, the resilience of the landscape, and the current ecosystem state. Our dataset presents the opportunity to further investigate the impact of disturbance history on vegetation and assess the effect of repeated fires and their intensity on the landscape. Both, post-disturbed thaw and post-thaw recovery can be categorized.

Arctic tundra and boreal forests are particularly sensitive to climate variability, and their amplified response to external disturbances may indicate the ecosystem's proximity to a critical threshold or transition (Seddon et al. 2016; Scheffer et al. 2009). We provide the framework and first dataset to study and understand these dynamics, essential for predicting future disturbance trends and their impacts on the carbon balance of these vulnerable ecosystems and help to demystify the permafrost carbon feedback, which urgently needs a better representation (McGuire et al. 2018).

CHAPTER 3

BELOW-GROUND PERMAFROST PROCESSES MANIFEST AS ABOVE_GROUND FUNCTIONAL TRAITS IN ARCTIC TUNDRA LANDSCAPES

Tundra climate change exerts significant pressure on Arctic ecosystems impacting their resilience to disturbances and shifts in ecosystem structure. Detecting changes in tundra ecosystems is challenging due to the heterogeneous nature of the landscape, permafrost, and vegetation patterns. While remote sensing observations capture primarily above-ground properties, below-ground properties are critical in the Arctic, so much of our understanding is dependent on how aboveground vegetation properties thereby reflect the state of the underlying permafrost. Here we propose a novel approach using hyperspectral imagery to map the spatial patterns of tundra functioning. We hypothesize that by combining spectral metrics and traits linked to tundra functioning, a clustered functional diversity assessment will reveal the spatial patterns of tundra functioning from which we may gain insight into the state of the underlying permafrost and the stability of the tundra ecosystem.

Using hyperspectral AVIRIS-NG imagery from NASA's ABoVE (Arctic-Boreal Vulnerability Experiment) field campaign and field-based thaw depth measurements we identified spectral plant traits indicative of the functioning of the tundra ecosystem. The balanced set of spectral traits was clustered to create 'thaw functional types' and compared with thaw depth measurements and model outcomes to unravel the interactions between tundra functioning and the state of the permafrost. We show that a balanced set of spectral vegetation traits can be used to create high-resolution maps showing regional patterns in trait diversity, without prior taxonomic info, indicative of tundra functioning.

3.1. Introduction

The Arctic has experienced warming at a rate two to four times faster than any other biome on Earth (Rantanen et al. 2022). The pronounced warming of the Arctic region, known as Arctic amplification, is considered the primary driver of recent changes in tundra ecosystems. Over thousands of years, the low soil temperatures and limited drainage of permafrost soils have facilitated the accumulation of dead organic matter, leading to the sequestration of substantial carbon reserves, nearly double the size of the atmospheric C pool (Schuur et al. 2015; Hugelius et al. 2014; McGuire et al. 2012). However, the current climate warming trends and consequently thawing permafrost can release vast amounts of the C previously stored in the permafrost by making it available for decomposition and releasing greenhouse gasses such as carbon dioxide and methane into the atmosphere (Schuur et al. 2015; Hayes et al. 2014). The permafrost carbon feedback mechanism is one of the largest terrestrial-climate feedbacks with a strong positive effect on global warming (Schuur et al. 2008, 2015; Schaefer et al. 2014). Permafrost thaw can alter the resilience of the tundra ecosystem and increase the vulnerability of the permafrost landscape to abrupt (pulse) disturbances that can have a huge impact on the soil C stocks (Schuur and Abbott 2011; Grosse et al. 2011; Jones et al. 2015; Holloway et al. 2020; Treat et al. 2024). The effects of permafrost thaw are currently underestimated due to the challenge of detecting gradual permafrost thaw (Jorgenson and Grosse 2016; Bartsch, Strozzi, and Nitze 2023), the tendency to generalize the tundra landscape characterization in region-wide assessments (Lara et al. 2020), and the limited or missing representation of the permafrost C feedback in current climate models (Schädel et al. 2024; Fisher et al. 2018).

Permafrost thaw increases the depth of the seasonal unfrozen layer on top of the permafrost, or active layer. It drives changes like increased mineralization, nutrient cycling, and rooting depth reflected in the tundra vegetation community structure and composition traits (Standen and Baltzer 2021). Plant functional traits are linked with geomorphological processes in tundra landscapes, and disturbances

drive changes in trait composition and diversity (Kemppinen et al. 2022; Bjorkman et al. 2018). To study the adaptive strategies of tundra vegetation, it is important to focus on functional traits. The significance of functional traits lies in their direct or indirect impact on the fitness and performance of the individual plant species within a given tundra landscape (Violle et al. 2007). Morphological, physiological, or phenological characteristics or traits are considered functional traits if they influence growth rate, reproduction, and survival (Díaz and Cabido 2001; Violle et al. 2007). Functional traits serve as vital indicators of species distribution and individual performance across environmental and disturbance gradients. Assessing leaf and plant functional traits provides insight into the ecosystem functioning and resilience, and is consequently indicative of the ecosystem response to disturbances (Funk et al. 2017; Reich, Wright, and Cavender-Bares 2003; Lavorel and Garnier 2002; Wright et al. 2004). Understanding the relationship between functional traits, trait diversity, and the environment allows for forecasting the effects of climate change (Myers-Smith, Thomas, and Bjorkman 2019; Thomas et al. 2020). A Functional Diversity assessment can link the changes in biological diversity and the underlying ecosystem processes by combining traits that influence individual fitness and ecosystem functioning (Violle et al. 2007, 2014; Asner et al. 2017).

Field measurements of arctic plant traits are challenging, due to the remote location, short growing season, and the spatial heterogeneity in tundra vegetation. Remote Sensing (RS) offers a key advantage by enabling continuous spatiotemporal observations of arctic environments. Recent advances in imaging spectroscopy have revolutionized our ability to observe spectral leaf and canopy traits, facilitating continuous, spatiotemporal observations and diversity metrics across landscapes (Nelson et al. 2022; Jetz et al. 2016; Yang et al. 2023). Spectral traits are linked to leaf pigments (eg. chlorophyll), leaf foliar chemistry (eg. nitrogen or phosphorus content), structural (eg. LAI), or senescent (dry) carbon (cellulose and lignin index) properties of the reflected vegetation and can be linked to belowground processes, via decomposition, nutrient cycling, and soil microbial community composition (Madritch et

al. 2020; de Vries et al. 2012). Spectral traits can be derived from hyperspectral imagery, and using NASA's airborne imaging spectrometer AVIRIS-NG enables the spatial mapping of canopy and plant functional traits (Angela Lausch et al. 2016). These canopy traits reflect the heterogeneity across the landscape (Asner et al. 2014), providing detailed insights into spatial patterns of tundra functioning. Creating a spatial representation of the functional heterogeneity of the tundra landscape requires selecting a balanced set of spectral traits encompassing the characteristics and adaptations of tundra vegetation to varying environmental conditions and disturbances. Using spectral plant traits beyond field-measured plant traits can offer a more comprehensive understanding of ecological patterns and ecosystem functions by quantifying similarities, differences, and distribution of the spectral traits (Cadotte, Carscadden, and Mirotchnick 2011). RS indicators of functional diversity enable the detection and monitoring of spatial trends and patterns in vegetation health (Angela Lausch et al. 2016), facilitating the derivation of ecosystem functioning, health, and resilience (to change) without individual species mapping. A spatially explicit assessment of functional diversity in tundra vegetation can reveal spatial patterns in tundra functioning linked to ecosystem stability and resilience (A. Lausch et al. 2016; Schneider et al. 2017). Recent studies such as Kemppinen et al. (2022) have demonstrated the relationships between plant (community) functional traits and geomorphological processes in tundra landscapes. Moreover, Mason et al. (2005) advocate for using a combination of functional richness, functional evenness, and functional divergence as essential components to assess functional trait diversity.

To understand the vegetation response to environmental changes, Díaz et al. (2016) identified the key plant traits for growth, survival, and reproduction. They showed that the first two principal axes explained most of the trait variation and the axes were identified as (a) plant and leaf size, comprising attributes like plant height and leaf area, and (b) the leaf economic trait axis, summarizing photosynthetic leaf area construction costs, including leaf nutrient and pigment contents, as well as

specific leaf area. Although the global trait relationship along these two axes also applies to the tundra biome, Thomas et al. (2020) found a reversed relative importance of these axes suggesting the primary importance of resource economic traits such as resource allocation and utilization. However, despite the emphasis on resource traits, we should not overlook the importance of size traits, as tundra warming is expected to benefit larger plants and leaves, and these size-related traits will inform the trajectory of the tundra in a warming world (Thomas et al. 2020; Myers-Smith, Thomas, and Bjorkman 2019). Translating these findings to the tundra landscape, changes along axis (a) may affect carbon storage, snow trapping, and shading, while axis (b) relates to nutrient cycling and availability, photosynthetic efficiency, and resilience. Therefore, the selected spectral traits should also reflect the potential of vegetation to withstand or adapt to disturbances associated with a warming landscape. These traits must be ecologically meaningful to depict the response of tundra vegetation to changing environmental conditions.

In this chapter, we utilized AVIRIS-NG hyperspectral imagery acquired by NASA's ABoVE (Arctic-Boreal Vulnerability Experiment) flight campaign (Miller et al. 2018), to calculate spectral vegetation traits for a study area in western Alaska, USA. Different spectral traits were combined to detect subtle changes in vegetation characteristics that could indicate variability in the active layer, hydrology, or nutrient availability - parameters that are particularly susceptible to changes under current climate scenarios. Clustering key spectral traits into the so-called thaw functional type classes creates a high-resolution spatial data set of trait-based above-ground tundra characteristics that indicate the state of below-ground properties, such as permafrost. The spatial variability in functional diversity will represent the permafrost-vegetation interactions due to the strong coupling between vegetation and permafrost features in the tundra landscape. Further analysis of traits, trait diversity, and trait relationships can be used to derive vegetation trajectories to thaw. The functional diversity will show the spatial variation in

thaw-related functional traits, without prior knowledge, resembling the resilience of permafrost to future warming.

3.2. Materials and Methods

3.2.1. In-situ Thaw Depth Measurements for Spatial ALD Modeling

Our study focused on a site near Nome on the Seward Peninsula, Alaska. The Seward Peninsula, located in western Alaska below the Arctic Circle, is covered by tundra vegetation underlain with discontinuous permafrost (Peel, Finlayson, and McMahon 2007). The site at Teller Road mile 27, hereafter called Teller, is characterized by coastal tundra featuring transitions from wet meadow tundra to willow shrubland along the streams, as well as erect dwarf shrub tundra, sedge willow dryas, and shrub and sedge tussock tundra (Raynolds et al. 2019). Through collaborations with the Next-Generation Ecosystem Experiments Arctic (NGEE-Arctic) (https://ngee-arctic.ornl.gov/), field-based thaw depth measurements were collected across the Teller site. The spatial sampling strategy was designed to capture the spatial variability of tundra vegetation, permafrost features, and disturbances by linear transects perpendicular to the elevation gradient. Thaw depth was measured along the transects using a thaw probe (130 cm long, 1 cm diameter, marked with 5-centimeter increments). We pushed it into the ground until resistance of the permafrost layer was encountered, and recorded the depth. At sample locations with rocks or a high variability, multiple thaw depths were sampled within an area of about 2 by 2 m square, where we reported the maximum thaw depth. The active layer depth (ALD, n = 419) was measured across six transects, avoiding alignment with vegetation and environmental gradients, spanning distances from 2.5 to 3 km, totaling over 16 km, and encompassing an elevation gradient ranging from 57 to 270 meters covering the NGEE-Arctic Teller watershed (Fig. 1A). To explore the spectral patterns of vegetation, spectral (AVIRIS-NG) and ALD measurements were carry out during peak-season vegetation from July 19 to July 22nd, 2022.. Maximum annual ALD, commonly referred to as active layer thickness (ALT) is

observed at the end of the growing season, but ALD generally increases proportionally to the square root of time since snowmelt (Nelson and Hinkel 2003), allowing to observe the spatial patterns in ALD variability before reaching the maximum thaw depth. Next to thaw depth, also soil moisture and vegetation height were measured at each sample point. At last, the GPS position was measured using a portable Trimble Geo7X differential GPS. The Geo7X was connected to a Zephyr Model 2 Dual Frequency GNSS antenna (Trimble Incorporated, Sunnyvale, California) and sites were logged for at least 1 minute. The nearest base station data from the Trimble Reference Network (https://www.trimble.com/trs/findtrs.asp) were used to post-process the locations to achieve dGPS accuracy. For spatial modeling of the Active Layer Depth (ALD) across the Teller site we created a high-resolution spatially explicit active layer model based on the thaw depth transects in combination with hyperspectral AVIRIS-NG imagery, their derivatives, and the Arctic DEM following the methodology described in chapter 1. The ALD model output will be compared with plant community types mapped by (Konduri et al. 2021) for the 1st- and 2nd-level plant community types.

3.2.2. Remote Sensing Datasets

Airborne hyperspectral imagery was collected over the Teller and Mile 80 sites. The AVIRIS-NG flight lines were collected on 13 July 2022 by the NASA ABoVE airborne campaign (Miller et al. 2018) using the AVIRIS NG imaging spectrometer (400 - 2400 nm, 430 bands) with +-5 m pixel size. We downloaded the reflectance product from the AVIRIS-NG data portal (https://avirisng.jpl.nasa.gov/dataportal/) 2022 - (https://popo.jpl.nasa.gov/avng/y22/). We processed the Arctic-DEM (https://www.pgc.umn.edu/data/arcticdem/) (Porter et al. 2023) to select the best available strip and used it as an elevation model with the matching AVIRIS-NG resolution at 5 m.

3.2.3. Tundra Functional traits

We aim to categorize tundra vegetation with tundra functional traits, reflecting their responses to geomorphological processes, disturbances, and environmental conditions in tundra landscapes

(Kemppinen et al. 2022, 2021). Hyperspectral AVIRIS-NG imagery, available from the ABoVE field campaign (Miller et al. 2018), can be used to detect small changes in vegetation traits and characteristics (S. Serbin and Yang 2021) that could be the first indication of thaw-driven changes in active layer, hydrology, or nutrient availability. In our approach, we use ALD as a proxy for the variability of the tundra landscape as a reflection of the geomorphological processes, disturbances, and environmental conditions. ALD was compared with the functional diversity metrics based on the following selection of spectral traits suggested by (Féret and Boissieu 2020):

- Transformed Chlorophyll Absorption Reflectance Index / Optimized Soil-Adjusted Vegetation Index ratio (TCARI_OSAVI - (Haboudane et al. 2002) provides an estimate of vegetation chlorophyll content, and vegetation vigor, adjusted for variable soil background effects;
- Normalized Difference Leaf Mass Area (ND_LMA -(le Maire et al. 2008) reflects leaf structural parameter leaf mass per unit area. High values indicate vegetation with high mass and density leaves, slower growth rates, and longer longevity reflecting investments in structural defense, durability, and conservation of resources;
- Continuum Removal in Shortwave Infrared (CR_SWIR - (Féret, 2020) index is based on absorption features in the shortwave infrared that reflects the moisture content and structural properties of the vegetation and is related to Equivalent Water Thickness. Low values indicate well-hydrated leaves and a healthy leaf structure;
- Area under continuum removed curve Normalized to the Chlorophyll absorption Bands (ANCB - (Malenovský et al. 2013) is related to Chlorophyll a&b content of the leaves, especially for higher vegetation fraction with high signal to noise;
- Normalized Difference Vegetation Index (NDVI - (Tucker 1979) measures the overall vegetation health and density difference between the near-infrared strongly reflected by vegetation and the

light absorbed by vegetation. A healthy vegetation with greater biomass will have higher NDVI values.

While the spectral indices used lack validation for the tundra landscape or this specific site, our primary focus is not on obtaining precise numeric leaf parameter values but rather on analyzing the spatial patterns and relationships between key functional traits across the tundra landscape and factors such as ALD. These selected spectral indices serve as proxies for the associated vegetation or leaf traits, enabling the mapping and analysis of the spatial variation. Grouping vegetation with similar spectral trait responses into so-called Tundra Functional Types, can be used as predictors of tundra functioning. The concept of tundra functional types originates from Plant Functional Types (PFTs) commonly used in community and ecosystem ecology. PFTs group species with similar responses to environmental changes, disturbances, and contributions to ecosystem functioning. Following (Ordway et al. 2022) we clustered the selected spectral traits into functional types, hypothesizing that the grouped types will reflect below-ground properties. The calculated spectral traits also allow for assessing spatial trends and patterns in vegetation and vegetation health using RS indicators of functional diversity (Angela Lausch et al. 2016). The trait-based functional diversity metrics, functional richness, divergence, and evenness were calculated from the multidimensional trait space (Villéger, Mason, and Mouillot 2008; Schneider et al. 2017) using the biodivMapR package in R (Féret and Boissieu 2020).

3.3. Results

3.3.1. Active Layer Depth Transects

The measured ALD varied between 20 and 120 cm, with a mean of 62.8 cm and a standard deviation of 24.0 cm. The boxplots in Figure 3.1B illustrate the variations in ALD among transects, with the deepest ALD observed along transects 3 and 4, which traverse the site along the water track.

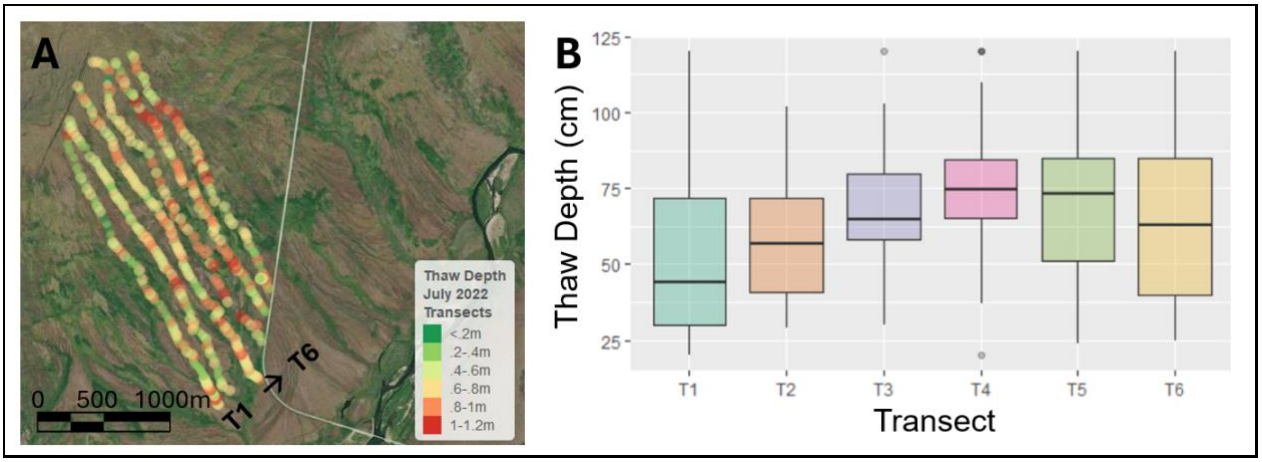

Figure 3.1. Location and overview of the field based active layer depth measurements. 3.1A: The 6 transects covering the NGEE-Arctic study site Teller, red indicates a deeper active layer depth. 3.1B: Boxplots show the variability in thaw depth along the different transects of the Teller study site.

Compared with plant community types mapped by Konduri et al. (2021), no significant differences were observed between mean ALD for the 1st-level plant community types (Fig. 3.2A). When using 2nd-level plant community types, the deepest mean ALD was associated with Willow shrubs (80.2, sd 18.6 cm), followed by Mesic graminoid herb meadow tundra (74.0, sd 19.8 cm) and Rock-talus-glacial-snow (69, sd 9.6 cm). The shallowest mean ALD was observed for drias-lichen dwarf shrub tundra (40.8, sd 10.7 cm) followed by Mixed shrub-sedge tussock tundra (59.1, sd 25.8 cm) and Tussock lichen tundra (57.9, sd 23.0cm). The difference between the means of Willow shrubs (21, 25, 26, 30, 36 - 0.05 / 22 - 0.1) and between 30 - 24 (24 - 25 / 0.1) is significant ($p < 0.05$). We used one-sided ANOVA to test the difference between groups ($p<0.01$) followed by the Tukey HSD ($p<0.05$) to identify the specific groups with significant differences.

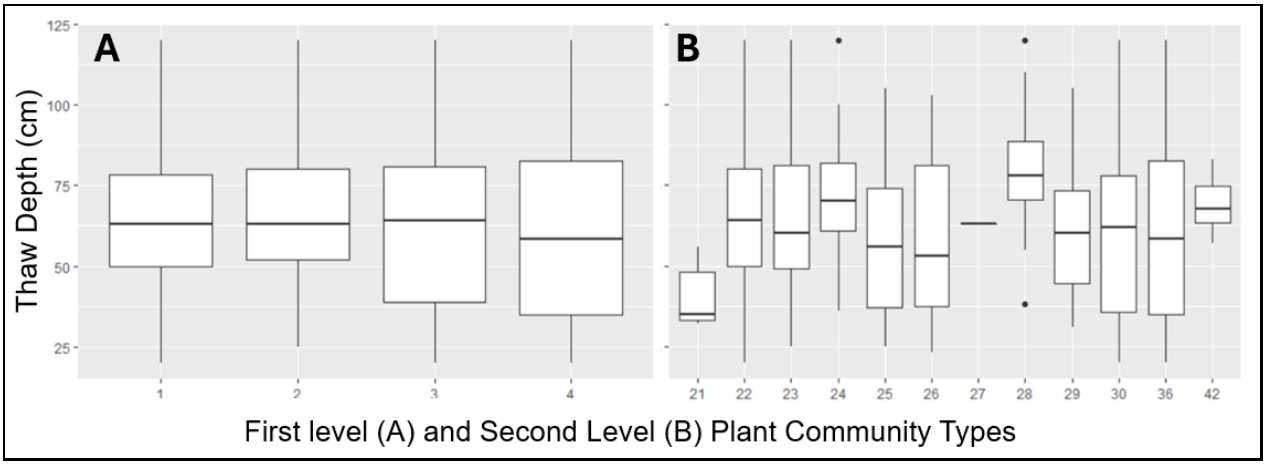

Figure 3.2. The relationship between measured active layer depth and vegetation type for the Teller site. The boxplots in Figure 2A show the ALD distribution for the first-level plant community types (1 Barren, 2 Graminoid - , 3 Shrub-, and 4 Wetland- tundra. Figure 2B shows the variability in ALD along the second-level plant community types: 21: Dryas-lichen dwarf shrub tundra, 22: Ericaceous dwarf shrub tundra, 23: Sedge-willow-Dryas tundra, 24: Mesic graminoid-herb meadow tundra, 25: Tussock-lichen tundra, 26: Mixed shrub-sedge tussock tundra, 27: Birch-Ericaceous-lichen shrub tundra, 28: Willow shrub, 29: Alder-willow shrub, 30: Willow-birch shrub, 36: Wet meadow tundra, and 42: Rock-talus-glacial-snow.

3.3.2. Spatial Distribution of Active Layer Depth

When visually examining the spatial patterns of high-resolution ALD model outputs, the Teller site (Fig. 3.3) shows pronounced large-scale landscape patterns associated with deeper thaw depths, primarily driven by a large gully in the middle of the watershed and smaller water tracks draining into the gully or continuing downslope. The spatial structures associated with ice wedges are characterized by a spatial distinct pattern and relatively shallow thaw depths at the top and bottom of the Teller hillslope.

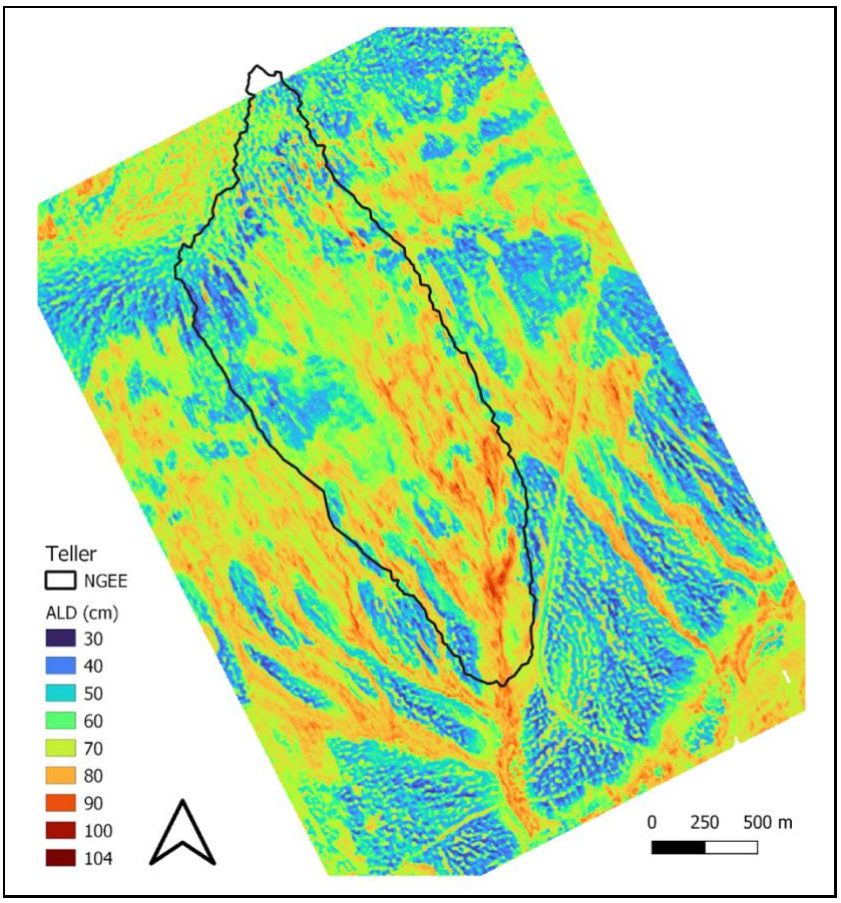

Figure 3.3: High-resolution active layer depth model output, based on the active layer measurements for the Next Generation Ecosystem Experiment - Arctic Teller watershed showing the pronounced deep active layer patterns along the water tracks and the particular shallow active layer ice wedge patterned regions.

3.3.3. AVIRIS-NG Spectral Traits Clusters

For the Teller watershed, five spectral traits are calculated CR_SWIR, TCARI_OSAVI, ANCB, MD_LMA, and NDVI (Fig. 3.4). We use the ALD transects to connect the functional tundra traits with measured ALD, vegetation height, and soil moisture. Table 3.1 shows the correlation coefficient between the spectral traits and field measured ALD, soil moisture, and vegetation height. The spectral indices CR_SWIR, related to Equivalent Water Thickness or the leaf water content, and ANCB, related to Chlorophyll a & b content, show an inverse and weak correlation with ALD and vegetation height. TCARI/OSAVI is related to leaf

chlorophyll content, ND_LMA is related to Leaf Mass per Area, and NDVI shows a correlation with ALD and a stronger correlation with vegetation height.

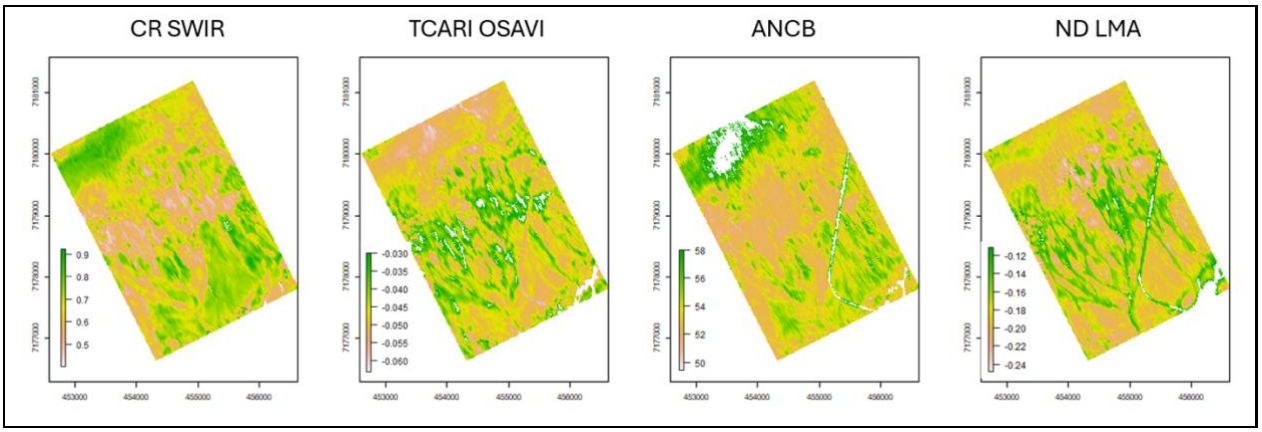

Figure 3.4: AVIRIS-NG derived spectral traits CR_SWIR, TCARI_OSAVI, ANCB, ND_LMA.

Table 3.1: Correlation coefficients (r) between field-measured active layer depth (ALD), soil moisture, vegetation height, and AVIRIS-NG derived spectral traits (* not significant).

	ALD	Soil moisture	Veg. height	NDVI	ND LMA	CR SWIR	TCARI OSAVI
Soil moisture	-0.02*						
Veg. height	0.23	0.13					
NDVI	0.28	-0.25	0.45				
ND LMA	0.26	0.24	0.50	0.61			
CR SWIR	-0.28	0.23	-0.37	-0.88	-0.57		
TCARI OSAVI	0.24	-0.07*	0.56	0.88	0.69	-0.81	
ANCB	-0.15	0.47	-0.21	-0.76	-0.12	0.61	-0.49

We used the spectral traits CR_SWIR, TCARI_OSAVI, ANCB, MD_LMA, and NDVI (Fig. 3.4) as the basis for k-means clustering to identify the functional response classes. First, we reduced the dimensionality of the normalized indices using a PCA. The first two PCA bands account for 88.9% of the cumulative explained variance (PC1: 70.4%, PC2: 18.5%) of the input spectral indices. Key indices for PC1 are NDVI, CR_SWIR, and TCARI_OSAVI, while for PC2, they are ND_LMA and ANCB. Finally, we used the first two PC components as input for the k-means cluster analysis, which was set to four clusters.

Figure 3.5 illustrates the spatial distribution of the functional groups obtained by the kNN classifier (Fig. 3.5A) and the distribution of their associated trait values and ALD (Fig. 3.5B). Class 2 (green) is barely present in the core site, rendering it insufficient for analysis. Two key classes exhibit distinct ALD patterns: class 3 (yellow) corresponds with the deeper ALD values, while class 4 (red) is associated with shallow ALD values. Based on trait values, we can differentiate the vegetation strategies of the distinct functional groups. Class 1 (orange) does not show distinct patterns in functional traits, the ALD and trait values do not differentiate them from classes 3 and 4. As a result, class 1 is not considered a distinct functional group.

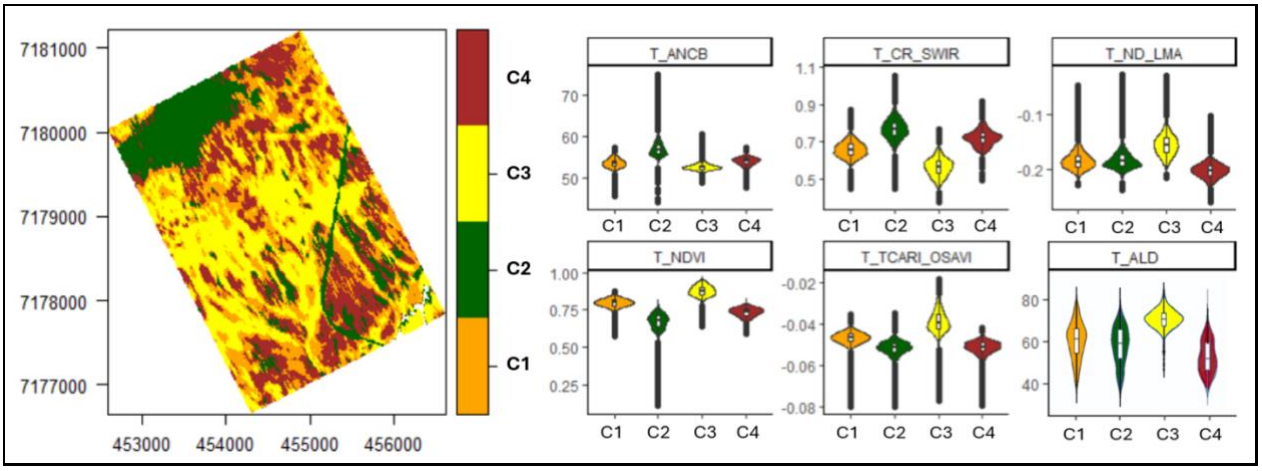

Figure 3.5: Spatial map showing TFT for the Teller site, along with cluster plots showing the distribution of the spectra indices and ALD along vegetation type.

Comparing class 3, which has deeper ALD values, with class 4, which has shallower ALD values, reveals different adaptation strategies of the tundra vegetation. The vegetation properties of Class 3 are characterized by high ND_LMA, NDVI, and TCARI/OSAVI, as well as lower ANCB and CR_SWIR trait values (Fig 3.5). High ND_LMA, or a high mass per unit area, indicates thick and robust leaves associated with relatively slower growth rates but increased durability and resistance to damage. High NDVI values suggest healthy vegetation with dense growth and strong photosynthetic activity. Similarly, high TCARI/OSAVI reflects strong photosynthetic activity due to high chlorophyll content. Surprisingly, ANCB,

another indicator of chlorophyll content, showed lower values, although the differences between groups were smaller for this trait. Lastly, a low CR_SWIR reflects higher leaf moisture content and intact leaf structure, indicating soft and healthy leaves. In contrast, the vegetation in class 4 shows an inverse response for all indices. Class 4 is characterized by reduced photosynthetic activity, sparse vegetation, thinner and less dense leaves, and potential water stress or tougher, drier leaves.

For the Mile 80 site, which has a rather homogeneous vegetation cover, we calculated the same spectral indices and used the first two PC components as input for the k-means cluster analysis, which was set to two clusters. Figure 3.6 shows the spatial patterns of the two distinct tundra trait classes. Compared to Teller (Fig. 3.5), the relative values of ANCB are higher, while the NDVI values are lower. The vegetation properties of type 1 are characterized by higher NDVI and TCARI/OSAVI values, and lower ANCB, CR_SWIR, and ND_LMA trait values compared to type 2. Higher NDVI and TCARI/OSAVI traits suggest a higher photosynthetic activity, chlorophyll content, and overall healthier vegetation. However, this is contradicted by the lower ANCB values. Lower ND_LMA and CR_SWIR values indicate leaves with a lower mass per unit area, or fast-growing thinner leaves with a high moisture content and a more intact leaf structure, suggesting healthier leaves. In contrast, vegetation type 2 has lower NDVI and TCARI/OSAVI values, indicating lower photosynthetic activity and chlorophyll content, which is not supported by the slightly higher ANCB values. The higher CR_SWIR values reflect lower leaf moisture content or damage to the leaf structure, and the slightly higher ND_LMA values indicate thicker, slow-growing, but more durable leaves.

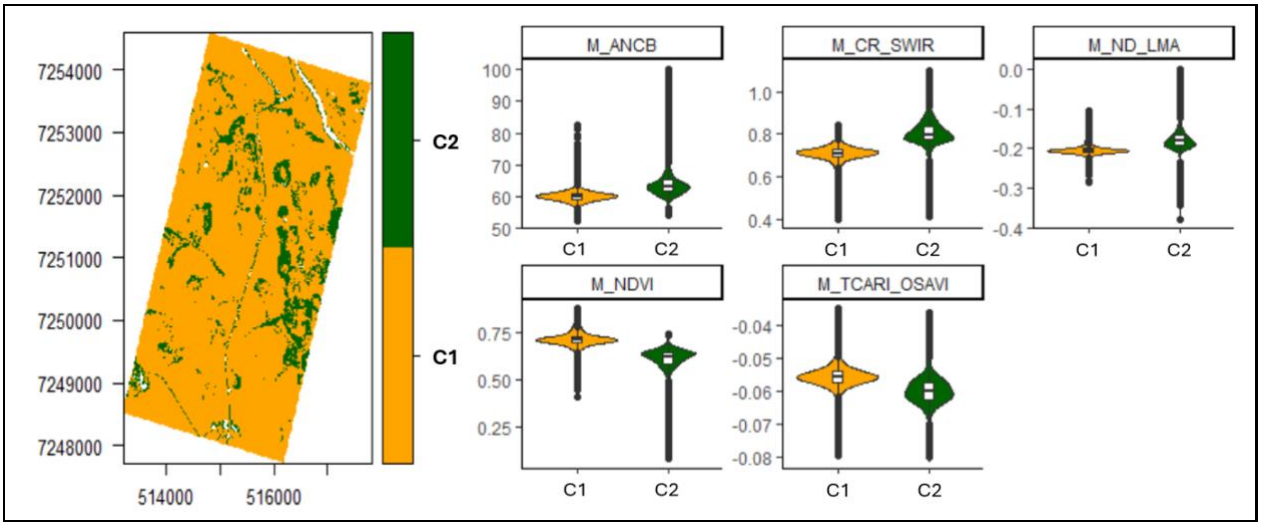

Figure 3.6: Spatial map showing TFT for the Mile 80 site, along with cluster plots showing the distribution of the spectra indices along tundra vegetation type.

Further analyses of the tundra landscapes were based on functional diversity metrics. While the functional diversity metrics for the Telle landscape did not reveal any new patterns compared to the cluster plot, the functional diversity metrics for Mile 80 (Fig. 3.7 - from left to right functional richness, divergence, and evenness) did show an elaborated response. Functional richness or trait space occupied by the tundra communities, shows that the tundra landscape at Mile 80 exhibits low functional richness, suggesting only a limited range of traits are present and the dominance of a specific functional strategy. Areas affected by disturbances show increased functional richness. Functional divergence shows how regular the abundances are in trait space, where undisturbed tundra is characterized by low divergence, showing an overrepresentation of key traits while other traits are underrepresented or rare. The higher functional divergence observed along the disturbance gradients suggests a more equal representation of traits. Lastly, functional evenness reflects the balance between specialization and redundancy, where high evenness or redundant functional roles are observed along disturbances like drained thaw lakes, water tracks, and streams.

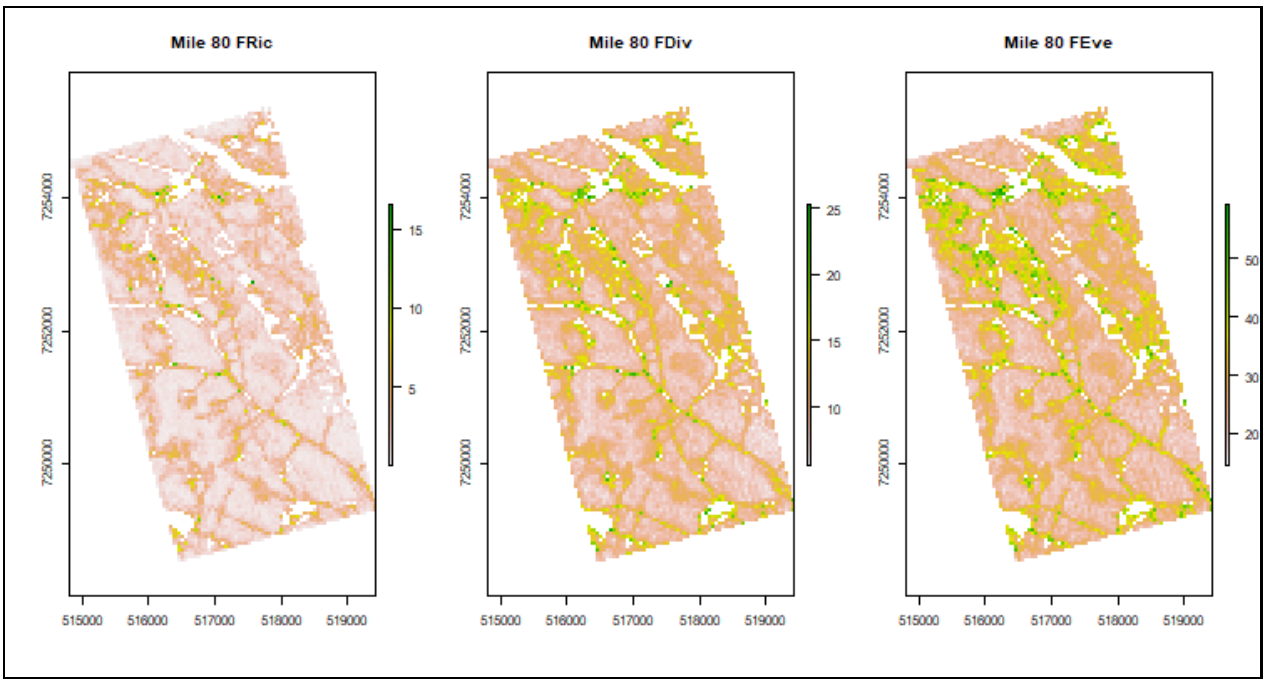

Figure 3.7: Functional diversity (10 pixels radius) of the mile 80 site based on the spectral trait layers.

To study the differences in observed patterns between grouped functional traits and diversity (Fig. 3.6 & 3.7) in detail for Mile 80, we explore the different landscape features and their functional response. Creating an RGB plot of three key spectral traits, R: ND_LMA - G: NDVI - B: CR_SWIR, allows for an in-depth study and understanding of the variability in tundra trait space. As presented in Figure 3.8, different trajectories are observed for the disturbances, which are not detected when clustering traits into two functional groups, and even increasing the number of functional groups does not reveal the same pattern. Two different and opposite responses of the tundra vegetation to disturbances are captured but not visible in the tundra trait clustering and functional diversity metrics. Both transects cover a drained lake, while the red transect shows decreased productivity and the yellow transect shows improved productivity. Interestingly, the water tracks created by the drainage show a similar response as the drained lakes.

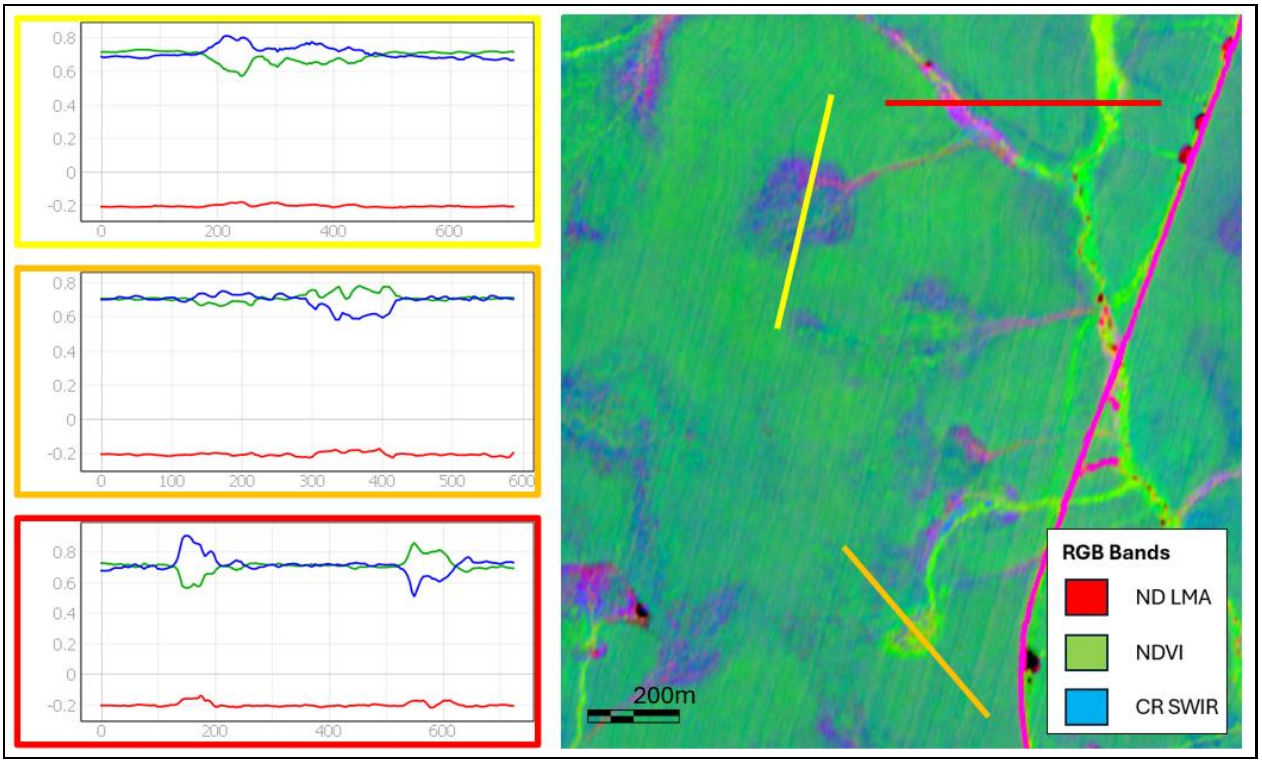

Figure 3.8: Functional trait variability observed at the Mile 80 landscape, indicating different trajectories for disturbance patterns. Band combination used: Red: ND_LMA, Green: NDVI, and Blue: CR_SWIR band.

3.4. Discussion and Conclusion

Text Tundra landscapes represent a dynamic equilibrium between abiotic conditions, disturbance regimes, and species communities. The landscape exhibits patterns driven by self-organization, vegetation succession, and permafrost dynamics (Romme and Knight 1981). Historically, tundra landscapes have been resilient to change, defined as the cumulative disturbances required to shift landscape processes and associated vegetation toward a new stable state (Hirota et al. 2011; Naito and Cairns 2015; Levine et al. 2016; Holling 1973; Curtin and Parker 2014). However, current anthropogenic climate change is pushing tundra landscapes to the limits of resilience, as observed by increased disturbances and shifting patterns (Braghiere et al. 2023). To unravel the dynamics, we used spectrally derived functional traits, specifically those reflecting the with- and within-species variability of leaf traits,

indicative of variations in light availability, environmental conditions such as water and nutrient availability, and disturbance pressure (Osnas et al. 2018; S. P. Serbin et al. 2016; Butler et al. 2017).

First, we studied a heterogeneous hillslope characterized by two vegetation types with distinct adaptation strategies. One vegetation type exhibits healthy, well-hydrated, and robust durable leaves with high photosynthetic activity, suggesting near-optimal growing conditions with ample moisture and nutrients. The other vegetation type had faster growing but less durable leaves and lower photosynthetic activity, suggesting poorer vegetation health and less optimal growing conditions with periods of inadequate moisture or limited nutrient availability. The observed vegetation type patterns corresponded with modeled ALD patterns, and the correlation coefficients between spectral traits and measured ALD suggest that taller and healthier vegetation is associated with deeper ALD. Second, we studied a homogenous tundra landscape with limited topographic variation. Our clustering approach characterized two vegetation types with distinct adaptation strategies. The base vegetation is characterized by relatively fast-growing leaves and high photosynthetic activity suggesting relatively healthy vegetation without large moisture or nutrient deficits. In contrast, the disturbance-associated vegetation had a relatively low photosynthetic activity and health. The relatively homogeneous tundra landscape of Mile 80 provides the environment to explore the ability of functional traits and functional diversity metrics to capture ecosystem responses to environmental conditions and disturbances. In resource-limited and harsh environments functional richness reflects the constraints imposed by the landscape on species and traits, and captures the functional adaptations along gradients (Lamanna et al. 2014; Schumm et al. 2019). High functional divergence can be interpreted as a relaxed ecological filter, allowing for functional redundancy (Ricotta et al. 2020). Low functional evenness signifies specialization and efficient resource use (Mason et al. 2005), which may increase vulnerability to disturbance, whereas high evenness implies redundant functional roles promoting stability. Generally, high functional richness,

divergence, and evenness are linked with more stable landscapes, where redundant functional groups or a fully occupied functional space enhances resilience to disturbances. Translating this to the tundra landscape, we can conclude that disturbances create a window of opportunity for plant species initially unable to establish. Making it unlikely that disturbed tundra landscapes will return to their undisturbed, but more vulnerable state. Feedback mechanisms between the vegetation and soil properties can exacerbate this trend. Our functional diversity maps allow for a spatially continuous assessment of plant functional diversity linked to ecosystem stability (Lausch et al. 2016; Schneider et al. 2017), without prior taxonomic info. Interestingly, our detailed analysis of spectral traits shows that clustering detected vegetation patterns associated with reduced economic traits (browning) but not those with improved economic traits (greening) as shown in Figure 3.8.

In the Tundra landscape, warming is expected to drive an increase in vegetation height and leaf size traits, but the direction of the relationship was largely determined by soil moisture (Bjorkman et al. 2018; Thomas et al. 2020). This highlights the importance of assessing a balanced set of plant functional traits to determine the functional drivers and responses of the Tundra landscape. Based on the spectral traits and spectral trait diversity at Teller, the predicted increasing thaw depth, where deeper thaw depths are associated with taller vegetation. For Mile 80, we suggest a similar effect with increasing vegetation height and leaf traits will be observed along water tracks. This indicates that spectral traits and spectral trait diversity can provide insights into current and future shifts in vegetation or ecosystem trajectories.

Employing spectral traits or their functional diversity will also enable functional diversity from space (Rossi et al. 2020; Hauser et al. 2021), improve the scaling towards the pan-arctic using sentinel-2 (Ma et al. 2019) or the application of future multi- and hyperspectral satellites able to RS traits, that could be used to improve the modeling of key vegetation parameters as demonstrated by improved RS-driven

trait-based models to map vegetation productivity at larger scales (Wieczynski et al. 2022). This can be extended by using functional traits or diversity measures to improve the prediction of other ecosystem functions and below- and aboveground processes like energy balance and nutrient cycling. Therefore, functional traits and their diversity metrics can become predictors of key arctic ecosystem functions.

In summary, we demonstrated that functional traits allow for the quantification of high-resolution spatial variation of tundra landscapes. For Teller, with its diverse vegetation patterns, we observed a functioning relationship between tundra vegetation types and the state of the permafrost. In contrast, disturbances and upcoming shifts in vegetation were observed for Mile 80, characterized by uniform Tussock tundra vegetation.

BIBLIOGRAPHY

Abbott, B. W., J. B. Jones, S. E. Godsey, J. R. Larouche, and W. B. Bowden. 2015. "Patterns and Persistence of Hydrologic Carbon and Nutrient Export from Collapsing Upland Permafrost." Biogeosciences 12 (12): 3725–40.

Allen Broughton, S., and Kurt Bryan. 2011. Discrete Fourier Analysis and Wavelets: Applications to Signal and Image Processing. John Wiley & Sons.

Anderson, John E., Thomas A. Douglas, Robyn A. Barbato, Stephanie Saari, Jarrod D. Edwards, and Robert M. Jones. 2019. "Linking Vegetation Cover and Seasonal Thaw Depths in Interior Alaska Permafrost Terrains Using Remote Sensing." Remote Sensing of Environment 233 (November): 111363.

Arévalo, Paulo, Eric L. Bullock, Curtis E. Woodcock, and Pontus Olofsson. 2020. "A Suite of Tools for Continuous Land Change Monitoring in Google Earth Engine." Frontiers in Climate 2. https://doi.org/10.3389/fclim.2020.576740.

Armstrong, Lindsay, Denis Lacelle, Robert H. Fraser, Steve Kokelj, and Anders Knudby. 2018. "Thaw Slump Activity Measured Using Stationary Cameras in Time-Lapse and Structure-from-Motion Photogrammetry." Arctic Science 4 (4): 827–45.

Asner, G. P., C. B. Anderson, R. E. Martin, D. E. Knapp, R. Tupayachi, F. Sinca, and Y. Malhi. 2014. "Landscape-Scale Changes in Forest Structure and Functional Traits along an Andes-to-Amazon Elevation Gradient." Biogeosciences. https://doi.org/10.5194/bg-11-843-2014.

Asner, G. P., R. E. Martin, D. E. Knapp, R. Tupayachi, C. B. Anderson, F. Sinca, N. R. Vaughn, and W. Llactayo. 2017. "Airborne Laser-Guided Imaging Spectroscopy to Map Forest Trait Diversity and Guide Conservation." Science 355 (6323): 385–89.

Atkins, Jeff W., Jennifer Costanza, Kyla M. Dahlin, Matthew P. Dannenberg, Andrew J. Elmore, Matthew C. Fitzpatrick, Christopher R. Hakkenberg, et al. 2023. "Scale Dependency of Lidar-derived Forest Structural Diversity." Methods in Ecology and Evolution / British Ecological Society 14 (2): 708–23.

Bartsch, Annett, Tazio Strozzi, and Ingmar Nitze. 2023. "Permafrost Monitoring from Space." Surveys in Geophysics 44 (5): 1579–1613.

Beamish, Alison, Martha K. Raynolds, Howard Epstein, Gerald V. Frost, Matthew J. Macander, Helena Bergstedt, Annett Bartsch, et al. 2020. "Recent Trends and Remaining Challenges for Optical Remote Sensing of Arctic Tundra Vegetation: A Review and Outlook." Remote Sensing of Environment 246 (September): 111872.

Beck, Pieter S. A., and Scott J. Goetz. 2011. "Satellite Observations of High Northern Latitude Vegetation Productivity Changes between 1982 and 2008: Ecological Variability and Regional Differences." Environmental Research Letters: ERL [Web Site]. https://doi.org/10.1088/1748-9326/6/4/045501.

Bennett, Katrina E., Greta Miller, Robert Busey, Min Chen, Emma R. Lathrop, Julian B. Dann, Mara Nutt, et al. 2022. "Spatial Patterns of Snow Distribution in the Sub-Arctic." The Cryosphere 16 (8): 3269–93.

Bjorkman, Anne D., Isla H. Myers-Smith, Sarah C. Elmendorf, Signe Normand, Nadja Rüger, Pieter S. A. Beck, Anne Blach-Overgaard, et al. 2018. “Plant Functional Trait Change across a Warming Tundra Biome.” Nature, no. 562: 57–62.

Blok, Daan, Gabriela Schaepman-Strub, Harm Bartholomeus, Monique M. P. D. Heijmans, Trofim C. Maximov, and Frank Berendse. 2011. “The Response of Arctic Vegetation to the Summer Climate: Relation between Shrub Cover, NDVI, Surface Albedo and Temperature.” Environmental Research Letters: ERL [Web Site] 6 (3). https://doi.org/10.1088/1748-9326/6/3/035502.

Blume-Werry, Gesche, Ann Milbau, Laurenz M. Teuber, Margareta Johansson, and Ellen Dorrepaal. 2019. “Dwelling in the Deep - Strongly Increased Root Growth and Rooting Depth Enhance Plant Interactions with Thawing Permafrost Soil.” The New Phytologist 223 (3): 1328–39.

Bradshaw, Corey J. A., and Ian G. Warkentin. 2015. “Global Estimates of Boreal Forest Carbon Stocks and Flux.” Global and Planetary Change 128 (May): 24–30.

Braghiere, Renato K., Joshua B. Fisher, Kimberley R. Miner, Charles E. Miller, John R. Worden, David S. Schimel, and Christian Frankenberg. 2023. “Tipping Point in North American Arctic-Boreal Carbon Sink Persists in New Generation Earth System Models despite Reduced Uncertainty.” Environmental Research Letters: ERL [Web Site] 18 (2): 025008.

Breiman, Leo. 2001. “Random Forests.” Machine Learning 45 (1): 5–32.

Butler, Ethan E., Abhirup Datta, Habacuc Flores-Moreno, Ming Chen, Kirk R. Wythers, Farideh Fazayeli, Arindam Banerjee, et al. 2017. “Mapping Local and Global Variability in Plant Trait Distributions.” Proceedings of the National Academy of Sciences of the United States of America 114 (51): E10937–46.

Cadotte, Marc W., Kelly Carscadden, and Nicholas Mirotchnick. 2011. “Beyond Species: Functional Diversity and the Maintenance of Ecological Processes and Services.” The Journal of Applied Ecology 48 (5): 1079–87.

Cohen, Judah, James A. Screen, Jason C. Furtado, Mathew Barlow, David Whittleston, Dim Coumou, Jennifer Francis, et al. 2014. “Recent Arctic Amplification and Extreme Mid-Latitude Weather.” Nature Geoscience 7 (9): 627–37.

Cohen, Warren B., Zhiqiang Yang, Sean P. Healey, Robert E. Kennedy, and Noel Gorelick. 2018. “A LandTrendr Multispectral Ensemble for Forest Disturbance Detection.” Remote Sensing of Environment 205 (February): 131–40.

Conrad, O., B. Bechtel, M. Bock, Helge Dietrich, E. Fischer, L. Gerlitz, J. Wehberg, V. Wichmann, and J. Böhner. 2015. “System for Automated Geoscientific Analyses (SAGA) v. 2.1.4.” Geoscientific Model Development Discussions 8 (July): 2271–2312.

Correll, M. D., C. S. Elphick, W. Hantson, B. B. Cline, E. L. Tymkiw, W. Gregory Shriver, and B. J. Olsen. 2019. “A Multi-Scale Comparison of Elevation Measurement Methods in Northeastern Tidal Marshes of the United States.” Wetlands 39 (3). https://doi.org/10.1007/s13157-018-1110-x.

Csillag, Ferenc, and Sándor Kabos. 2002. “Wavelets, Boundaries, and the Spatial Analysis of Landscape Pattern.” Écoscience 9 (2): 177–90.

Curtin, Charles G., and Jessica P. Parker. 2014. “Foundations of Resilience Thinking.” Conservation Biology: The Journal of the Society for Conservation Biology 28 (4): 912–23.

Dale, M. R. T., and M. Mah. 1998. “The Use of Wavelets for Spatial Pattern Analysis in Ecology.” Journal of Vegetation Science: Official Organ of the International Association for Vegetation Science 9 (6): 805–14.

Díaz, Sandra, Jens Kattge, Johannes H. C. Cornelissen, Ian J. Wright, Sandra Lavorel, Stéphane Dray, Björn Reu, et al. 2016. “The Global Spectrum of Plant Form and Function.” Nature 529 (7585): 167–71.

Díaz, Sandra, and Marcelo Cabido. 2001. “Vive La Différence: Plant Functional Diversity Matters to Ecosystem Processes.” Trends in Ecology & Evolution 16 (11): 646–55.

Döpper, Veronika, Santosh Panda, Christine Waigl, Matthias Braun, and Hannes Feilhauer. 2021. “Using Floristic Gradient Mapping to Assess Seasonal Thaw Depth in Interior Alaska.” Applied Vegetation Science 24 (1): 1–11.

Engstrom, R., A. Hope, H. Kwon, D. Stow, and D. Zamolodchikov. 2005. “Spatial Distribution of near Surface Soil Moisture and Its Relationship to Microtopography in the Alaskan Arctic Coastal Plain.” Hydrology Research 36 (3): 219–34.

Evans, J. S., and K. Ram. 2021. “Package ‘spatialEco.’” R CRAN Project. http://r.meteo.uni.wroc.pl/web/packages/spatialEco/spatialEco.pdf.

Féret, Jean-Baptiste, and Florian Boissieu. 2020. “biodivMapR: An R Package for α- and β-diversity Mapping Using Remotely Sensed Images.” Methods in Ecology and Evolution / British Ecological Society 11 (1): 64–70.

Fisher, James P., Cristian Estop-Aragonés, Aaron Thierry, Dan J. Charman, Stephen A. Wolfe, Iain P. Hartley, Julian B. Murton, Mathew Williams, and Gareth K. Phoenix. 2016. “The Influence of Vegetation and Soil Characteristics on Active-Layer Thickness of Permafrost Soils in Boreal Forest.” Global Change Biology. https://doi.org/10.1111/gcb.13248.

Fisher, Joshua B., Daniel J. Hayes, Christopher R. Schwalm, Deborah N. Huntzinger, Eric Stofferahn, Kevin Schaefer, Yiqi Luo, et al. 2018. “Missing Pieces to Modeling the Arctic-Boreal Puzzle.” Environmental Research Letters: ERL [Web Site] 13 (2). https://doi.org/10.1088/1748-9326/aa9d9a.

Fraser, Robert H., Ian Olthof, Trevor C. Lantz, and Carla Schmitt. 2016. “UAV Photogrammetry for Mapping Vegetation in the Low-Arctic.” Arctic Science 2 (3): 79–102.

French, Hugh M. 2007. The Periglacial Environment. John Wiley & Sons.

Funk, Jennifer L., Julie E. Larson, Gregory M. Ames, Bradley J. Butterfield, Jeannine Cavender-Bares, Jennifer Firn, Daniel C. Laughlin, Ariana E. Sutton-Grier, Laura Williams, and Justin Wright. 2017. “Revisiting the Holy Grail: Using Plant Functional Traits to Understand Ecological Processes.” Biological Reviews of the Cambridge Philosophical Society 92 (2): 1156–73.

Gangodagamage, Chandana, Joel C. Rowland, Susan S. Hubbard, Steven P. Brumby, Anna K. Liljedahl, Haruko Wainwright, Cathy J. Wilson, et al. 2014. “Extrapolating Active Layer Thickness Measurements across Arctic Polygonal Terrain Using LiDAR and NDVI Data Sets.” Water Resources Research 50 (8): 6339–57.

Genet, H., A. D. McGuire, K. Barrett, A. Breen, E. S. Euskirchen, J. F. Johnstone, E. S. Kasischke, et al. 2013. “Modeling the Effects of Fire Severity and Climate Warming on Active Layer Thickness and Soil Carbon Storage of Black Spruce Forests across the Landscape in Interior Alaska.” Environmental Research Letters: ERL [Web Site] 8 (4): 045016.

Genuer, Robin, Jean-Michel Poggi, and Christine Tuleau-Malot. 2010. “Variable Selection Using Random Forests.” Pattern Recognition Letters 31 (14): 2225–36.

Gomersall, Claire E., and Kenneth M. Hinkel. 2010. “Estimating the Variability of Active-Layer Thaw Depth in Two Physiographic Regions of Northern Alaska.” Geographical Analysis 33 (2): 141–55.

Gorelick, Noel, Matt Hancher, Mike Dixon, Simon Ilyushchenko, David Thau, and Rebecca Moore. 2017. “Google Earth Engine: Planetary-Scale Geospatial Analysis for Everyone.” Remote Sensing of Environment 202 (December): 18–27.
Goward, Samuel, Terry Arvldson, Darrel Williams, John Faundeen, James Irons, and Shannon Franks. 2006. “Historical Record of Landsat Global Coverage : Mission Operations, NSLRSDA, and International Cooperator Stations.” Photogrammetric Engineering and Remote Sensing 72 (10): 1155–69.

Graham, L. J., R. Spake, S. Gillings, K. Watts, and F. Eigenbrod. 2019. “Incorporating Fine-Scale Environmental Heterogeneity into Broad-Extent Models, Methods Ecol. Evol., 10, 767--778.”

Grosse, Guido, Jennifer Harden, Merritt Turetsky, A. David McGuire, Philip Camill, Charles Tarnocai, Steve Frolking, et al. 2011. “Vulnerability of High-Latitude Soil Organic Carbon in North America to Disturbance.” Journal of Geophysical Research: Biogeosciences 116 (3): 1–23.

Haboudane, Driss, John R. Miller, Nicolas Tremblay, Pablo J. Zarco-Tejada, and Louise Dextraze. 2002. “Integrated Narrow-Band Vegetation Indices for Prediction of Crop Chlorophyll Content for Application to Precision Agriculture.” Remote Sensing of Environment 81 (2): 416–26.

Hall, Kevin. 2007. “The Periglacial Environment Hugh M. French John Wiley and Sons, 2007 ISBN 13:978-0-470-86588-0, 458 Pages, £80.” Antarctic Science / Blackwell Scientific Publications 19 (4): 535–36.

Hansen, M. C., P. V. Potapov, R. Moore, M. Hancher, S. A. Turubanova, A. Tyukavina, D. Thau, et al. 2013. “High-Resolution Global Maps of 21st-Century Forest Cover Change.” Science 342 (6160): 850–53.

Hauser, Leon T., Jean-Baptiste Féret, Nguyen An Binh, Niels van der Windt, ngelo F. Sil, Joris Timmermans, Nadejda A. Soudzilovskaia, and Peter M. van Bodegom. 2021. “Towards Scalable Estimation of Plant Functional Diversity from Sentinel-2: In-Situ Validation in a Heterogeneous (semi-)natural Landscape.” Remote Sensing of Environment 262 (September): 112505.

Hayes, Daniel J., David W. Kicklighter, A. David McGuire, Min Chen, Qianlai Zhuang, Fengming Yuan, Jerry M. Melillo, and Stan D. Wullschleger. 2014. “The Impacts of Recent Permafrost Thaw on Land–atmosphere Greenhouse Gas Exchange.” Environmental Research Letters: ERL [Web Site] 9 (4): 045005.

Healey, Sean P., Warren B. Cohen, Zhiqiang Yang, C. Kenneth Brewer, Evan B. Brooks, Noel Gorelick, Alexander J. Hernandez, et al. 2018. “Mapping Forest Change Using Stacked Generalization: An Ensemble Approach.” Remote Sensing of Environment 204 (January): 717–28.

Heijmans, Monique M. P. D., Rúna Í. Magnússon, Mark J. Lara, Gerald V. Frost, Isla H. Myers-Smith, Jacobus van Huissteden, M. Torre Jorgenson, et al. 2022. “Tundra Vegetation Change and Impacts on Permafrost.” Nature Reviews Earth & Environment 3 (1): 68–84.

Hermes, Anna L., Haruko M. Wainwright, Oliver Wigmore, Nicola Falco, Noah P. Molotch, and Eve-Lyn S. Hinckley. 2020. “From Patch to Catchment: A Statistical Framework to Identify and Map Soil Moisture Patterns Across Complex Alpine Terrain.” Frontiers in Water 2. https://doi.org/10.3389/frwa.2020.578602.

Hirota, Marina, Milena Holmgren, Egbert H. Van Nes, and Marten Scheffer. 2011. “Global Resilience of Tropical Forest and Savanna to Critical Transitions.” Science 334 (6053): 232–35.

Hislop, Samuel, Simon Jones, Mariela Soto-Berelov, Andrew Skidmore, Andrew Haywood, and Trung H. Nguyen. 2019. “A Fusion Approach to Forest Disturbance Mapping Using Time Series Ensemble Techniques.” Remote Sensing of Environment 221 (February): 188–97.

Holling, C. S. 1973. “Resilience and Stability of Ecological Systems.” Annual Review of Ecology and Systematics 4: 1–23.

Holloway, Jean E., Antoni G. Lewkowicz, Thomas A. Douglas, Xiaoying Li, Merritt R. Turetsky, Jennifer L. Baltzer, and Huijun Jin. 2020. “Impact of Wildfire on Permafrost Landscapes: A Review of Recent Advances and Future Prospects.” Permafrost and Periglacial Processes 31 (3): 371–82.

Huang, Lingcao, Lin Liu, Liming Jiang, and Tingjun Zhang. 2018. “Automatic Mapping of Thermokarst Landforms from Remote Sensing Images Using Deep Learning: A Case Study in the Northeastern Tibetan Plateau.” Remote Sensing 10 (12). https://doi.org/10.3390/rs10122067.

Hugelius, G., J. Strauss, S. Zubrzycki, J. W. Harden, E. A. G. G. Schuur, C. L. Ping, L. Schirrmeister, et al. 2014a. “Estimated Stocks of Circumpolar Permafrost Carbon with Quantified Uncertainty Ranges and Identified Data Gaps.” Biogeosciences Discussions . https://doi.org/10.5194/bg-11-6573-2014.

Hugelius, G., J. Strauss, S. Zubrzycki, J. W. Harden, E. A. G. Schuur, C. L. Ping, L. Schirrmeister, et al. 2014b. “Improved Estimates Show Large Circumpolar Stocks of Permafrost Carbon While Quantifying Substantial Uncertainty Ranges and Identifying Remaining Data Gaps.” Biogeosciences Discussions . https://doi.org/10.5194/bgd-11-4771-2014.

Hugelius, Gustaf, Julie Loisel, Sarah Chadburn, Robert B. Jackson, Miriam Jones, Glen MacDonald, Maija Marushchak, et al. 2020. “Large Stocks of Peatland Carbon and Nitrogen Are Vulnerable to Permafrost Thaw.” Proceedings of the National Academy of Sciences of the United States of America 117 (34): 20438–46.

Huissteden, J. van. 2020. Thawing Permafrost.

Huntzinger, D. N., K. Schaefer, C. Schwalm, J. B. Fisher, D. Hayes, E. Stofferahn, J. Carey, et al. 2020. "Evaluation of Simulated Soil Carbon Dynamics in Arctic-Boreal Ecosystems." Environmental Research Letters: ERL [Web Site] 15 (2): 025005.

Jetz, Walter, Jeannine Cavender-Bares, Ryan Pavlick, David Schimel, Frank W. Davis, Gregory P. Asner, Robert Guralnick, et al. 2016. "Monitoring Plant Functional Diversity from Space." Nature Plants 2 (March): 16024.

Jones, Benjamin M., Guido Grosse, Christopher D. Arp, Eric Miller, Lin Liu, Daniel J. Hayes, and Christopher F. Larsen. 2015. "Recent Arctic Tundra Fire Initiates Widespread Thermokarst Development." Scientific Reports 5 (October): 15865.

Jones, B. M., G. Grosse, C. D. Arp, M. C. Jones, K. M. Walter Anthony, and V. E. Romanovsky. 2011. "Modern Thermokarst Lake Dynamics in the Continuous Permafrost Zone, Northern Seward Peninsula, Alaska." Journal of Geophysical Research 116 (G00M03). https://doi.org/10.1029/2011jg001666.

Jorgenson, Mark Torre, and Guido Grosse. 2016. "Remote Sensing of Landscape Change in Permafrost Regions." Permafrost and Periglacial Processes 27 (4): 324–38.

Jorgenson, M. Torre, Vladimir Romanovsky, Jennifer Harden, Yuri Shur, Jonathan O'Donnell, Edward A. G. Schuur, Mikhail Kanevskiy, and Sergei Marchenko. 2010. "Resilience and Vulnerability of Permafrost to Climate Change." Canadian Journal of Forest Research. Journal Canadien de La Recherche Forestiere 40 (7): 1219–36.

Ju, Junchang, and Jeffrey G. Masek. 2016. "The Vegetation Greenness Trend in Canada and US Alaska from 1984–2012 Landsat Data." Remote Sensing of Environment 176 (April): 1–16.

Kartoziia, Andrei. 2019. "Assessment of the Ice Wedge Polygon Current State by Means of UAV Imagery Analysis (Samoylov Island, the Lena Delta)." Remote Sensing 11 (13). https://doi.org/10.3390/rs11131627.

Kemppinen, Julia, Pekka Niittynen, Konsta Happonen, Peter C. Roux, Juha Aalto, Jan Hjort, Tuija Maliniemi, et al. 2022. "Geomorphological Processes Shape Plant Community Traits in the Arctic." Global Ecology and Biogeography: A Journal of Macroecology, May. https://doi.org/10.1111/geb.13512.

Kemppinen, Julia, Pekka Niittynen, Anna-Maria Virkkala, Konsta Happonen, Henri Riihimäki, Juha Aalto, and Miska Luoto. 2021. "Dwarf Shrubs Impact Tundra Soils: Drier, Colder, and Less Organic Carbon." Ecosystems 24 (6): 1378–92.

Kennedy, Robert E., Zhiqiang Yang, and Warren B. Cohen. 2010. "Detecting Trends in Forest Disturbance and Recovery Using Yearly Landsat Time Series: 1. LandTrendr - Temporal Segmentation Algorithms." Remote Sensing of Environment 114 (12): 2897–2910.

Kennedy, Robert E., Zhiqiang Yang, Noel Gorelick, Justin Braaten, Lucas Cavalcante, Warren B. Cohen, and Sean Healey. 2018. "Implementation of the LandTrendr Algorithm on Google Earth Engine." Remote Sensing 10 (5): 691.

Konduri, Venkata, Amy Breen, William Hargrove, Forrest Hoffman, Verity Salmon, Colleen Iversen, Auroop Ganguly, and Jitendra Kumar. 2021. "Hyperspectral Remote Sensing-Based Plant Community Map for

Region around NGEE-Arctic Intensive Research Watersheds at Seward Peninsula, Alaska, 2017-2019." Next Generation Ecosystems Experiment - Arctic, Oak Ridge National Laboratory (ORNL), Oak Ridge, TN (US); NGEE Arctic, Oak Ridge National Laboratory (ORNL), Oak Ridge, TN (United States). https://doi.org/10.5440/1828604.

Lamanna, Christine, Benjamin Blonder, Cyrille Violle, Nathan J. B. Kraft, Brody Sandel, Irena Šímová, John C. Donoghue 2nd, et al. 2014. "Functional Trait Space and the Latitudinal Diversity Gradient." Proceedings of the National Academy of Sciences of the United States of America 111 (38): 13745–50.

Lara, M. J., A. D. McGuire, E. S. Euskirchen, H. Genet, S. Yi, R. Rutter, C. Iversen, V. Sloan, and S. D. Wullschleger. 2020. "Local-Scale Arctic Tundra Heterogeneity Affects Regional-Scale Carbon Dynamics." Nature Communications 11 (1): 1–10.

Lausch, A., L. Bannehr, M. Beckmann, C. Boehm, H. Feilhauer, J. M. Hacker, M. Heurich, et al. 2016. "Linking Earth Observation and Taxonomic, Structural and Functional Biodiversity: Local to Ecosystem Perspectives." Ecological Indicators 70: 317–39.

Lausch, Angela, Stefan Erasmi, Douglas J. King, Paul Magdon, and Marco Heurich. 2016. "Understanding Forest Health with Remote Sensing-Part I-A Review of Spectral Traits, Processes and Remote-Sensing Characteristics." Remote Sensing. https://doi.org/10.3390/rs8121029.

Lavorel, S., and E. Garnier. 2002. "Predicting Changes in Community Composition and Ecosystem Functioning from Plant Traits: Revisiting the Holy Grail." Functional Ecology. https://doi.org/10.1046/j.1365-2435.2002.00664.x.

Levine, Naomi M., Ke Zhang, Marcos Longo, Alessandro Baccini, Oliver L. Phillips, Simon L. Lewis, Esteban Alvarez-Dávila, et al. 2016. "Ecosystem Heterogeneity Determines the Ecological Resilience of the Amazon to Climate Change." Proceedings of the National Academy of Sciences of the United States of America 113 (3): 793–97.

Liljedahl, Anna K., Julia Boike, Ronald P. Daanen, Alexander N. Fedorov, Gerald V. Frost, Guido Grosse, Larry D. Hinzman, et al. 2016. "Pan-Arctic Ice-Wedge Degradation in Warming Permafrost and Its Influence on Tundra Hydrology." Nature Geoscience 9 (4): 312–18.

Li, Xiao-Ying, Hui-Jun Jin, Hong-Wei Wang, Sergey S. Marchenko, Wei Shan, Dong-Liang Luo, Rui-Xia He, et al. 2021. "Influences of Forest Fires on the Permafrost Environment: A Review." Advances in Climate Change Research 12 (1): 48–65.

Loranty, Michael M., Benjamin W. Abbott, Daan Blok, Thomas A. Douglas, Howard E. Epstein, Bruce C. Forbes, Benjamin M. Jones, et al. 2018. "Reviews and Syntheses: Changing Ecosystem Influences on Soil Thermal Regimes in Northern High-Latitude Permafrost Regions." Biogeosciences 15 (17): 5287–5313.

Madritch, Michael, Jeannine Cavender-Bares, Sarah E. Hobbie, and Philip A. Townsend. 2020. "Linking Foliar Traits to Belowground Processes." In Remote Sensing of Plant Biodiversity, 173–97. Springer, Cham.

Maire, Guerric le, Christophe François, Kamel Soudani, Daniel Berveiller, Jean-Yves Pontailler, Nathalie Bréda, Hélène Genet, Hendrik Davi, and Eric Dufrêne. 2008. "Calibration and Validation of Hyperspectral

Indices for the Estimation of Broadleaved Forest Leaf Chlorophyll Content, Leaf Mass per Area, Leaf Area Index and Leaf Canopy Biomass." Remote Sensing of Environment 112 (10): 3846–64.

Malenovský, Zbyněk, Lucie Homolová, Raúl Zurita-Milla, Petr Lukeš, Věroslav Kaplan, Jan Hanuš, Jean-Philippe Gastellu-Etchegorry, and Michael E. Schaepman. 2013. "Retrieval of Spruce Leaf Chlorophyll Content from Airborne Image Data Using Continuum Removal and Radiative Transfer." Remote Sensing of Environment 131 (April): 85–102.

Mason, Norman W. H., David Mouillot, William G. Lee, and J. Bastow Wilson. 2005. "Functional Richness , Functional Evenness and Functional Divergence : The Primary Components of Functional Diversity." Oikos 111: 112–18.

Matsuoka, Norikazu, Atsushi Ikeda, and Takeshi Date. 2005. "Morphometric Analysis of Solifluction Lobes and Rock Glaciers in the Swiss Alps." Permafrost and Periglacial Processes 16 (1): 99–113.

Ma, Xuanlong, Miguel D. Mahecha, Mirco Migliavacca, Fons van der Plas, Raquel Benavides, Sophia Ratcliffe, Jens Kattge, et al. 2019. "Inferring Plant Functional Diversity from Space: The Potential of Sentinel-2." Remote Sensing of Environment 233 (November): 111368.

McGuire, A. David, Leif G. Anderson, Torben R. Christensen, Scott Dallimore, Laodong Guo, Daniel J. Hayes, Martin Heimann, Thomas D. Lorenson, Robie W. Macdonald, and Nigel Roulet. 2009. "Sensitivity of the Carbon Cycle in the Arctic to Climate Change." Ecological Monographs 79 (4): 523–55.

McGuire, A. David, David M. Lawrence, Charles Koven, Joy S. Clein, Eleanor Burke, Guangsheng Chen, Elchin Jafarov, et al. 2018. "Dependence of the Evolution of Carbon Dynamics in the Northern Permafrost Region on the Trajectory of Climate Change." Proceedings of the National Academy of Sciences of the United States of America 115 (15): 3882–87.

McGuire, A. D., T. R. Christensen, D. Hayes, A. Heroult, E. Euskirchen, J. S. Kimball, C. Koven, et al. 2012. "An Assessment of the Carbon Balance of Arctic Tundra: Comparisons among Observations, Process Models, and Atmospheric Inversions." Biogeosciences 9 (8): 3185–3204.

McGuire, A. D., C. Wirth, M. Apps, J. Beringer, J. Clein, H. Epstein, D. W. Kicklighter, et al. 2002. "Environmental Variation, Vegetation Distribution, Carbon Dynamics and Water/energy Exchange at High Latitudes." Journal of Vegetation Science: Official Organ of the International Association for Vegetation Science 13 (3): 301–14.

Mikola, Juha, Tarmo Virtanen, Maiju Linkosalmi, Emmi Vähä, Johanna Nyman, Olga Postanogova, Aleksi Räsänen, et al. 2018. "Spatial Variation and Linkages of Soil and Vegetation in the Siberian Arctic Tundra - Coupling Field Observations with Remote Sensing Data." Biogeosciences 15 (9): 2781–2801.

Miller, C. E., P. C. Griffith, S. J. Goetz, D. J. Hodkinson, E. K. Larson, E. S. Kasischke, H. A. Margolis, and E. E. Hoy. 2018. "The Arctic Boreal Vulnerability Experiment (ABoVE) Airborne Campaign." In , 2018:B11A – 03.

Murwira, Amon, and Andrew K. Skidmore. 2005. "The Response of Elephants to the Spatial Heterogeneity of Vegetation in a Southern African Agricultural Landscape." Landscape Ecology 20 (2): 217–34.

Muster, S., M. Langer, B. Heim, S. Westermann, and J. Boike. 2012. “Subpixel Heterogeneity of Ice-Wedge Polygonal Tundra: A Multi-Scale Analysis of Land Cover and Evapotranspiration in the Lena River Delta, Siberia.” Tellus. Series B, Chemical and Physical Meteorology 64 (1): 17301.

Myers-Smith, Isla H., Haydn J. D. Thomas, and Anne D. Bjorkman. 2019. “Plant Traits Inform Predictions of Tundra Responses to Global Change.” The New Phytologist 221 (4): 1742–48.

Naito, Adam T., and David M. Cairns. 2015. “Patterns of Shrub Expansion in Alaskan Arctic River Corridors Suggest Phase Transition.” Ecology and Evolution 5 (1): 87–101.

Nauta, Ake L., Monique M. P. D. Heijmans, Daan Blok, Juul Limpens, Bo Elberling, Angela Gallagher, Bingxi Li, et al. 2014. “Permafrost Collapse after Shrub Removal Shifts Tundra Ecosystem to a Methane Source.” Nature Climate Change 5 (1): 67–70.

Nelson, F. E. and Hinkel K. M. 2003. “Methods for measuring active-layer thickness.” A handbook on Periglacial Field Methods. 10 -20.

Nelson, Peter R., Andrew J. Maguire, Zoe Pierrat, Erica L. Orcutt, Dedi Yang, Shawn Serbin, Gerald V. Frost, et al. 2022. “Remote Sensing of Tundra Ecosystems Using High Spectral Resolution Reflectance: Opportunities and Challenges.” Journal of Geophysical Research. Biogeosciences 127 (2). https://doi.org/10.1029/2021jg006697.

Nitzbon, Jan, Sebastian Westermann, Moritz Langer, Léo C. P. Martin, Jens Strauss, Sebastian Laboor, and Julia Boike. 2020. “Fast Response of Cold Ice-Rich Permafrost in Northeast Siberia to a Warming Climate.” Nature Communications 11 (1): 2201.

Nitze, I., G. Grosse, B. M. Jones, V. E. Romanovsky, and J. Boike. 2018. “Remote Sensing Quantifies Widespread Abundance of Permafrost Region Disturbances across the Arctic and Subarctic.” Nature Communications 9 (1): 5423.

Nitze, Ingmar, Guido Grosse, Benjamin M. Jones, Christopher D. Arp, Mathias Ulrich, Alexander Fedorov, and Alexandra Veremeeva. 2017. “Landsat-Based Trend Analysis of Lake Dynamics across Northern Permafrost Regions.” Remote Sensing 9 (7): 640.

Nitze, Ingmar, Konrad Heidler, Sophia Barth, and Guido Grosse. 2021. “Developing and Testing a Deep Learning Approach for Mapping Retrogressive Thaw Slumps.” Remote Sensing 13 (21): 4294.

O’Donnell, Jonathan A., M. Torre Jorgenson, Jennifer W. Harden, A. David McGuire, Mikhail Z. Kanevskiy, and Kimberly P. Wickland. 2012. “The Effects of Permafrost Thaw on Soil Hydrologic, Thermal, and Carbon Dynamics in an Alaskan Peatland.” Ecosystems 15 (2): 213–29.

Olefeldt, D., S. Goswami, G. Grosse, D. Hayes, G. Hugelius, P. Kuhry, A. D. Mcguire, et al. 2016. “Circumpolar Distribution and Carbon Storage of Thermokarst Landscapes.” Nature Communications. https://doi.org/10.1038/ncomms13043.

Olthof, Ian, and Robert Fraser. 2014. “Detecting Landscape Changes in High Latitude Environments Using Landsat Trend Analysis: 2. Classification.” Remote Sensing. https://doi.org/10.3390/rs61111558.

Ordway, Elsa M., Gregory P. Asner, David F. R. P. Burslem, Simon L. Lewis, Reuben Nilus, Roberta E. Martin, Michael J. O'Brien, et al. 2022. "Mapping Tropical Forest Functional Variation at Satellite Remote Sensing Resolutions Depends on Key Traits." Communications Earth & Environment 3 (1): 1–11.

Osnas, Jeanne L. D., Masatoshi Katabuchi, Kaoru Kitajima, S. Joseph Wright, Peter B. Reich, Sunshine A. Van Bael, Nathan J. B. Kraft, Mirna J. Samaniego, Stephen W. Pacala, and Jeremy W. Lichstein. 2018. "Divergent Drivers of Leaf Trait Variation within Species, among Species, and among Functional Groups." Proceedings of the National Academy of Sciences of the United States of America 115 (21): 5480–85.

Osterkamp, T. E., M. T. Jorgenson, E. A. G. Schuur, Y. L. Shur, M. Z. Kanevskiy, J. G. Vogel, and V. E. Tumskoy. 2009. "Physical and Ecological Changes Associated with Warming Permafrost and Thermokarst in Interior Alaska." Permafrost and Periglacial Processes. https://doi.org/10.1002/ppp.656.

Pan, Y., R. A. Birdsey, J. Fang, R. Houghton, P. E. Kauppi, W. A. Kurz, O. L. Phillips, et al. 2011. "A Large and Persistent Carbon Sink in the World's Forests." Science 333 (6045): 988–93.

Pasquarella, Valerie J., Paulo Arévalo, Kelsee H. Bratley, Eric L. Bullock, Noel Gorelick, Zhiqiang Yang, and Robert E. Kennedy. 2022. "Demystifying LandTrendr and CCDC Temporal Segmentation." International Journal of Applied Earth Observation and Geoinformation 110 (June): 102806.

Peel, M. C., B. L. Finlayson, and T. A. McMahon. 2007. "Updated World Map of the Köppen-Geiger Climate Classification." Hydrology and Earth System Sciences Discussions 4 (2): 439–73.

Pekel, Jean-François, Andrew Cottam, Noel Gorelick, and Alan S. Belward. 2016. "High-Resolution Mapping of Global Surface Water and Its Long-Term Changes." Nature 540 (7633): 418–22.

Peng, Shushi, Xin Lin, Rona L. Thompson, Yi Xi, Gang Liu, Didier Hauglustaine, Xin Lan, et al. 2022. "Wetland Emission and Atmospheric Sink Changes Explain Methane Growth in 2020." Nature 612 (7940): 477–82.

Perreault, Naïm, Esther Lévesque, Daniel Fortier, and Laurent J. Lamarque. 2016. "Thermo-Erosion Gullies Boost the Transition from Wet to Mesic Tundra Vegetation." Biogeosciences 13 (4): 1237–53.

Porter, Claire, Ian Howat, Myoung-Jon Noh, Erik Husby, Samuel Khuvis, Evan Danish, Karen Tomko, et al. 2022. "ArcticDEM - Strips, Version 4.1." Harvard Dataverse. https://doi.org/10.7910/DVN/C98DVS., 2023. "ArcticDEM - Mosaics, Version 4.1." Harvard Dataverse. https://doi.org/10.7910/DVN/3VDC4W.

Rantanen, Mika, Alexey Yu Karpechko, Antti Lipponen, Kalle Nordling, Otto Hyvärinen, Kimmo Ruosteenoja, Timo Vihma, and Ari Laaksonen. 2022. "The Arctic Has Warmed Nearly Four Times Faster than the Globe since 1979." Communications Earth & Environment 3 (1): 1–10.

Raynolds, Martha K., Donald A. Walker, Andrew Balser, Christian Bay, Mitch Campbell, Mikhail M. Cherosov, Fred J. A. Daniëls, et al. 2019. "A Raster Version of the Circumpolar Arctic Vegetation Map (CAVM)." Remote Sensing of Environment 232 (June). https://doi.org/10.1016/j.rse.2019.111297.

Reich, P. B., I. J. Wright, and J. Cavender-Bares. 2003. "The Evolution of Plant Functional Variation: Traits, Spectra, and Strategies." Journal of Plant …. https://www.journals.uchicago.edu/doi/abs/10.1086/374368.

Ricotta, Carlo, Fabien Laroche, László Szeidl, and Sandrine Pavoine. 2020. “From Alpha to Beta Functional and Phylogenetic Redundancy.” Methods in Ecology and Evolution / British Ecological Society 11 (4): 487–93.

Rietkerk, Max, Pieter Ketner, Joep Burger, Bart Hoorens, and Han Olff. 2000. “Multiscale Soil and Vegetation Patchiness along a Gradient of Herbivore Impact in a Semi-Arid Grazing System in West Africa.” Plant Ecology 148 (2): 207–24.

Riihimäki, Henri, Miska Luoto, and Janne Heiskanen. 2019. “Estimating Fractional Cover of Tundra Vegetation at Multiple Scales Using Unmanned Aerial Systems and Optical Satellite Data.” Remote Sensing of Environment. https://doi.org/10.1016/j.rse.2019.01.030.

Rocha, Adrian V., Michael M. Loranty, Phil E. Higuera, Michelle C. Mack, Feng Sheng Hu, Benjamin M. Jones, Amy L. Breen, Edward B. Rastetter, Scott J. Goetz, and Gus R. Shaver. 2012. “The Footprint of Alaskan Tundra Fires during the Past Half-Century: Implications for Surface Properties and Radiative Forcing.” Environmental Research Letters. https://doi.org/10.1088/1748-9326/7/4/044039.

Romanovsky, V. E., and T. E. Osterkamp. 1995. “Interannual Variations of the Thermal Regime of the Active Layer and near-Surface Permafrost in Northern Alaska.” Permafrost and Periglacial Processes 6 (4): 313–35.
Romme, William H., and Dennis H. Knight. 1981. “Fire Frequency and Subalpine Forest Succession along a Topographic Gradient in Wyoming.” Ecology 62 (2): 319–26.

Rösch, Angi, and H. Schmidbauer. 2018. “WaveletComp 1.1: A Guided Tour through the R Package.” . Hsstat. com/projects/WaveletComp …. https://www.researchgate.net/profile/Harald-Schmidbauer/publication/323836523_WaveletComp_11_A_guided_tour_through_the_R_package/links/5abbc0f0aca27222c7536677/WaveletComp-11-A-guided-tour-through-the-R-package.pdf.

Rossi, Christian, Mathias Kneubühler, Martin Schütz, Michael E. Schaepman, Rudolf M. Haller, and Anita C. Risch. 2020. “From Local to Regional: Functional Diversity in Differently Managed Alpine Grasslands.” Remote Sensing of Environment 236 (January): 111415.

Roulet, N., W. Reeburgh, M. Alperin, R. Desjardin, V. Galchenko, W. Glooschenko, R. Lassiter, et al. 1992. “High-Latitude Ecosystems: Sources and Sinks of Trace Gases.” Ecological Bulletins, no. 42: 86–97.

Runge, Alexandra, Ingmar Nitze, and Guido Grosse. 2022. “Remote Sensing Annual Dynamics of Rapid Permafrost Thaw Disturbances with LandTrendr.” Remote Sensing of Environment 268 (January): 112752.

Salmon, Verity G., Patrick Soucy, Marguerite Mauritz, Gerardo Celis, Susan M. Natali, Michelle C. Mack, and Edward A. G. Schuur. 2016. “Nitrogen Availability Increases in a Tundra Ecosystem during Five Years of Experimental Permafrost Thaw.” Global Change Biology 22 (5): 1927–41.

Schädel, Christina, Brendan M. Rogers, David M. Lawrence, Charles D. Koven, Victor Brovkin, Eleanor J. Burke, Hélène Genet, et al. 2024. “Earth System Models Must Include Permafrost Carbon Processes.” Nature Climate Change 14 (2): 114–16.

Schädel, Christina, Edward A. G. Schuur, Rosvel Bracho, Bo Elberling, Christian Knoblauch, Hanna Lee, Yiqi Luo, Gaius R. Shaver, and Merritt R. Turetsky. 2014. “Circumpolar Assessment of Permafrost C Quality and Its Vulnerability over Time Using Long-Term Incubation Data.” Global Change Biology 20 (2): 641–52.

Schaefer, Kevin, Hugues Lantuit, Vladimir E. Romanovsky, Edward A. G. Schuur, and Ronald Witt. 2014. "The Impact of the Permafrost Carbon Feedback on Global Climate." Environmental Research Letters: ERL [Web Site] 9 (8). https://doi.org/10.1088/1748-9326/9/8/085003.

Scheffer, Marten, Jordi Bascompte, William A. Brock, Victor Brovkin, Stephen R. Carpenter, Vasilis Dakos, Hermann Held, Egbert H. van Nes, Max Rietkerk, and George Sugihara. 2009. "Early-Warning Signals for Critical Transitions." Nature 461 (7260): 53–59.

Scheffer, M., S. Carpenter, J. A. Foley, C. Folke, and B. Walker. 2001. "Catastrophic Shifts in Ecosystems." Nature 413 (6856): 591–96.

Schneider, Fabian D., Felix Morsdorf, Bernhard Schmid, Owen L. Petchey, Andreas Hueni, David S. Schimel, and Michael E. Schaepman. 2017. "Mapping Functional Diversity from Remotely Sensed Morphological and Physiological Forest Traits." Nature Communications 8 (1). https://doi.org/10.1038/s41467-017-01530-3.

Schumm, M., S. M. Edie, K. S. Collins, V. Gómez-Bahamón, K. Supriya, A. E. White, T. D. Price, and D. Jablonski. 2019. "Common Latitudinal Gradients in Functional Richness and Functional Evenness across Marine and Terrestrial Systems." Proceedings. Biological Sciences / The Royal Society 286 (1908): 20190745.

Schuur, E. A. G., A. D. McGuire, C. Schädel, G. Grosse, J. W. Harden, D. J. Hayes, G. Hugelius, et al. 2015. "Climate Change and the Permafrost Carbon Feedback." Nature 520 (7546): 171–79.

Schuur, Edward A. G., and Benjamin Abbott. 2011. "High Risk of Permafrost Thaw." Nature Publishing Group UK. November 30, 2011. https://doi.org/10.1038/480032a.

Schuur, Edward A. G., James Bockheim, Josep G. Canadell, Eugenie Euskirchen, Christopher B. Field, Sergey V. Goryachkin, Stefan Hagemann, et al. 2008. "Vulnerability of Permafrost Carbon to Climate Change: Implications for the Global Carbon Cycle." Bioscience. https://doi.org/10.1641/B580807.

Seddon, Alistair W. R., Marc Macias-Fauria, Peter R. Long, David Benz, and Kathy J. Willis. 2016. "Sensitivity of Global Terrestrial Ecosystems to Climate Variability." Nature 531 (7593): 229–32.

Serbin, Shawn P., Aditya Singh, Brenden E. McNeil, Clayton C. Kingdon, and Philip A. Townsend. 2016. "Spectroscopic Determination of Leaf Morphological and Biochemical Traits for Northern Temperate and Boreal Tree Species." Ecological Applications: A Publication of the Ecological Society of America 24 (7): 1651–69.

Serbin, Shawn, and Dedi Yang. 2021. "Maps of Arctic Vegetation Leaf Nitrogen Concentration, Albedo and Plant Functional Type (PFT) Derived from Imaging Spectroscopy Data, Council Watershed, Seward Peninsula, Alaska, 2019." Next Generation Ecosystems Experiment-Arctic, Oak Ridge National Laboratory …. https://www.osti.gov/biblio/1838174.

Shur, Yuri, Kenneth M. Hinkel, and Frederick E. Nelson. 2005. "The Transient Layer: Implications for Geocryology and Climate-Change Science." Permafrost and Periglacial Processes 16 (1): 5–17.

Standen, Katherine M., and Jennifer L. Baltzer. 2021. "Permafrost Condition Determines Plant Community Composition and Community-Level Foliar Functional Traits in a Boreal Peatland." Ecology and Evolution 11 (15): 10133–46.

Stein, Anke, Katharina Gerstner, and Holger Kreft. 2014. “Environmental Heterogeneity as a Universal Driver of Species Richness across Taxa, Biomes and Spatial Scales.” Ecology Letters 17 (7): 866–80.

Sturm, Matthew, and Jonathan Holmgren. 1994. “Effects of Microtopography on Texture, Temperature and Heat Flow in Arctic and Sub-Arctic Snow.” Annals of Glaciology 19: 63–68.

Swanson, David K. 2021. “Permafrost Thaw-related Slope Failures in Alaska’s Arctic National Parks, c . 1980–2019.” Permafrost and Periglacial Processes 32 (3): 392–406.

Tarnocai, C., J. G. Canadell, E. A. G. Schuur, P. Kuhry, G. Mazhitova, and S. Zimov. 2009. “Soil Organic Carbon Pools in the Northern Circumpolar Permafrost Region.” Global Biogeochemical Cycles 23 (2). https://doi.org/10.1029/2008gb003327.

Thaler, E. A., S. Uhleman, J. C. Rowland, J. Schwenk, C. Wang, B. Dafflon, and K. E. Bennett. 2023. “High-resolution Maps of Near-surface Permafrost for Three Watersheds on the Seward Peninsula, Alaska Derived from Machine Learning.” Earth and Space Science (Hoboken, N.J.) 10 (12). https://doi.org/10.1029/2023ea003015.

Thomas, H. J. D., A. D. Bjorkman, I. H. Myers-Smith, S. C. Elmendorf, J. Kattge, S. Diaz, M. Vellend, et al. 2020. “Global Plant Trait Relationships Extend to the Climatic Extremes of the Tundra Biome.” Nature Communications 11 (1): 1351.

Thommeret, N., J. S. Bailly, and C. Puech. 2010. “Extraction of Thalweg Networks from DTMs: Application to Badlands.” Hydrology and Earth System Sciences 14 (8): 1527–36.

Thompson, James A., Jay C. Bell, and Charles A. Butler. 2001. “Digital Elevation Model Resolution: Effects on Terrain Attribute Calculation and Quantitative Soil-Landscape Modeling.” Geoderma 100 (1): 67–89.

Treat, Claire C., Anna-Maria Virkkala, Eleanor Burke, Lori Bruhwiler, Abhishek Chatterjee, Joshua B. Fisher, Josh Hashemi, et al. 2024. “Permafrost Carbon: Progress on Understanding Stocks and Fluxes across Northern Terrestrial Ecosystems.” Journal of Geophysical Research. Biogeosciences 129 (3). https://doi.org/10.1029/2023jg007638.

Tucker, Compton J. 1979. “Red and Photographic Infrared Linear Combinations for Monitoring Vegetation.” Remote Sensing of Environment 8 (2): 127–50.

Turetsky, M., B. Abbott, M. Jones, K. M. Walter Anthony, D. Olefeldt, E. A. G. Schuur, G. Grosse, et al. 2020. “Carbon Release through Abrupt Permafrost Thaw.” Nature Geoscience Accepted (February). https://doi.org/10.1038/s41561-019-0526-0.

Turetsky, Merritt R., Benjamin W. Abbott, Miriam C. Jones, Katey Walter Anthony, David Olefeldt, Edward A. G. Schuur, Charles Koven, et al. 2019. “Permafrost Collapse Is Accelerating Carbon Release.” Nature 569 (7754): 32–34.

Van Everdingen, Robert O., International Permafrost Association, and Others. 1998. Multi-Language Glossary of Permafrost and Related Ground-Ice Terms in Chinese, English, French, German. Arctic Inst. of North America University of Calgary.

Villéger, Sébastien, Norman W. H. Mason, and David Mouillot. 2008. “New Multidimensional Functional Diversity Indices for a Multifaceted Framework in Functional Ecology.” Ecology 89 (8): 2290–2301.

Violle, Cyrille, Marie-Laure Navas, Denis Vile, Elena Kazakou, Claire Fortunel, Irène Hummel, and Eric Garnier. 2007. “Let the Concept of Trait Be Functional!” Oikos 116 (5): 882–92.

Violle, Cyrille, Peter B. Reich, Stephen W. Pacala, Brian J. Enquist, and Jens Kattge. 2014. “The Emergence and Promise of Functional Biogeography.” Proceedings of the National Academy of Sciences of the United States of America 111 (38): 13690–96.

Vries, Franciska T. de, Pete Manning, Jerry R. B. Tallowin, Simon R. Mortimer, Emma S. Pilgrim, Kathryn A. Harrison, Phil J. Hobbs, et al. 2012. “Abiotic Drivers and Plant Traits Explain Landscape-Scale Patterns in Soil Microbial Communities.” Ecology Letters 15 (11): 1230–39.

Wainwright, Haruko M., Baptiste Dafflon, Lydia J. Smith, Melanie S. Hahn, John B. Curtis, Yuxin Wu, Craig Ulrich, John E. Peterson, Margaret S. Torn, and Susan S. Hubbard. 2015. “Identifying Multiscale Zonation and Assessing the Relative Importance of Polygon Geomorphology on Carbon Fluxes in an Arctic Tundra Ecosystem.” Journal of Geophysical Research: Biogeosciences 120 (4): 788–808.

Wainwright, Haruko M., Anna K. Liljedahl, Baptiste Dafflon, Craig Ulrich, John E. Peterson, Alessio Gusmeroli, and Susan S. Hubbard. 2017. “Mapping Snow Depth within a Tundra Ecosystem Using Multiscale Observations and Bayesian Methods.” Cryosphere 11 (2): 857–75.

Walker, Xanthe J., Jennifer L. Baltzer, Steven G. Cumming, Nicola J. Day, Christopher Ebert, Scott Goetz, Jill F. Johnstone, et al. 2019. “Increasing Wildfires Threaten Historic Carbon Sink of Boreal Forest Soils.” Nature 572 (7770): 520–23.

Wang, Peng, Juul Limpens, Liesje Mommer, Jasper Ruijven, Ake L. Nauta, Frank Berendse, Gabriela Schaepman-Strub, Daan Blok, Trofim C. Maximov, and Monique M. P. D. Heijmans. 2017. “Above- and Below-ground Responses of Four Tundra Plant Functional Types to Deep Soil Heating and Surface Soil Fertilization.” The Journal of Ecology 105 (4): 947–57.

Wieczynski, Daniel J., Sandra Díaz, Sandra M. Durán, Nikolaos M. Fyllas, Norma Salinas, Roberta E. Martin, Alexander Shenkin, et al. 2022. “Improving Landscape-scale Productivity Estimates by Integrating Trait-based Models and Remotely-sensed Foliar-trait and Canopy-structural Data.” Ecography 2022 (8). https://doi.org/10.1111/ecog.06078.

Winzeler, Hans Edwin, Phillip R. Owens, Quentin D. Read, Zamir Libohova, Amanda Ashworth, and Tom Sauer. 2022. “Topographic Wetness Index as a Proxy for Soil Moisture in a Hillslope Catena: Flow Algorithms and Map Generalization.” Land 11 (11): 2018.

Wright, Ian J., Peter B. Reich, Mark Westoby, David D. Ackerly, Zdravko Baruch, Frans Bongers, Jeannine Cavender-Bares, et al. 2004. “The Worldwide Leaf Economics Spectrum.” Nature 428 (6985): 821–27.

Yang, Dedi, Wouter Hantson, Daniel Hayes, and Shawn Serbin. n.d. “UAS Remote Sensing (DJI Phantom 4 RTK Platform): RGB Orthomosaic, Digital Surface and Canopy Height Models, Plant Functional Type Map,

Seward Peninsula, Alaska, 2019." Next Generation Ecosystem Experiments - Arctic. Accessed April 25, 2023. https://data.ngee-arctic.ornl.gov/data/pages/NGA300.html.

Yang, Dedi, Ran Meng, Bailey D. Morrison, Andrew McMahon, Wouter Hantson, Daniel J. Hayes, Amy L. Breen, Verity G. Salmon, and Shawn P. Serbin. 2020. "A Multi-Sensor Unoccupied Aerial System Improves Characterization of Vegetation Composition and Canopy Properties in the Arctic Tundra." Remote Sensing 12 (16): 2638.

Yang, Dedi, Bailey D. Morrison, Kenneth J. Davidson, Julien Lamour, Qianyu Li, Peter R. Nelson, Wouter Hantson, et al. 2022. "Remote Sensing from Unoccupied Aerial Systems: Opportunities to Enhance Arctic Plant Ecology in a Changing Climate." The Journal of Ecology 110 (12): 2812–35.

Yang, Dedi, Bailey D. Morrison, Wouter Hanston, Andrew McMahon, Latha Baskaran, Daniel J. Hayes, Charles E. Miller, and Shawn P. Serbin. 2023. "Integrating Very-High-Resolution UAS Data and Airborne Imaging Spectroscopy to Map the Fractional Composition of Arctic Plant Functional Types in Western Alaska." Remote Sensing of Environment 286 (March): 113430.

Yang, Dedi, Bailey D. Morrison, Wouter Hantson, Amy L. Breen, Andrew McMahon, Qianyu Li, Verity G. Salmon, Daniel J. Hayes, and Shawn P. Serbin. 2021. "Landscape-Scale Characterization of Arctic Tundra Vegetation Composition, Structure, and Function with a Multi-Sensor Unoccupied Aerial System." Environmental Research Letters. https://doi.org/10.1088/1748-9326/ac1291.

Zandt, Michiel H. in 't, Susanne Liebner, and Cornelia U. Welte. 2020. "Roles of Thermokarst Lakes in a Warming World." Trends in Microbiology. https://doi.org/10.1016/j.tim.2020.04.002.

Zhang, Caiyun, Thomas A. Douglas, and John E. Anderson. 2021. "Modeling and Mapping Permafrost Active Layer Thickness Using Field Measurements and Remote Sensing Techniques." International Journal of Applied Earth Observation and Geoinformation 102 (October): 102455.

Zhang, Weixing, Anna K. Liljedahl, Mikhail Kanevskiy, Howard E. Epstein, Benjamin M. Jones, M. Torre Jorgenson, and Kelcy Kent. 2020. "Transferability of the Deep Learning Mask R-CNN Model for Automated Mapping of Ice-Wedge Polygons in High-Resolution Satellite and UAV Images." Remote Sensing 12 (7): 1085.

Zhu, Zhe, and Curtis E. Woodcock. 2014. "Continuous Change Detection and Classification of Land Cover Using All Available Landsat Data." Remote Sensing of Environment 144 (March): 152–71. style of the bibliography will vary by discipline.

BIOGRAPHY OF THE AUTHOR

Wouter Hantson was born in Brugge, Belgium on February 5, 1980. He was raised in Rumbeke, Belgium and graduated from SIVI High School in 1999. Wouter attended the Erasmus Hogeschool Brussel, Belgium and graduated in 2005 with a Bachelor's degree in Chemistry. He moved to Wageningen, the Netherlands and entered the Geo-Information Science Master program at Wageningen University, graduating in summer 2010. After receiving his degree, he joined Avia-GIS, a Belgian startup specialized in spatial epidemiology. After spending some years in Ecuador, he moved to Maine to begin his PhD program at The University of Maine in the fall of 2017. After receiving his degree, Wouter will be joining WSL, the Swiss Federal Institute for Forest, Snow, and Landscape Research as a postdoctoral researcher. Wouter is a candidate for the Doctor of Philosophy in Forest Resources from the University of Maine in August 2024.